MS RESEARCH THESIS

Modeling, Fabrication, and Optimization of the Electrical Contacts of Undoped, n- and p-type Doped AlN Films

Submitted By

Student Name: Sana Nasir

Registration No: 168-FET/MSEE/F21

Supervisor: Dr. Habib Ahmad

DEPARTMENT OF ELECTRICAL AND COMPUTER ENGINEERING

FACULTY OF ENGINEERING AND TECHNOLOGY

INTERNATIONAL ISLAMIC UNIVERSITY, ISLAMABAD

October, 2024

CERTIFICATE OF APPROVAL

Title of Thesis: Modeling, Fabrication, and Optimization of the Electrical Contacts of Undoped, n- and p-type Doped AlN Films.

Name's Student: Sana Nasir

Registration No: 168-FET/MSEE/F21

Approved by the Department of Electrical and Computer Engineering, Faculty of Engineering and Technology, International Islamic University Islamabad, in partial fulfillment of the requirement for the degree of MS. Electrical Engineering.

Viva Voice Committee

Supervisor
Dr. Habib Ahmad _____
Assistant Professor, DECE / FET/ IIUI

Internal Examiner

_____

External Examiner

_____

Chairman
DECE / FET / IIUI
Dr. Shahid Ikram _____

Dean
FET / IIUI
Prof. Dr. Saeed Badshah _____

بِسْمِ اللهِ الرَّحْمٰنِ الرَّحِيْمِ

DECLARATION

I solemnly declare that the thesis entitled "Modeling, Fabrication, and Optimization of the Electrical Contacts of Undoped, n- and p-type Doped AlN Films" represents my work conducted at International Islamic University, Islamabad, under the supervision of Dr. Habib Ahmad. The research presented herein is original, and I have duly acknowledged all sources through proper citation. This thesis has not been previously submitted for any other degree or qualification at this institution or elsewhere. I affirm the accuracy of all data, figures, and results presented, which have been obtained through ethical research practices. Any assistance received in the preparation of this thesis has been appropriately acknowledged.

Sana Nasir

168-FET/MSEE/F21

ACKNOWLEDGMENTS

As I present this Master of Science thesis in Electrical Engineering, my foremost gratitude is to Allah, for granting me all that was needed to undertake and complete this academic endeavor. In every challenge faced and triumph achieved, it is to Him that I turn in gratitude.

I am sincerely thankful to my supervisor, Dr. Habib Ahmad, for his exceptional guidance and continuous support throughout my research journey. His expertise, patience, and insightful feedback have been pivotal in the development of this thesis and in helping me grow as a researcher. I am truly appreciative of the opportunity to learn from him and enhance my research skills under his supervision.

I would also like to acknowledge the Center for Advanced Electronics & Photovoltaic Engineering (CAEPE) for giving me access to the necessary facilities and resources to perform my research. I extend special thanks to Research Associate Engr. Muhammad Ali for his guidance and support during the research process. The technical support staff at CAEPE have been incredibly helpful and instrumental in the successful completion of this project.

My heartfelt gratitude goes to my family for their unwavering support, understanding, and encouragement throughout my studies. Their love and faith in me have always been a source of strength and motivation.

ABSTRACT

Recent advancements in the development of doped aluminum nitride (AlN) films have opened new avenues in semiconductor technology. However, establishing effective electrical contacts to AlN, with its ultra-wide bandgap of 6.1 eV, remains a significant challenge that hinders fully realizing its potential in high-performance electronic and optoelectronic applications. This study addresses the challenges associated with fabricating high-quality AlN thin films and establishing low-resistance ohmic contacts through a combination of TCAD simulations and experimental techniques.

The research utilizes Silvaco TCAD simulations to investigate the behavior of various metal contacts on AlN films. The study identifies platinum (Pt) as the optimal contact metal for p-type and undoped AlN, achieving the lowest Schottky barrier height (Φ_B) of 2.9 eV. For n-type AlN, indium (In) contacts resulted in the lowest Φ_B of 1.6 eV. Additionally, the research explores the performance of fully GaN-based and AlN-on-GaN Junction Barrier Schottky (JBS) diodes, optimizing inter-p^+ spacings to enhance diode performance. For an i-layer thickness of 0.5 μm, the ideal trade-off between specific on-resistance ($R_{on,sp}$) and breakdown voltage (V_{br}) is achieved at 1.2 μm spacing for GaN-based diodes, yielding a $R_{on,sp}$ of 6.13×10^{-3} mΩ·cm^2, a V_{br} of 185.72 V, a critical electric field of 3.75 MV/cm, and a BFOM of 347 MW/cm^2. Similarly, AlN/GaN diodes at 1.4 μm spacing achieve optimal performance with a $R_{on,sp}$ of 5.14×10^{-3} mΩ·cm^2, a V_{br} of 156.98 V, a critical electric field of 4.32 MV/cm, and a BFOM of 678 MW/cm^2. This research demonstrates the superior performance of JBS diodes compared to PiN diodes under forward bias and Schottky diodes under reverse bias conditions. The AlN/GaN diodes exhibit an unprecedented BFOM, setting a new benchmark in the field.

The experimental work involves a systematic approach to fabricating AlN thin films using magnetron sputtering and metal-modulated epitaxy (MME), followed by the deposition of metal contact stacks on AlN films through physical vapor deposition (PVD) and e-beam evaporation. The study demonstrates high-crystalline-quality AlN films and low-resistance ohmic contacts using Pt/Pd/Au stacks for n-type and p-type AlN films, and cost-effective contact stacks of Ag, Al, Cu, Sn, and Zn metals for undoped AlN films. Various

characterization methods, including current-voltage (I-V) characteristics, Hall effect measurements, thickness profilometry, scanning electron microscopy, and spectroscopic ellipsometry, were employed to evaluate the electrical optical, and structural properties of the fabricated samples. The annealed undoped AlN samples exhibited higher currents likely due to defects such as cracks or impurities in the films. However, a magnetron sputtering power of 200 W, a substrate temperature of 300 °C, and an N_2 flow rate of 25 sccm, resulted in a high-quality, defect-free AlN film with current levels in the nanoampere range for undoped AlN sample 8 that exhibited an effective Richardson constant of 7.19×10^{-7} A/cm²K² and a Schottky barrier height of 0.59 eV. Hall effect measurements confirmed significant bulk conductivity in AlN:Si sample with 9.7×10^{17} electron concentration, a resistivity of 102 mΩ.cm, and a Hall mobility of 62.45 cm²/(V·s). The AlN:Be sample demonstrated bulk conductivity with 2.92×10^{17} cm^{-3} hole concentration, a resistivity of 1.642 Ω·cm, and a Hall mobility of 13 $cm^2/(V\cdot s)$. These findings underscore the potential of AlN films in advancing semiconductor technology, particularly in high-performance electronic and optoelectronic applications. The successful integration of low-resistance ohmic contacts and the optimization of JBS diodes highlight the practical viability of AlN-based devices. Future work will focus on further refining the fabrication processes and exploring the scalability of these techniques for industrial applications. This research paves the way for the development of next-generation semiconductor devices with superior performance and reliability.

TABLE OF CONTENTS

LIST OF FIGURES

LIST OF TABLES

LIST OF ABBREVIATIONS

Abbreviation	Full Term
Al	Aluminum
AlN	Aluminum Nitride
Ag	Silver
Au	Gold
BFOM	Baliga's Figure of Merit
BSE	Backscattered Electrons
CDA	Compressed Dry Air
CTLM	Circular Transmission Line Measurement
Cu	Copper
DCMS	Direct Current Magnetron Sputtering
EDS	Energy Dispersive Spectrometer
FOM	Figure of Merit
FWHM	Full Width at Half Maximum
GaN	Gallium Nitride
HEM	Hall Effect Measurements
HRXRD	High-Resolution X-ray Diffraction
HVPE	Hydride Vapor Phase Epitaxy
I-V	Current-Voltage
I-V-T	Temperature Dependent Current-Voltage
In	Indium
JBS	Junction Barrier Schottky
LVDT	Linear Variable Differential Transformer
MBE	Molecular Beam Epitaxy
MME	Metal-Modulated Epitaxy
MS	Magnetron Sputtering
NIR	Near-Infrared
PAMBE	Plasma-Assisted Molecular Beam Epitaxy
Pd	Palladium
Pt	Platinum
PVD	Physical Vapor Deposition
RCA	Radio Corporation of America
RMS	Root Mean Square

RTA	Rapid Thermal Annealing
SBH	Schottky Barrier Height
SE	Secondary Electrons
SEM	Scanning Electron Microscopy
SiC	Silicon Carbide
Sn	Tin
SNR	Signal-to-Noise Ratio
SBD	Schottky Barrier Diode
TCAD	Technology Computer Aided Design
UID	Unintentionally Doped
UV	Ultraviolet
VBM	Valence Band Maximum
WBG	Wide-Band Gap
XPS	X-ray Photoelectron Spectroscopy
Zn	Zinc
ZnO	Zinc Oxide

LIST OF NOMENCLATURE

Symbol	Description
A^*	Effective Richardson constant
A_{sch}	Schottky contact area
d	Thickness of the AlN layer
E_{00}	Characteristic energy
E_F	Fermi energy level
E_G	Energy band gap
E_{vacuum}	Vacuum energy level
I_{sat}	Saturation current
J_F	Forward current density
$J_{T.E}$	Thermionic emission current density
J_{sch}	Schottky barrier lowering current density
J_{tunnel}	Tunneling current density
k	Boltzmann constant
m_{tunn}	Tunneling effective mass
N_A	Acceptor concentration
N_D	Donor concentration
n	Ideality factor
n_i	Intrinsic carrier concentration
Pa	Average roughness
Pq	RMS roughness
Psk	Skewness
Pku	Kurtosis
Pz	Average maximum height
Pp	Maximum peak height
Pv	Maximum valley depth
Pt	Maximum height between the highest peak and the lowest valley
q	Elementary charge
$R_{on,sp}$	Specific on-resistance
R_s	Sheet resistance
R_t	Total resistance
S	Contact area
T	Kelvin Temperature

V_{bi}	Built-in voltage
V_{br}	Breakdown voltage
V_F	Forward voltage drop
V_H	Hall voltage
W	Depletion width
χ	Electron affinity
Φ_B	Schottky barrier height
Φ_M	Metal work function

CHAPTER 1

INTRODUCTION

1.1 Background

1.1.1 Wide-Band Gap Semiconductors

Wide-band gap semiconductors (WBG) are materials with larger energy band gaps than traditional semiconductors, such as silicon. Recent advances in the growth and fabrication of WBG semiconductors, particularly group III- V compounds, have seen enormous advancements concerning material quality and device performance. These materials have broad and flexible direct energy band gaps ranging from 0.7–1.9 eV for InN through 3.4 to 6.2 eV for GaN and AlN respectively [1]. WBG semiconductors offer numerous benefits when compared to conventional semiconductors, including:

- Higher breakdown voltage
- Higher operating temperatures
- Higher frequency operation
- Higher electron mobility
- Lower power losses and increased efficiency

WBG semiconductors are increasingly utilized in high-power, high-temperature, high-frequency electronics, and deep ultraviolet (UV) optoelectronics. Among these semiconductor materials, Gallium Nitride (GaN) has emerged as a prominent material attributed to its exceptional electrical and optical properties. The inherent properties of GaN, such as its wide bandgap, high breakdown electric field, high electron mobility, and superior thermal conductivity make it suitable for various applications ranging from power electronics to solid-state lighting [2], [3], [4]. Therefore, the continued development of WBG semiconductor materials is crucial to meet the increasing demand for advanced electronic and optoelectronic devices.

1.1.2 Aluminum Nitride: Properties and Applications

One of the promising III-nitride compounds is aluminum nitride (AlN). Crystalline or c-axis oriented AlN in the hexagonal wurtzite structure is an ultra-wide direct bandgap semiconductor with an E_g of ~6.1 eV at room temperature [5]. It has several advantages over other group III-nitrides including larger band gap, high values of the critical field, thermal conductivity, thermal and chemical stability, saturation velocity, breakdown voltage, refractive index, peak velocities, current density, and significant piezoelectricity [6], [7], [8], [9], [10] .Compared to all relevant semiconductors, AlN ranks first or second in all major Figures of Merit (FOM) [11], indicating its potential for achieving higher performance parameters across diverse applications.

Figure 1.1 shows the wurtzite crystal structure of AlN which is analogous to that of Gallium Nitride (GaN), Zinc Oxide (ZnO), and to that of other group III-nitride compounds. In this hexagonal arrangement, each aluminum atom is tetrahedrally coordinated with four nitrogen atoms, forming a three-dimensional network.

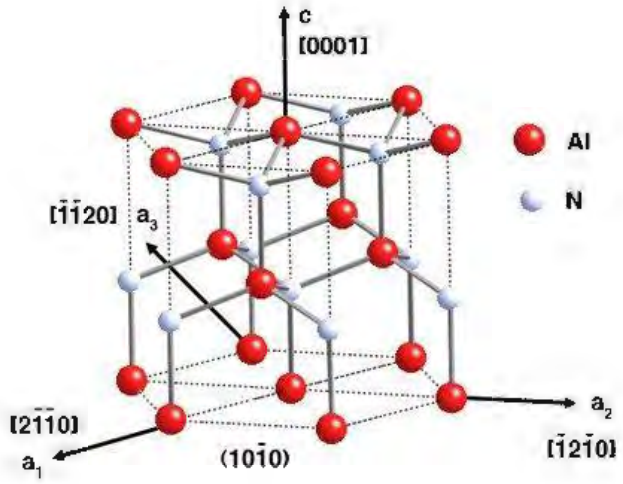

Figure 1.1: Schematic representation of an AlN hexagonal wurtzite standard unit cell [10]

This hexagonal crystal lattice arrangement imparts an ultra-wide bandgap to AlN, contributing to its several important properties. Covalent bonding between aluminum and nitrogen atoms not only bolsters the mechanical strength of AlN but it facilitates efficient heat dissipation contributing to its high thermal conductivity. Additionally, the hexagonal crystal structure of AlN, being non-centrosymmetric, gives it notable piezoelectric properties. The following table lists key material properties of intrinsic AlN at room

temperature and compares them to the traditional semiconductor silicon, the substrate material utilized in this investigation.

Table 1.1: Intrinsic properties of AlN and Si [5], [12], [13], [14], [15], [16]

Property	**Value**	
	Aluminum Nitride	**Silicon**
Crystal structure	Hexagonal wurtzite (Tetrahedral geometry)	Diamond (Face-Centered Cubic)
Lattice constants [Å]	a = b = 3.11, c = 4.98	a = 5.431
Molar mass [g/mol]	40.989	28.09
Density [g/cm^3]	3.255	2.3290
Melting point [°C]	2,500	1414
Bandgap [eV]	6.2 (direct)	1.12 (indirect)
Refractive index	1.8 – 2.2	3.8
Dielectric Constant	~9.0	11.9
Electrical Resistivity [Ω.cm]	>10^{14}	~2.3×10^5
Electron mobility [cm^2/Vs]	300	1400
Hole mobility [cm^2/Vs]	14	450
Thermal conductivity [Wm^{-1}K^{-1}]	319	149
Critical field [MV/cm]	15.4	0.3
Electron affinity [eV]	0.6 - 1.9	4.01
Breakdown Voltage (at 10 mΩ cm^2) [V]	20,000	100

The ultra-wide bandgap in AlN results in a higher critical field as compared to the current technologies of wide bandgap semiconductors such as SiC (3.1 MV/cm), GaN (4.9

MV/cm), and β-Ga_2O_3 (10.3 MV/cm), which makes it particularly effective for use in high-power devices. [17]. AlN is suited for applications requiring high power and temperature because its high thermal conductivity makes it capable of operating under extreme environments, including high-radiation environments.

AlN is a demanding material for optical, UV optoelectronic, high-frequency electroacoustic, and sensors due to its excellent thermal and mechanical compatibility with substrate materials [18], [19].

1.1.3 Electrical Contacts

The formation and characterization of stable, low-resistance contacts with linear I-V characteristics in device fabrication are crucial in ensuring the efficiency and durability of semiconductor devices. By causing the semiconductor material next to the junction to deplete, improperly constructed junctions to semiconductors can readily exhibit rectifying behavior, leaving the device inoperable by obstructing the charge flow between those devices and the external circuitry. Electrical contact conductivity plays a pivotal role in the performance of optoelectronic and electronic devices. Besides negligible contact resistance and other typical contact properties, they must possess good chemical and mechanical properties, including corrosion resistance, toughness, electrical and thermal conductivity, etc.

Based on their composition and metallurgical structure, the following categories can be used to classify materials appropriate for use as electrical contacts:

- Pure metals
- Alloys
- Composite materials

However, making good contacts to AlN continues to be a challenging task in research, mainly attributed to its low electron affinity which is reported to be in the range of 0.6-1.9 eV [20], and wide bandgap resulting in a high potential barrier. It is critical to have a solution for making good electrical contact with the material. All known metals are unreliable for making contacts to AlN, so metal alloys and exceptional contact stacks of the highest work function metals are required such as Pt (5.29 eV), Pd (4.82 eV), Cu (4.47

eV), Au (4.58 eV), Ag (4.28 eV), Sn (4.11 eV), Zn (3.74 eV), and Al (3.74 eV) etc. [21]. However, due to the AlN's wide energy bandgap, one of the main problems in AlN-based devices is the fabrication of ohmic contacts. Due to the high work function requirements of the metal contacts, applying low-resistance ohmic contacts to p-type AlN films is extremely difficult.

This research study comprises the TCAD modeling, fabrication, and experimental investigation to achieve optimized ohmic electrical contact stacks to undoped, p-type, and n-type doped AlN films. The project involves the growth and modeling of the required AlN layers on silicon substrates via magnetron sputtering. Silicon substrates have received a lot of attention for epitaxially growing AlN thin films due to their huge scale and ease of industrial mass manufacturing. Several research initiatives have focused on growing AlN layers on silicon wafers with 100 and 111 crystal orientations to produce high-quality AlN films. AlN films can be grown by a variety of methods, such as chemical vapor deposition (CVD), physical vapor deposition (PVD) techniques like pulsed laser deposition (PLD), molecular beam epitaxy (MBE), thermal evaporation, and reactive sputtering (RF or DC, with or without magnetron). Magnetron sputtering is the most popular technique due to its benefits like fast deposition rates, uniform coating of large substrates, easiness, low temperature, low cost, flexibility, etc. [22]. After the growth of the required AlN thin film, a detailed study would be conducted by exploring extensive contacts stack structures, annealing temperatures, and inert gases flow conditions to achieve the optimized contacts to AlN.

1.2 Problem Statement

Being a UWBG material, the doping of AlN was a big challenge for a long time due to reconfigurable defect formation and dopant compensation making doping inefficient. However, recent advances in the doping of AlN have achieved a maximum electron concentration of ~6×10^{18} cm^{-3} for n-type AlN films, and the highest concentration of holes of ~3×10^{18} cm^{-3} for n-type AlN films [17]. These research advances make AlN suitable for high-temperature/voltage/power devices, deep ultraviolet (UV) optical detectors, and emitters capable of operating in extreme heat and radiation environments.

However, making good contacts to AlN is still a big research problem. AlN has an electron affinity that is reported to be in the range of 0.6-1.9 eV. So, the work function of p-type AlN films would presumably be ~6.8 to 8.1 eV. Even the highest work function metals such as platinum (5.29), palladium (4.82 eV), and gold (4.58 eV) would introduce a large Schottky barrier to such films.

Improper contacts to the AlN films would result in high contact resistance badly impacting device measurements. Thus, a comprehensive study of different contact stacks to undoped, n- and p-type AlN was desired to demonstrate good contacts conductivity of these films. This required the growth and modeling of the requisite AlN films as well.

The central challenge addressed in this work is to identify optimized contact stacks to AlN films. A detailed experimental and modeling study has been performed to achieve these optimized AlN contacts by exploring extensive contact stack structures, annealing temperatures, and inert gases flow conditions.

1.3 Objectives of the Research

This research seeks to achieve the following objectives:

1. Using the Silvaco TCAD tool to design, characterize, and optimize the desired device structure and obtain optimal parameters for performing experimentation.
2. To achieve high-crystalline-quality AlN thin films on silicon by optimizing the growth conditions (plasma power, substrate temperature, and nitrogen flow rate) via Magnetron Sputtering.
3. To fabricate cost-effective low-resistance electrical contact stack structures to undoped, n- and p-type AlN films by optimizing annealing temperatures and inert gases flow conditions.

1.4 Significance of the Research

AlN is a semiconductor with increasing industrial interest because of its numerous possible uses in the production of devices. With an ultra-wide bandgap of around 6.1 eV, it can offer operating frequencies that are many orders of magnitude higher and can sustain significantly greater breakdown voltages than silicon.

AlN possesses an extremely high thermal conductivity, high index of refraction, high thermal and chemical stability, and high breakdown field. These characteristics make thermodynamically stable AlN films potential materials for serving as buffer layers in GaN growth and in other microelectronic and optoelectronic applications [23], [24]. AlN's high thermal conductivity (319 $Wm^{-1}K^{-1}$) allows effective heat dissipation, which makes it appropriate for applications involving high power and elevated temperatures capable of operating under severe conditions, including high-radiation environments.

AlN is recognized as a piezoelectric material with an acoustic velocity greater than 5500 m/s as opposed to less than 4000 m/s for quartz or less than 5000 m/s for lithium niobate. AlN is therefore seen favorably for applications in both optical and electroacoustic fields [25]. AlN, due to its ultra-wide bandgap and thus higher critical field as compared to the current technologies of wide bandgap semiconductors such as SiC (3.1 MV/cm), GaN (4.9MV/cm), and β-Ga2O3 (10.3 MV/cm), is used in power devices that offer increased breakdown voltage and reduced on-resistance.

The emission wavelength of AlN falls in the 200nm range enabling a vast range of applications including, laser beam machining, curing applications, lithography, and deep ultraviolet light-based disinfection systems, high-temperature and high-power electronics [17]. AlN-based UV light sources are gaining prominence in the laser industry as a result of potential uses for curing resin, epoxies, and polymers [26]. AlN-based devices perform better in power electronics than existing GaN devices because of their enhanecd thermal conductivity and breakdown field (15.4 $MVc^{-1}m^{-1}$) [27].

The realization of all these potential applications requires high-crystalline-quality AlN films and making effective low-resistance contacts to them. A major obstacle in the development of high-performance AlN-based systems is the formation of reliable ohmic contacts. Realizing ohmic contacts with minimized resistance is necessary for all semiconductor laser applications, high-power and high-frequency devices. This study focuses on addressing these research problems and providing potential solutions.

1.5 Methodology of the Research

The figure below sequentially displays the methodology employed to conduct the research.

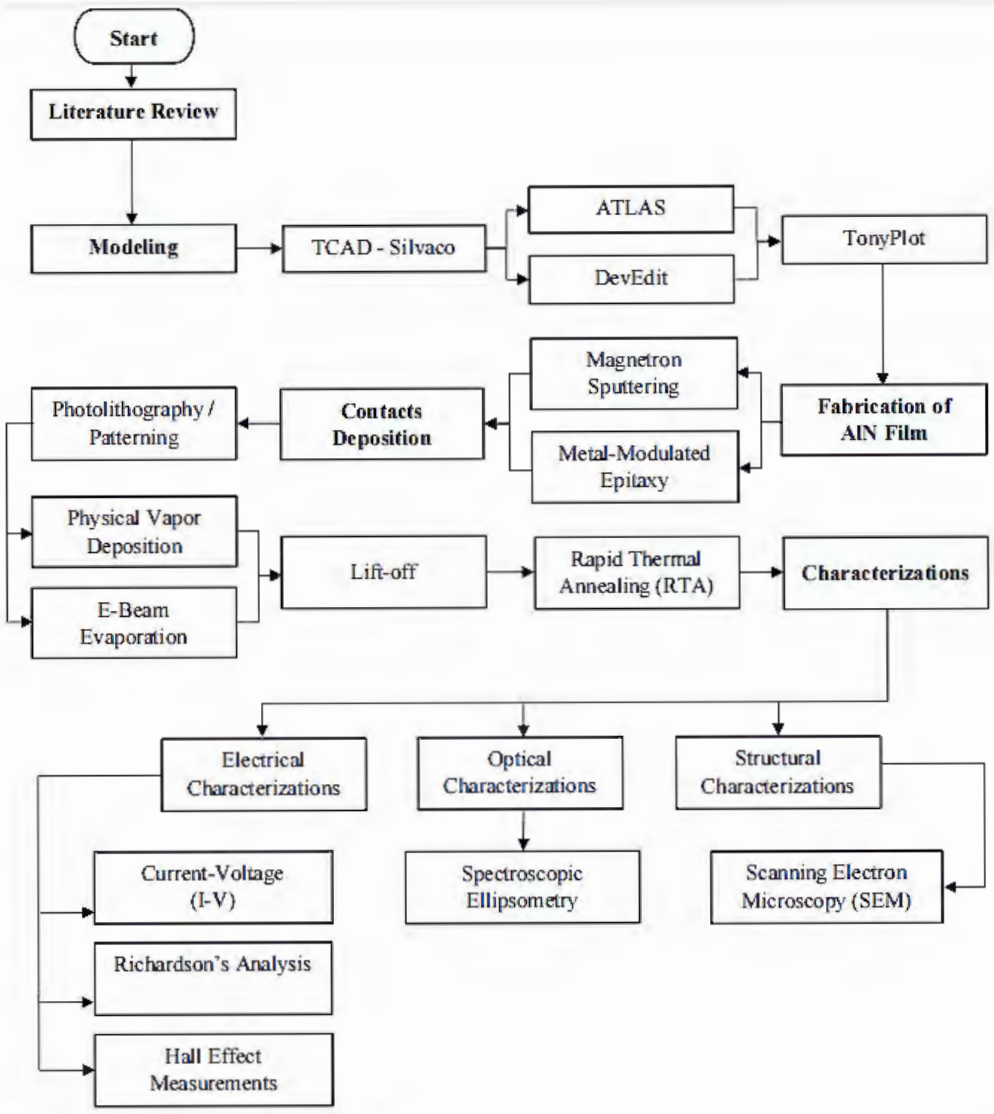

Figure 1.2: Research methodology flow diagram

A description of the methodology of research is given below.

1.5.1 Literature Survey

During this phase of research, an understanding of the concepts and theories related to the research topic has been developed and an in-depth review of the previous research findings has been conducted to examine, compare, and contrast the problems that are already investigated, to study the associated methodologies, to find the research gaps in this domain and to locate this research within the context of existing literature. A comprehensive study has been conducted to find the latest related work; extensive literature about the high-quality AlN growth on the silicon substrate, how various growth conditions affect the

quality of the films, various contacts stack structures, and the impact of annealing temperatures and gases flow conditions on the contact conductivity was studied and summarized to make evaluations, arguments and for conducting the original research on the selected topic.

1.5.2 Modeling and Simulation

Then the individual films and devices have been modeled and simulated using Silvaco TCAD. Using the DevEdit device structure editor and ATLAS TCAD tool, device modeling has been performed, various characteristics have been analyzed and optimization has been done. The results or data generated by the Silvaco TCAD are displayed using the TonyPlot visualization tool. The extracted optimum simulation parameters were used for the fabrication process.

1.5.3 Fabrication, Characterization & Testing

This phase involves experimentation, wherein AlN thin films were produced on silicon substrates through the process of Magnetron Sputtering. Subsequently, electrical contacts were deposited employing lithography/patterning, Physical Vapor Deposition, and etching, followed by annealing the contacts on the samples. Following this, a comprehensive analysis encompassing structural, electrical, and optical characterization and testing of the fabricated device was conducted.

1.6 Thesis Organization

The structure of this thesis is outlined as follows:

- Chapter 1 briefly introduced the research context followed by the problem statement, research objectives, significance, and methodology of the research.
- Chapter 2 delves into the theoretical considerations of metal-semiconductor contacts, including the Schottky-Mott model, ohmic contact formation to AlN, and the foundations of Junction Barrier Schottky (JBS) diodes.
- Chapter 3 offers a comprehensive review of the existing relevant literature.
- Chapter 4 presents the TCAD modeling and simulation of AlN contacts and JBS diodes, along with a detailed analysis of the results.

- Chapter 5 provides an in-depth exploration of the fabrication process, including the tools and techniques employed.
- Chapter 6 discusses the various characterization techniques utilized in this study.
- Chapter 7 presents the characterization results and their subsequent analysis.
- Chapter 8 provides a brief conclusion and outlines potential future research directions.

CHAPTER 2

METAL-SEMICONDUCTOR CONTACTS

2.1 Introduction to Metal-Semiconductor Contacts

In semiconductor device technology, the interaction between metal and semiconductor materials is vital for defining the electrical properties and overall device performance. Two primary types of metal-semiconductor contacts are widely employed in semiconductor devices [28]:

1. Rectifying or Schottky contacts
2. Non-rectifying or Ohmic contacts

A Schottky contact functions as a diode with rectifying properties, while the alternative is a low-resistance ohmic contact exhibiting linear current-voltage (I-V) characteristics. Typically, a Schottky barrier arises when a metal interfaces with an undoped or lightly doped semiconductor. However, when a metal interacts with a highly doped semiconductor and undergoes additional thermal treatment, it can establish low-resistance ohmic contacts.

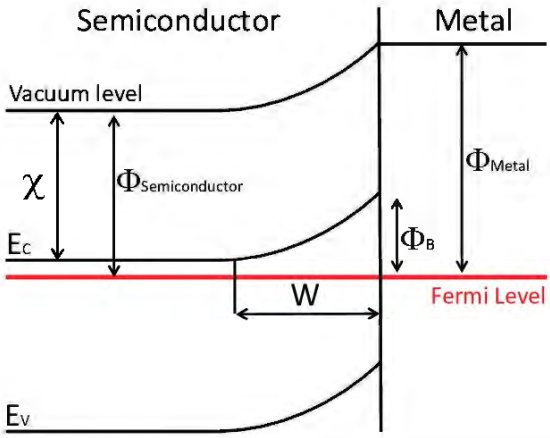

Figure 2.1: Energy band diagram of semiconductor-metal junction in equilibrium [29]

The above figure depicts the energy band structure of a metal and n-type semiconductor junction in equilibrium. In the absence of any external voltage at the junction, the Fermi energy

level (EF) stays constant [30]. This condition leads to band bending, resulting in the forming a space charge region represented by a width W. The Schottky barrier height (φ_B), which hinders electron flow, is a key factor influenced by the work function of the metal (φ_M) and the electron affinity of the semiconductor (χ). The work function (φ_M) is the minimum energy necessary to remove an electron from the surface of a metal and move it into the vacuum (E_{vacuum}). In contrast, the electron affinity (χ) of a semiconductor is the energy difference between the E_{vacuum} and the bottom of the conduction band in the semiconductor.

2.1.1 Schottky-Mott Theory

The Schottky-Mott theory, proposed by Walter H. Schottky and Sir Nevill Francis Mott in the 1930s provides a fundamental framework for comprehending the formation of metal-semiconductor junctions. At the core of the Schottky-Mott theory is the concept of energy band alignment. There is an exchange of charge carriers (electrons or holes) between a semiconductor and a metal when they come into contact. The semiconductor's energy bands bend as a result of this interaction, forming a Schottky barrier at the M-S contact. The electron affinity (χ_{semi}) of the semiconductor and the work function (φ_M) of the metal both affect this Schottky barrier height.

2.1.1.1 Ideal Schottky Barrier

The ideal Schottky barrier heights for p- and n-type semiconductors are expressed by the following equations:

$$\Phi_{B_n} = \Phi_M - \chi_{semi} \tag{2.1}$$

$$\Phi_{B_p} = E_G - \Phi_M + \chi_{semi} \tag{2.2}$$

2.1.1.2 Limitations of Schottky-Mott Model

While the Schottky-Mott theory offers a valuable framework for understanding the formation of Schottky barriers, it has notable limitations. The model assumes perfect contact between the semiconductor and metal, neglecting any influences caused by gap states introduced by the metal, interface states, and surface states that can lead to Fermi level pinning (FLP). Due to this phenomenon, the ideal Schottky behavior deviates, leading to a significant Schottky barrier height (SBH) that is governed by the density of defect states and becomes independent of the metal work function [31], [32]. Therefore, it

becomes difficult to modify the SBH to get an ohmic contact. Additionally, the oxygen reactivity of AlN plays a crucial role in FLP. AlN exhibits a strong affinity for oxygen, leading to the formation of aluminum oxide (Al_2O_3) or other oxynitrides at the surface, even when present in trace amounts. This oxide layer introduces interface states that further contribute to Fermi level pinning resulting in discrepancies between the predicted and observed barrier heights. Therefore, it is often essential to explore more intricate models to address the complexities of real-world interfaces and the variations from idealized assumptions.

2.2 Ohmic Contacts to AlN

To maximize the potential of semiconductor devices, it is essential to establish ohmic contacts with low resistance and linear current-voltage (I-V) behavior with minimized parasitic losses. Achieving such contacts on wide bandgap III-nitride materials has been a significant challenge.

The efficacy of ohmic contacts is influenced by two key factors: the height of the Schottky barrier (ϕ_B) and the concentration of dopants in the semiconductor (N_D). The low electron affinity of AlN in the range of 0.6-1.9 eV, and the available range of work functions of the metals of ~1.9-5.3 eV [21] result in a significant barrier at the interface of AlN with any metal contact. Forming ohmic contacts on p-type AlN films is especially challenging due to the high work function needed for the metal contacts. Furthermore, at real interfaces, defect states and often FLP by those states weaken the correlation between SBH and metal work function, hindering SBH engineering for ohmic contact formation. Therefore, simply depositing metals on the semiconductor is insufficient to achieve ohmic contacts to AlN. So, alternative approaches such as high doping resulting in tunnel barriers (explained in the next sub-section) are employed to attain ohmic contacts. Appropriate metal contact stacks can significantly improve contact characteristics by narrowing the Schottky barrier, thereby facilitating tunneling. Thermal annealing conditions also play a vital role in enhancing contact performance and ensuring optimal electrical conductivity.

The performance of ohmic contacts is typically evaluated through the specific contact resistivity (ρ_c), outlined in Equation 2.3, it represents the relationship between the current

density (J) and the applied voltage under zero bias conditions. It essentially quantifies the resistance per unit area, expressed in Ω.cm².

$$\rho_c = \left(\frac{\partial V}{\partial J}\right)_{V=0} \tag{2.3}$$

2.2.1 Carrier Transport Regimes

There are three different mechanisms for carrier transport across the metal-semiconductor junction. These mechanisms depend on the semiconductor's doping level (N_d), which influences the width of the space charge region. The depletion width decreases as the doping density is increased allowing tunneling of carriers through the junction, i.e.,

$$W \propto \frac{1}{\sqrt{N_d}} \tag{2.4}$$

In lightly doped semiconductors, the Schottky barrier presents a significant obstacle for carriers to flow across the metal-semiconductor junction. However, thermal energy provides an essential driving force. It excites carriers to energy levels above the barrier, enabling them to hop across into the semiconductor (Fig. 2.2a). In heavily doped semiconductors, the depletion region narrows significantly (as dictated by Equation 2.4) so this allows the carriers to pass directly through the barrier via tunneling (Fig. 2.2b). The depletion width is too large for direct tunneling of carriers for intermediate doping levels. However, with added thermal energy, carriers can be thermally excited to an energy level above the level of mFermi energy (E_F), where the depletion width becomes sufficiently thin to tunnel through the barrier called the thermionic field emission (Fig. 2.2c).

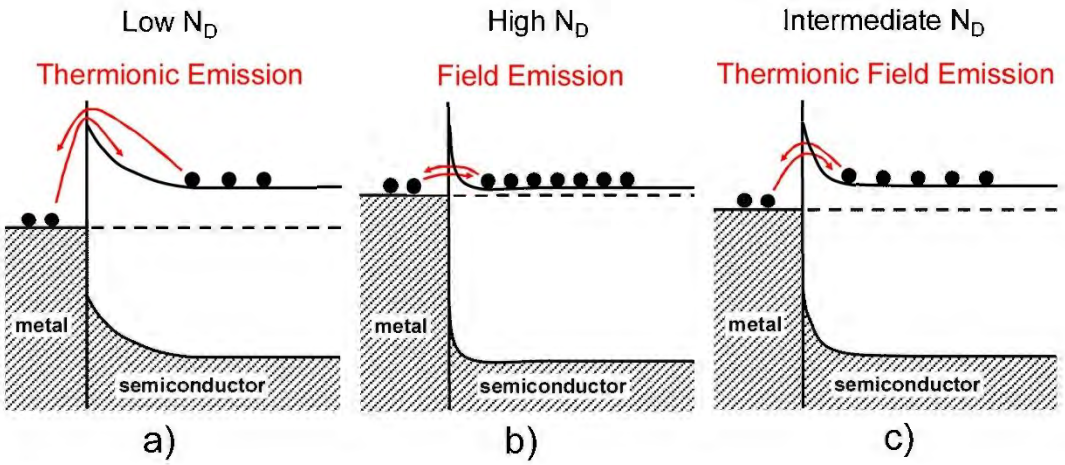

Figure 2.2: (a) Thermionic Emission (b) Field Emission (c) Thermionic Field Emission [33]

The primary carrier transport mechanism through the Schottky barrier can be identified using the characteristic energy E_{00}, defined as:

$$E_{00} = \frac{qh}{4\pi}\sqrt{\frac{N_d}{K_s \varepsilon_0 m^*_{tun}}}\ [eV] \tag{2.5}$$

where h, K_s, and m^*_{tun} are the Plank's constant, dielectric constant, and tunneling effective mass respectively. By comparing E_{00} with the thermal energy kT, we can determine the dominant transport mechanism: thermionic emission prevails when kT is much greater than E_{00}; thermionic-field emission is indicated when kT is approximately equal to E_{00}; and field emission dominates when kT is much less than E_{00}.

2.3 Junction Barrier Schottky (JBS) Diode

2.3.1 Introduction

The current mainstream of diodes encompassing the metal-semiconductor junction diodes / Schottky barrier diodes (SBDs) and PN junction diodes are considered the fundamental components for high-efficiency power electronics systems. Bipolar PiN diodes are characterized by high voltage handling capability, minimal leakage current, and high-temperature performance but they suffer from high forward voltage drop, resulting in significant conduction losses [34]. While unipolar SBDs offer advantages such as low forward voltage drop, high-frequency switching, and minimal reverse recovery current,

they exhibit drawbacks like increased leakage current and lower breakdown voltage, which result from Schottky barrier reduction and electron tunneling effects [35]. An advanced structure is the Junction Barrier Schottky (JBS) diode, sometimes referred to as the pinch rectifier, which is a unipolar device first developed using silicon technology [36], [37]. It combines the merits of both the SBDs in forward bias with their fast-switching characteristics and PiN diodes in reverse bias, eliminating their drawbacks [38]. The JBS diodes are particularly appealing for WBG materials.

2.3.2 I-V Characteristics

The JBS diode combines the low forward voltage drop characteristic of Schottky diodes with the high breakdown voltage and low reverse leakage current typical of pin or pn junction diodes, as illustrated in Figure 2.3.

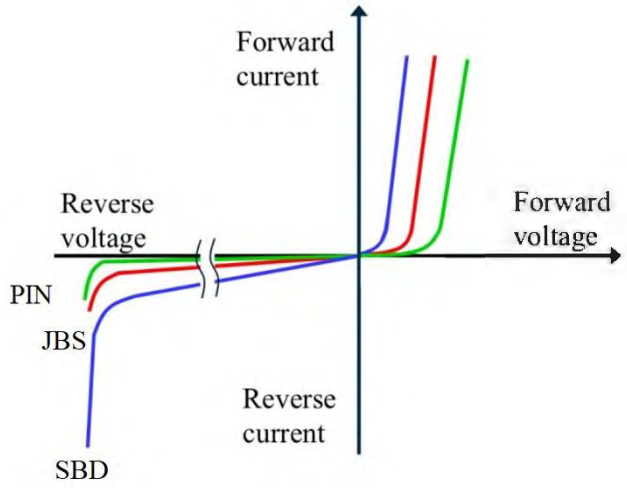

Figure 2.3: Current-Voltage Characteristics of PIN, SBD, and JBS Diodes

2.3.3 Diode Design

The JBS diode comprises Schottky diode areas linked in parallel with pin diodes at a specific spacing. This design shields the Schottky interface from the strong electric field during reverse bias preventing premature breakdown while preserving the forward bias characteristics. The Schottky barrier diode determines the forward voltage characteristics, whereas the pin diodes provide high breakdown performance and limit reverse leakage [36], [37]. Figure 2.4 presents a comparison of the structures of Schottky barrier diodes, PIN diodes, and JBS diodes.

As shown in Figure 2.4, the JBS diode consists of p+/n-/n+ regions. The structure includes an unintentionally doped (UID) n^- epitaxial layer, also referred to as the drift layer, which is formed on top of a uniformly doped n^+ substrate. The UID layer allows the efficient transport of charge carriers while minimizing leakage currents. A buried p^+-grid is integrated within the structure, featuring a uniform doping concentration. This grid improves the diode's ability to block voltage and reduces the concentration of electric fields at the surface. The distance between adjacent p^+ regions is designed to vary periodically, optimizing the balance between forward conduction and reverse blocking performance. An ideal ohmic contact is established on the n^+ substrate at the bottom of the device to facilitate efficient current injection. At the top, a Schottky contact with a specific work function is formed, enabling low forward voltage drop characteristics. This unique configuration allows the JBS diode to combine the benefits of both PIN and Schottky diodes, offering increased reverse voltage blocking while maintaining a low forward voltage drop, which makes it ideal for a range of power electronic applications.

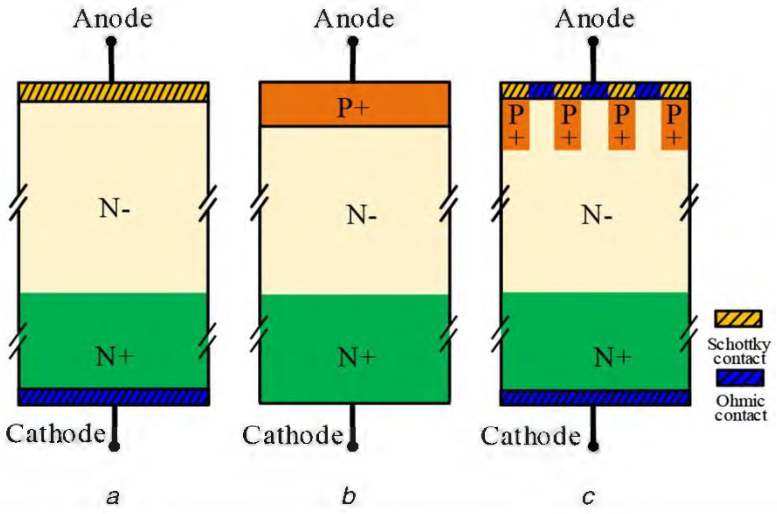

Figure 2.4: Diagrams illustrating the structures of (a) Schottky diode, (b) PIN diode, and (c) JBS diode [39]

2.3.3.1 Design Considerations

The characteristics of Junction Barrier Schottky (JBS) diodes are significantly influenced by several design considerations. The following are the key factors that impact their performance:

- ***Inter-p^+ region spacing:*** The p^+ region width (w) and the inter-p^+ Schottky spacing (s) are critical design parameters that impact the performance tradeoff of JBS diodes regarding reverse leakage current and forward voltage drop. Wider spacing improves forward current flow but allows for a stronger electric field at the Schottky contact leading to higher leakage current. Conversely, narrower spacing helps decrease the leakage current but results in increased current crowding and higher forward conduction losses [40]. By optimizing this trade-off, the diode can be tailored to exhibit predominantly PiN, JBS, or Schottky diode behavior. Furthermore, the doping level, shape, and p^+ region depth also impact the characteristics of the JBS diodes.
- ***Drift region:*** For JBS diode design to achieve the ideal balance between critical voltage and on-resistance, the drift region thickness and doping concentration must be carefully chosen. A thicker, lightly doped drift region enables higher breakdown voltage by facilitating significant depletion and improved electric field tolerance [41], but lower doping levels result in potential current crowding caused by the large depletion regions from the p^+ grid at the Schottky interface, and increased layer thickness contributes to higher resistance, both leading to increased forward conduction losses [42].

2.3.4 Forward Conduction

The forward conduction in JBS diodes involves unipolar conduction through thermionic emission over the Schottky barrier [43], [44] and bipolar conduction through the minority carrier injection from the p^+ grid into the n^--drift layer forming the PN junctions [44] but their primary mode of conduction is governed by thermionic emission, similar to Schottky barrier diodes. This leads to majority carrier current flow beneath the Schottky regions with the voltage drop being governed by the height of the M-S Schottky barrier (SBH), that results in a low turn-on voltage and improved forward current density. The Schottky spacing between the p^+ regions in a JBS diode is a critical parameter in controlling the influence of these conduction mechanisms.

In the forward operation of a JBS diode, the key parameters are the specific on-resistance ($R_{on,sp}$) and the forward voltage drop (V_F). The total R_{on} of a JBS can be represented as a total of component resistances as indicated in Equation 2.6.

$$R_{on} = R_{ch} + R_{spread} + R_{drift} + R_{sub} + R_{con} \quad (2.6)$$

Here, R_{ch} represents the channel resistance, R_{spread} is the additional spread resistance that arises due to results from the p+ regions' non-uniform current spreading, R_{drift} represents the drift layer resistance, R_{sub} denotes the resistance of the substrate, and R_{con} represents the contact resistance. Typically, R_{con} is significantly lower than the R_{sub} and can be neglected. The JBS diode's forward bias voltage drop is described by Equation 2.7.

$$V_F = \frac{\eta kT}{q} ln\left[\frac{(s+w)\cdot J_F}{(s-2d)\cdot A^{**}T^2}\right] + n\phi_B + R_{on}J_F, \quad (2.7)$$

where η represents the ideality factor, q denotes the elementary charge, T stands for temperature, k represents the Boltzmann's constant, ϕ_B denotes the Schottky barrier height, and J_F is the forward current density at voltage V_F, A** represents Richardson's constant, and s and w denote the Schottky spacing and p^+ region width, respectively.

2.3.5 Reverse Operation

In reverse blocking mode, a p^+n^- junction formed by the p^+ grid in a JBS diode expands its depletion region in reverse bias and pinches off the drift region at the lower end of the Schottky channel. This depletion region is a barrier that screens the Schottky contact from strong electric fields. A low e-field at the Schottky interface effectively suppresses the field emission or tunneling current and keeps it lower than the thermionic current, minimizing the overall leakage current. The critical electric field migrates away from the Schottky interfaces and concentrates at the edges of the p^+ regions. The drift region then primarily sustains the rising voltage. Consequently, breakdown now takes place at the periphery of the p^+ areas rather than the Schottky interfaces between them. Therefore, before reaching the critical voltage of the standard Schottky barrier diode (SBD), the pinching of the Schottky channel in a JBS diode extends the critical voltage of the JBS diode beyond that of the SBD [45], [46]. The inter-p^+ region spacings need to be precisely designed to guarantee that pinch-off occurs before the electric field at the Schottky contact reaches a level where it can cause significant leakage from tunneling. By optimizing this spacing in

the p^+ grid design, it is possible to reduce the leakage currents without a significant increase in the on-resistance of the JBS diode.

The pinch-off voltage (V_p) and doping concentration (N_d) of the Schottky channel are the main factors influencing the electric field at the Schottky interface.

$$E = \sqrt{\frac{2qN_d}{\varepsilon_s}(V_p + V_{bi})} \tag{2.8}$$

Where ε_s is the semiconductor's dielectric constant and V_{bi} represents the built-in voltage. The pinch-off voltage, at which the depletion regions meet, is influenced by the inter-p^+ region spacing (s).

$$V_p = \frac{qN_d s^2}{8\varepsilon_s} - V_{bi} \tag{2.9}$$

The leakage current in a JBS diode arises from tunneling effects, Schottky barrier lowering, and thermionic emission. The equation below describes the leakage current associated with thermionic emission:

$$J_{T.E} = A^{**}T^2 e^{\left(\frac{-\Phi_B}{kT}\right)} \tag{2.10}$$

where $A^{**}=4\pi qk^2m^*/h^3$ is Richardson's constant whereas T represents the absolute temperature. Since, at high reverse voltages, the exponential factor approaches zero.

$$J_{T.E} = Js \tag{2.11}$$

The leakage current density caused by the lowering of the Schottky barrier can be expressed as:

$$J_{Sch} = Js.\, e^{\left(\frac{-\nabla\Phi_B}{kT}\right)} \tag{2.12}$$

The tunneling current density,

$$J_{tunnel} = f(E, \Phi_B) \propto E^2 e^{\left(-8\pi\sqrt{2m^*\Phi_B}^{3/2}/3hqE\right)} \tag{2.13}$$

The JBS structure effectively mitigates both tunneling current components and Schottky barrier lowering by reducing the e-field at the Schottky interface. Consequently, field-dependent tunneling becomes the primary leakage mechanism to address through JBS grid optimization.

2.3.6 Applications

The combination of low forward voltage drop, high reverse breakdown voltage, and fast switching capabilities make JBS diodes suitable for a variety of applications across different fields.

- ***Power Electronics:*** One of the primary applications of JBS diodes is in power electronics. Their low conduction losses and high thermal stability make them ideal for use in power supplies, converters, and inverters. JBS diodes are often utilized in switch-mode power supplies (SMPS), where efficient power conversion is critical. These devices enable high-frequency operation and reduce energy dissipation during switching, leading to improved overall system efficiency.
- ***Renewable Energy Systems:*** JBS diodes are used in bypass diode designs in renewable energy systems, such as solar photovoltaic (PV) installations. These diodes play a vital role in preventing power loss from shaded solar cells, ensuring that the entire array maintains efficiency under varying environmental conditions. The capability of JBS diodes to handle significant reverse voltage makes them suitable for protecting solar inverters from high-voltage transients.
- ***Inductive Load Switching:*** JBS diodes find applications in circuits involving inductive loads, such as motors and transformers, due to their ability to effectively manage voltage transients. In scenarios where inductive kickback can damage components, JBS diodes provide a reliable pathway for the excess current, protecting sensitive components while enhancing circuit reliability.
- ***RF and Microwave Applications:*** In radio frequency (RF) and microwave applications, JBS diodes are used in mixer circuits and as frequency multipliers due

to their fast response time and low reverse recovery time. Their ability to operate efficiently at high frequencies and with minimal signal degradation makes them valuable in telecommunications and signal processing.

- ***Automotive Applications:*** The automotive industry is increasingly adopting JBS diodes in electric and hybrid vehicles. Their fast-switching speed and high efficiency contribute to the overall performance of powertrain systems and contribute to reducing weight by minimizing the heat sink requirements. Additionally, JBS diodes are utilized in battery management systems to ensure safe and efficient operation during charging and discharging cycles.

CHAPTER 3

LITERATURE REVIEW

An extensive summary of the state-of-the-art in AlN-based technologies is given in this chapter, focusing on key aspects like thin film deposition, doping strategies, and metal contact formation. The deposition of AlN films on silicon substrates via magnetron sputtering will be discussed, followed by an exploration of the challenges and advancements in achieving n-type and p-type conductivity in AlN.

Even though AlN growth and doping have made great strides, the development of reliable contacts remains a critical challenge due to the material's inherent properties. Reliable contacts play a vital part in realizing the full potential of AlN-based devices. A significant focus is placed on metal contacts to AlN, a topic that has received limited attention in the existing research, highlighting the need for further investigation in this area.

3.1 AlN Film Deposition on Silicon Substrate via Magnetron Sputtering

For the first time, G. F. Iriarte [25] reported the magnetron effect on AlN thin film growth deposited via reactive sputtering. They measured the AlN (0002) peak FWHM values at different locations across the Si substrates of diameter = 100 mm on which AlN films were grown. The experiment was performed in two series. In the first, four distinct 100-silicon substrates were processed at 2, 4, 6, and 8 mTorr of pressure. In the second series, the pressure was maintained at 6 mTorr, and the effect of ionic bombardment on the previously discovered magnetron effect was studied with voltages of 50, 60, and 90 V applied to the wafers.

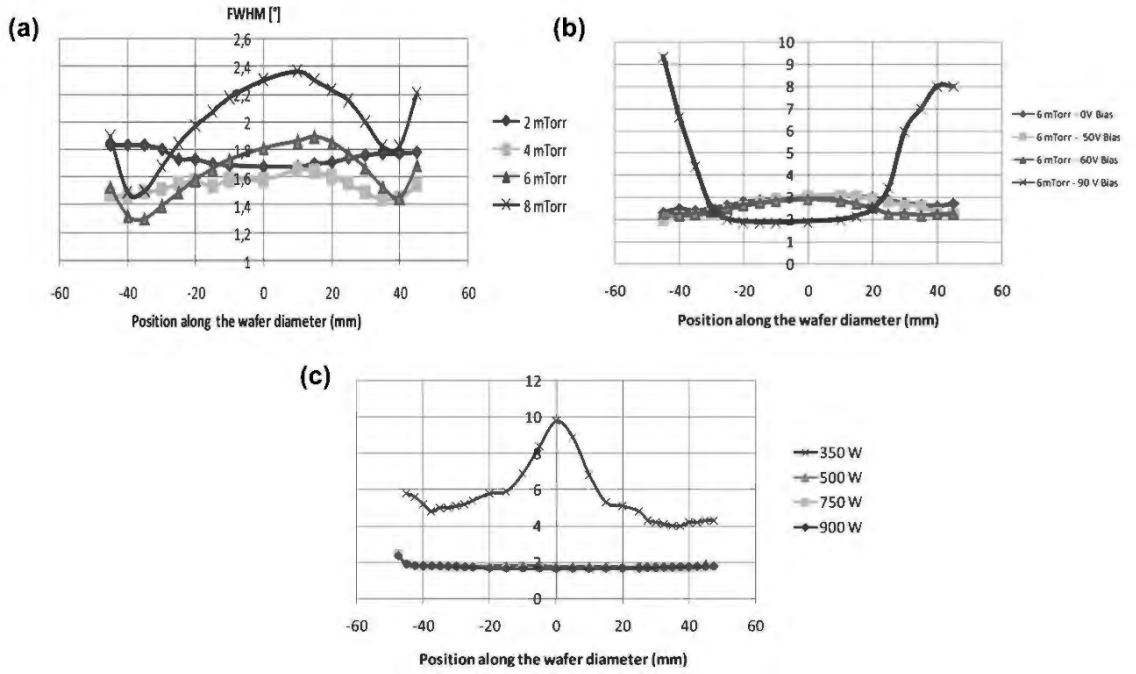

Figure 3.1: FWHM measured along the wafer diameter as a function of (a) Processing pressure (b) Substrate voltage and (c) Discharge power [25]

Other factors like Ar/N_2 ratio, power of cathode, substrate temperature, and substrate voltage variation effects were also studied independently. In all cases, the FHWM remained constant. The c-axis (crystallographic) orientation degree of the 0002-peak changes at substrate locations directly coinciding with the target magnetron for particular parameters only like increased pressure of processing and bias voltage or using a low discharge power, resulting in influencing the AlN thin films growth.

J.X. Zhang et al. [47] reported the formation of high-quality AlN thin layers on silicon-100 and 111 wafers using reactive sputter deposition as a layer of buffering material for ensuing epitaxial GaN layers formation. The sputtering was performed for 1 hour at discharge powers in the 200- 500 W range. The temperature of the substrate was set to 350 ºC with approximately 200-260 nm deposited film thickness and the target and the substrate were separated by 8cm. The XRD results shown in Figure 3.2 revealed that the AlN layers formed on silicon-100 wafers indicate preferred orientations at 200 W discharge power, compared to mixed (1000) and (0002) orientations at 400 W discharge power. The films though exhibit high c-axis orientation when discharged at 300 and 500 W. The film does

not show a preferential orientation at inadequate discharge powers, e.g., 200 W. When the power is raised to 300 watts, the film exhibits a high (0002) crystallographic orientation. However, as the power increases above 400 W, causing the gradual increase of (11-20) orientation which results in mixed (11-20) and (0002) orientations in the AlN film.

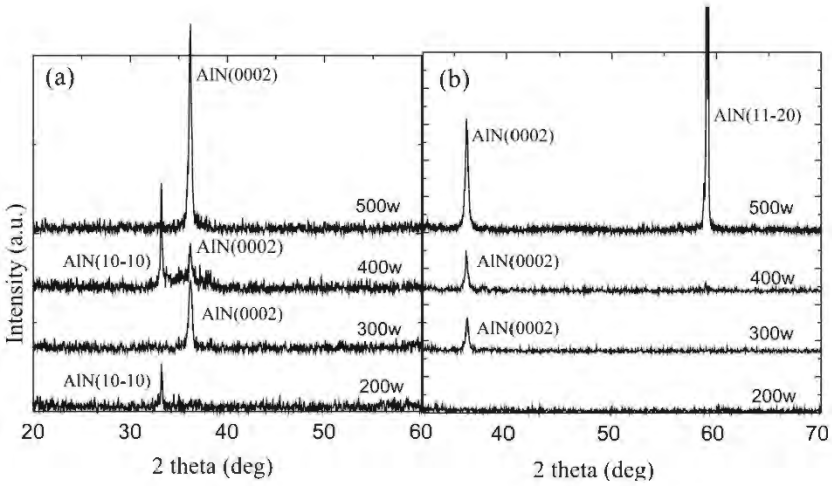

Figure 3.2: XRD patterns of AlN layers grown on silicon 100 and 111 wafers at different sputtering discharge powers [47]

The XRD analysis indicates that the preferential orientation of the layers on silicon (111) wafers is easier to control as compared to silicon (100) wafers. Also, the FWHM of the 0002-peak varies with discharge power and substrate orientation. FESEM studies revealed that the size of the crystallites enlarges as the power of RF sputtering increases due to a rise in the reactive species' mobility. Then, utilizing these crystallite sizes, the following formula was employed to compute the strain in the films:

$$\varepsilon = \frac{\beta}{tan\theta} - \frac{k\lambda}{dsin\theta}$$

It was discovered that the strain in the fabricated films is significantly influenced by the Si wafers orientation. The huge mismatch of the silicon (100) and AlN (0001) lattices is a major contributor to the substantial strain in the deposited layers and the strain was not significantly affected by discharge power whereas with increased discharge power, strain clearly rises for silicon (111) substrates and it is mainly the residual strain introduced because of the thermal mismatch and crystallographic defects.

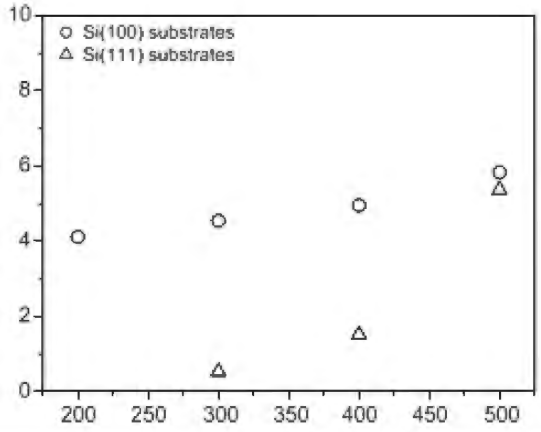

Figure 3.3: Strain in AlN layers grown on silicon wafers dependent on the sputtering power [23]

Badis Riah et al. [48] examined the influence of the orientation of Si wafer as well as a buffer layer of AlN on the hetero-epitaxial deposition of ~600 nm-thick AlN thin layer fabricated via direct current magnetron sputtering at low temperatures. A buffer layer of AlN of 1 nm thickness was formed on Si (111) substrate by MBE. For sputter deposition of the AlN films, the target was kept 37 mm away from the wafer, the pressure remained unchanged at 0.3 Pa, the Si wafer temperature was around 150 ºC with N_2 gas concentration set at 55%. Various tools were used to investigate the buffer layer's impact on the AlN film's quality including a Raman spectrometer, HRTEM, XRD and SEM. Profilometry was used to quantify the thickness and inherent stresses of the layers by determining the curvature of the wafer prior to and following the growth process. The thickness was calculated using the height difference between the region covered by the fabricated film and the other region that was initially concealed while fabrication. The following expression was used to determine stress:

$$\sigma = \frac{E}{6\,(1-v)} \frac{t_s^2}{t_f} \left(\frac{1}{r_c} - \frac{1}{r_u} \right)$$

The AlN films' crystalline quality improved as a result of the buffer layer. The FWHMs of the (0002) curves were reduced by utilizing the AlN buffer layer. The pole figures from XRD showed heteroepitaxial deposition of AlN thin films as well as a high (0001) texture of fibers for both (111) and (100) silicon wafers. When compared to films grown on silicon (100) and (111) wafers, the SEM results suggested that the AlN film fabricated using the buffer layer on silicon (111) wafer had better columnar crystal properties. Raman

spectroscopy revealed compressive stress relaxation for the AlN film formed on Si (111) and Si (100), and under tension when formed using an AlN buffer layer. HRTEM verified the heteroepitaxial deposition of AlN thin layers on AlN buffer/Si (111) wafers.

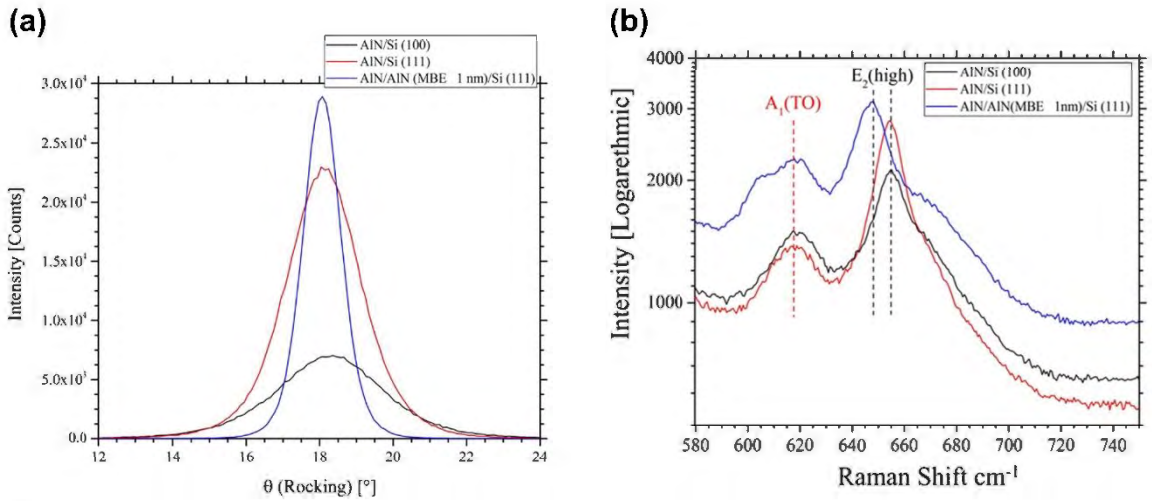

Figure 3.4: (a) XRD patterns of the θ-θ scans and (b) Raman spectra of AlN layers formed on various substrates [48]

M. K. Sandager et al.[49] conducted a thorough investigation in which they grew wurtzite AlN thin layers on large silicon (111) wafers (100mm) using reactive DCMS at low temperatures. XRD, AFM, SEM, and profilometer were used to examine how the power of magnetron, pressure, and N_2:Ar affected the deposited layers' structures. For all the samples, tensile stress and crystallographic orientation were observed in the films. It was discovered that at 0.2 Pa processing pressure and 50% inert gas ratio, AlN films of high crystalline quality can be attained. To achieve higher growth rates, strong magnetron powers in the range of 900 to 1200 W were required, but they resulted in increased stress in the layers. The study's findings revealed that magnetron power is a crucial factor for increasing the growth rate and it also gives the effect of increased substrate temperature simultaneously by increasing the incident atoms' kinetic energy and enhancing adatom surface diffusions. Another crucial factor that affects crystallinity and also influences the rate of deposition is the proportion of reactive to process gases (N_2/ Ar). Compromise has to be made on different growth conditions to achieve a high deposition rate, minimal stress, reduced surface roughness, and good crystalline quality. simultaneously. The following

figure shows the results of this work suggesting some of these compromises that could be made to achieve high-quality AlN films.

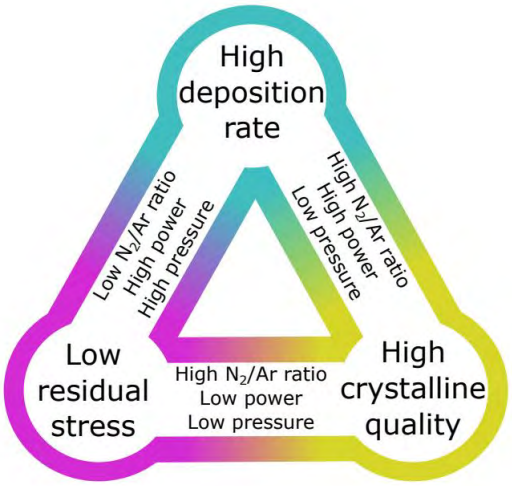

Figure 3.5: Diagram illustrating the relationship between sputtering parameters and crystalline quality, residual stress, and deposition rate [49]

The optimum method to grow good crystalline quality and smooth films is to utilize a low processing pressure with a high flow ratio of inert gases. But target poisoning is promoted under these conditions resulting in retardation in the film growth rate. The ideal ratio of deposition rate and residual stress can be attained by adjusting the magnetron power. However, this study concentrated on deposition at a reduced inert gas ratio of 27%, which allows the conclusion that average but reasonable quality layers (concerning surface roughness and crystallinity) could be produced whilst keeping a high growth rate first as a priority.

In-Su Shin et al. [50] examined the deposition of single-crystalline AlN film on a silicon (111) substrate via DCMS at room temperature. To grow AlN on Si substrate epitaxially at low temperatures, the mismatch of the lattices was reduced by introducing an Al buffer layer of 5 nm thickness in between. Four samples were prepared by depositing 100 nm AlN films on 2-inch Si (111) at room temperature to investigate how DC power, sputtering pressure, and Al pre-deposition affect the AlN films' quality. High-purity Ar and N_2 were used as the sputtering and reactive gases, respectively with a 1:1 ratio for all the samples. The following table shows the parameters selected for AlN growth on silicon wafers.

Table 3.1: Conditions of AlN deposition on Si substrate via Magnetron Sputtering [50]

Sample	Al Pre-deposition	DC Power (W)	Pressure (Pa)
A	No	400	0.399
B	No	400	0.133
C	No	600	0.133
D	Yes	600	0.133

The XRD θ–2θ scans of the templates suggested that sputtering pressure acts as a significant determinant of the AlN layer's orientation as 0.399 Pa gave the AlN ($10\bar{1}1$) peak while AlN (0002) peak was shown at a pressure of 0.133 Pa. For the films grown with a greater DC power of 600 W while maintaining the same pressure, it was noticed that the intensity (shows how well the AlN crystallites are aligned) of the AlN (0002) peak increased. The intensity of the peak was further enhanced for the sample on which the Al pre-deposition procedure was performed. XRD ϕ-scan profiles suggested that high DC power and Al pre-deposition are necessary for depositing a single-crystalline AlN layer on a silicon wafer epitaxially. The AlN and aluminum layers, as well as the silicon wafer, were discovered to have AlN [$0\bar{1}00$] ∥ Al [$0\bar{1}1$] ∥ Si [$11\bar{2}$] and AlN [$11\bar{2}0$] ∥ Al [011] ∥ Si [$1\bar{1}0$] as the orientation relationship based on the HR TEM analysis which signifies the epitaxial deposition of AlN. Also, for AlN [$1\bar{1}00$] ∥ Al [$0\bar{1}1$], the mismatch of the lattices was determined as 6% while for AlN [$11\bar{2}0$] ∥ Al [011], it was 8%, which are substantially lesser than the 19% mismatch between AlN [$11\bar{2}0$] and Si [$1\bar{1}0$] which also confirms the epitaxial deposition of AlN. On the AlN/Al/Si and AlN/Si templates, the GaN layers were also formed via MOCVD at 1040 °C temperature and 5 kPa pressure. As expected, it was found that the polycrystalline A rough-surfaced GaN film was deposited on the AlN/Si substrate whereas on the AlN/Al/Si substrate (with Al pre-deposition), a single-crystalline layer of GaN with a mirror-like smooth surface was achieved.

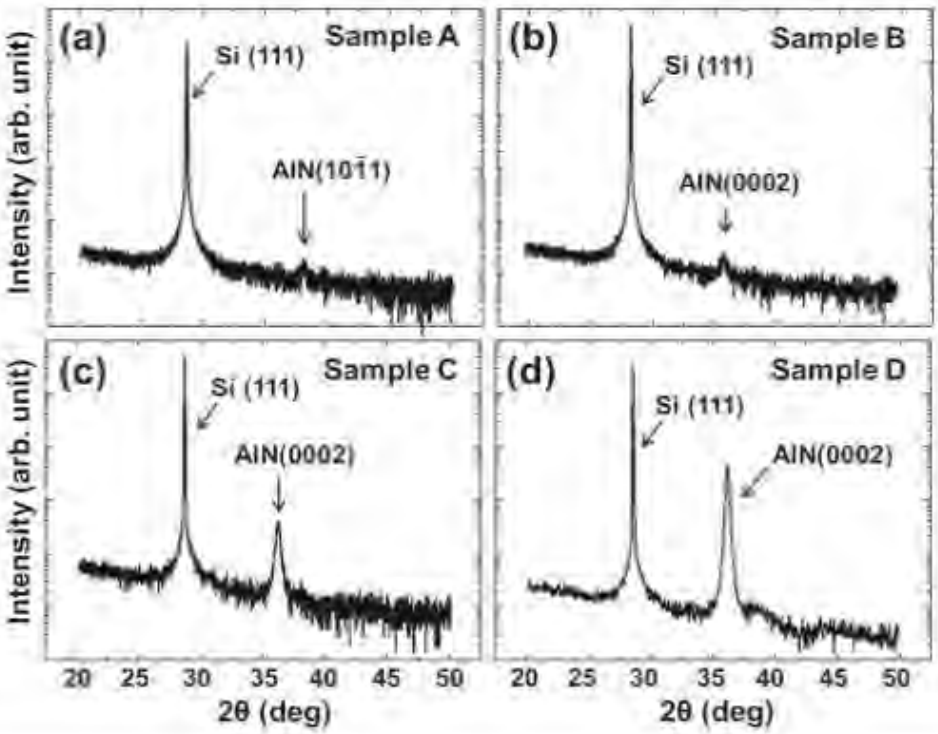

Figure 3.6: XRD θ–2θ scans for samples (a) A (b) B (c) C and (d) D [50]

Table 3.2 summarizes the relevant reported works on AlN thin film deposition on silicon substrates using magnetron sputtering techniques. This table provides a comprehensive overview and an insightful comparison across different studies and highlights trends in deposition parameters that significantly influence film quality and performance.

Table 3.2: Summary of relevant reported works on AlN thin film deposition on Si substrate via Magnetron Sputtering

Authors [ref] (Year of Publication)	RF	DC	Plasma Power (W)	Substrate Temp. (°C)	Flow Rate (sccm)	XRD Peak (°)	FWHM (°)	Thickness	Deposition Rate (nm/min)
Zhang et al. [47] (2005)	✓		500	350	-	36	0.327 (diffraction peak)	200-260 nm	-
Iriarte et al. [51] (2003)		✓	900	200	Ar/N_2 = 20/45	36	1.65 (rocking curve)	2 µm	30
Medjani et al. [52] (2006)	✓		150	RT	18 sccm total, 2.5 sccm for N_2 at 14%	-	-	1-1.7 µm	18-27
Jiao et al. [53] (2014)	✓		150	Water-cooled	60 sccm (1:3)	36	-	1.2 µm	-
Panda et al. [54] (2017)		✓	200	400	4:1	33.2 (100-AlN)	140.8 arcsec = 0.0391° (rocking curve)	1 µm	-
Das et al. [55] (2021)	✓		250	350	23% N_2	33.26	0.36 (diffraction peak)	700 nm	7
Choi et al. [56] (2001)	✓		200	250	12 (1:3)	36	-	12.9 nm	-
Jin et al. [57] (2012)		✓	270	430	(50 Ar + 50 N_2) sccm	36	2.259 (rocking curve)	1 µm	20.86
Han et al. [58] (2020)		✓	1200	RT	30 sccm (50% N_2)	36	0.34 (diffraction peak)	150 nm	-
Yin et al. [59] (2022)		Pulsed DC	3k	200	(20 + 100) sccm	36	2.66 (rocking curve)	300 nm	42
Li et al. [59] (2019)		✓	1200	RT	(15 + 15) sccm	36.02	0.325 (diffraction peak)	122 nm	33

Khan et al. [60] (2015)		✓	200mA, 800V	500	10 (60% N_2/ N_2+ Ar)	36.02	0.295 (diffraction peak)	296 nm	7.3
Wei et al. [61] (2014)	✓		200	<150 (no heating)	(5 + 5) sccm	35.96	0.466 (diffraction peak)	18.3 nm	24.7
Duquenne et al. [62] (2007)		✓	100	RT	12.5 (15% N_2/ N_2+Ar for crystalline orientation)	36	0.44 (diffraction peak)	0.5 µm	33.3, 18.3
Cheng et al. [63] (1996)	✓		300	350	12 sccm (75% N_2)	36	0.243 (diffraction peak)	-	25
Han et al. [64] (2012)	✓		200	300	0-20/0-20 sccm (70% N_2/Ar)	35.94	0.30 (diffraction peak)	-	-
Oliveira et al. [65] (2004)	✓		200	310	50/50 %	32.95, 36.06	0.073 (100-AlN)	680 nm	5.7
Stoeckel et al. [66] (2014)		Pulsed DC	865	350	80% N_2	36	0.39 (diffraction peak)	0.5-0.6 µm	0.204
Phan and Chung [67] (2011)		Pulsed DC	-	25	90% N_2	36	0.21 (diffraction peak)	-	8
Singh et al. [68] (2011)	✓		300	25	1:1	35.85	0.32 (diffraction peak)	1 µm	10.5
Ababneh et al. [69] (2010)		✓	500, 300	150-200	0/50 sccm	36	0.26, 0.28 (diffraction peak)	500 nm	10.4, 6.4
Venkataraj et al. [70] (2006)		✓	500	RT	5-8 sccm (100% N_2)	36	0.4 (diffraction peak)	-	60
Bi et al. [71] (2014)		✓	460	400	22.8 (85% N_2)	36	1.63 (rocking curve)	1.8	7.5

Kar et al. [72] (2005)	✓		400	200	1:4	36	0.25 (diffraction peak)	500 nm	-
Abdallah et al. [73] (2008)		✓	-	25	30% N_2	36	0.25 (diffraction peak)	1.5 µm	40
Engelmark et al. [74] (2000)	✓		350	350	1:3 (10/30 sccm)	36	0.216 (diffraction peak)	1 µm AlN/SiO_2/Si	-
Assouar et al. [75] (2004)	✓		170	400	40% N_2	36	0.9 (rocking curve)	2 µm	-
Galca et al. [76] (2012)	✓		100	50	25% N_2 (40 sccm Ar)	35.9	0.22 (diffraction peak)	1 µm	17
Zhang et al. [47] (2005)	✓		300	350	-	36	0.3 (diffraction peak)	200-260 nm	-
Meng et al. [77] (2013)		✓	110	650	7:3	36.19	3.8 (rocking curve)	1.5 µm	-
Liu et al. [78] (2022)	✓		500	600	40 sccm (100% N_2)	36	< 0.716 (diffraction peak)	450 nm	-
Abdallah et al. [73] (2008)	✓		-	25	30% N_2	36	0.35 (diffraction peak)	1 µm	40
Ivanov et al. [79] (1995)			1 A, 295 V	900, 500	-	36.10, 35.91	0.072, 0.097 (diffraction peak)	1.3 µm	35
Aissa et al. [80] (2015)		✓	150	Ambient	40 sccm (35% N_2)	~36	1 (rocking curve)	500 nm	-

3.2 Challenges and Advances in AlN Doping

The realization of functional AlN-based electronic devices necessitates both n-type and p-type conductive materials. Achieving optimal doping concentrations within AlN has been a significant challenge due to factors such as the large dopant activation energy, low crystalline quality, and the formation of compensating defects like DX centers [81], [82], [83]. Early doping attempts primarily focused on group IV elements (Si, Ge, C, and SiC) but encountered limitations in achieving high doping levels and uniform distribution [13]. Recent advancements have addressed these challenges through refined growth techniques, annealing processes, and innovative doping strategies [14], [84], [85].

Silicon emerges as the most promising n-type dopant for AlN due to its favorable properties: low ionization energy, high solubility, and atomic radius compatibility [86], [87]. Conversely, p-type doping remains a formidable challenge attributed to low acceptor solubility and high dopant activation energy [82]. Beryllium, which has been proposed as the optimal p-type dopant according to first-principle calculations, is a promising dopant for AlN [14], [88], [89]. In addition, novel doping approaches such as co-doping and alloying have recently been investigated in the literature for further engineering of AlN's electronic and optical properties [90], [91].

3.3 Metal Contacts to AlN

Xuewei Li et al. [92] investigated the impact of annealing temperature on the properties of ohmic Ti(20nm)/Al(130nm)/Ni(50nm)/Au(150nm) contacts on undoped AlN layers deposited via e-beam evaporation. In this study, HVPE was employed for AlN film deposition on (0001) sapphire substrates. The Circular Transmission Line Measurement (CTLM) technique was utilized to determine the variation in specific contact resistance (c) between metal contacts. After their deposition, the contact layers were annealed at temperatures varying from 200 ºC-1000 ºC. For the annealing temperatures lower than 600 °C, 2 min was set as the annealing duration, and when it was higher than 800 °C, it was 30 s.

The impact of annealing on the electrical contacts' properties was investigated by analyzing the I-V behavior utilizing the two-point probe method. Further, SEM,

energy dispersive spectrometer (EDS), and XRD were performed to study the morphology and interaction of various metal layers respectively. The ohmic contacts' overall resistance was calculated using the following relation:

$$Rt = \frac{Rs}{2\pi}\left[ln\frac{R}{r} + L_T\left(\frac{1}{R} + \frac{1}{r}\right)\right]$$

For annealing temperatures less than 600 ºC, non-linear contacts were obtained whereas the contacts were ohmic for temperatures between 800- 950 ºC as a result of the Al–Au, Al–Ni, and Au–Ti alloys formation. The contact resistance was found to have an inverse relation with the increasing annealing temperature. The sample for which the annealing was performed at 950 ºC gave the lowest specific contact resistance of 0.379 cm^2. The ohmic contacts were thought to have formed due to the $AlAu_2$ and Au_2Ti alloys as a result of thermal annealing. Above 1000 ºC, the Ti/Al/Ni/Au/AlN contacts showed non-linear behavior again.

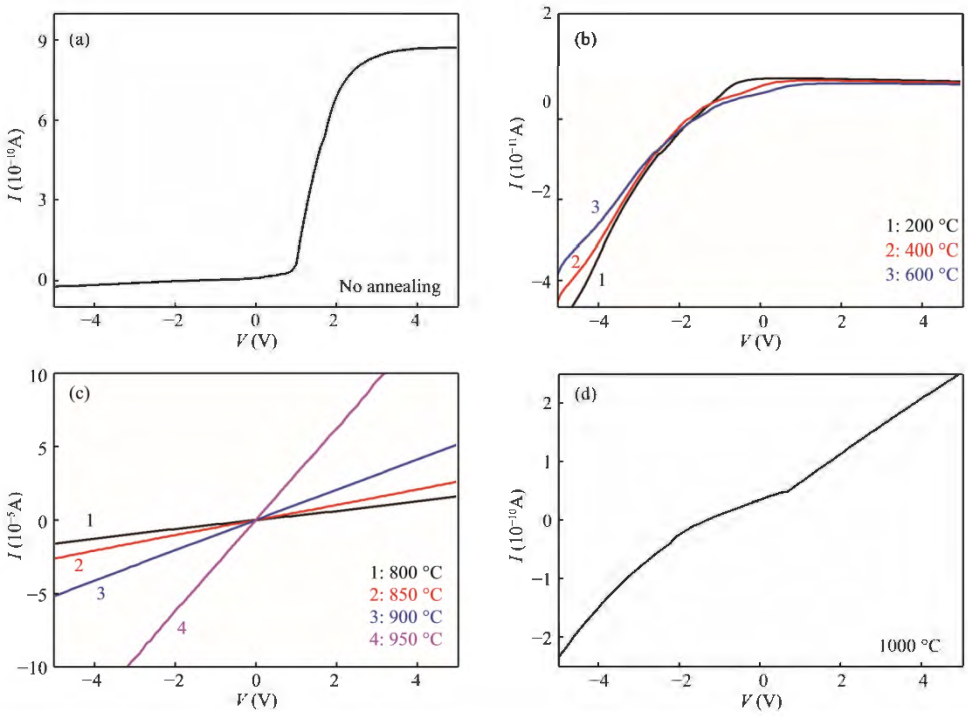

Figure 3.7: I-V characteristics of the Ti/Al/Ni/Au contacts on AlN layers (a) before annealing (b) annealed at 200- 600 ºC (c) at 800- 950 ºC and (d) beyond 1000 ºC [92]

Houqiang Fu et al. [27] demonstrated the novel AlN Schottky diodes on sapphire substrates with greater than 1 kV breakdown voltage. They grew AlN SBDs epilayers on SSP sapphire

(0001) wafers by MOCVD. The device is composed of an AlN buffer layer, a silicon-doped 300 nm n-AlN layer, a UID AlN underlayer (UL) 1 µm thickness with high resistance, and a UID 2 nm GaN cap layer as shown in Figure 3.8. AlN epilayers grown on sapphire wafers had the lowest recorded FWHM. HRXRD and AFM studies demonstrated that on sapphire substrates, AlN epilayers with decent surface morphologies and low density of defects were fabricated. Metal stacks with Ti/Al/Ti/Au (20/100/20/50 nm) for the ohmic contacts were produced via e-beam deposition and then thermally annealed for 30 seconds at 1000 °C in nitrogen using RTA whereas metal stacks with Pt/Au (30/120 nm) were fabricated for the Schottky contacts using electron beam evaporation. Using the transmission line method, a sheet resistance of 1.3×10^{3} ohms per square, a contact resistance of 2.8×10^{-5} Ω.cm^2, and good thermal stability over 500K were obtained exhibiting high ohmic behavior of the contacts. With the rise in temperature, there was a modest increase in contact resistance. At forward bias, With an on:off equals to 105, a small ideality factor equals to 5.5 at RT, and a V_{on} of 1.2 V, the AlN SBDs displayed promising rectifying performance. The diodes showed a critical voltage of up to 1 kV and a reverse leakage current of less than 1 nA.

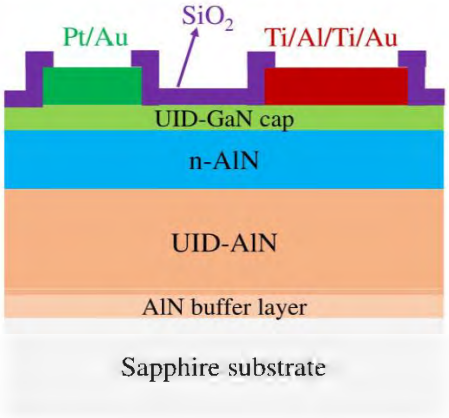

Figure 3.8: Structure of AlN SBDs grown on sapphire. Red and green regions represent the ohmic and Schottky contacts, respectively [27]

Habib Ahmad et al. [17] realized an AlN PN homojunction diode having a close to ideal V_{on} of approximately 6 V after successfully achieving p-type bulk conduction AlN having a concentration of holes of about 3.1×10^{18} cm^{-3} and remarkable improvement in bulk n-type conduction with electrons density up to 6×10^{18} cm^{-3}. The AlN: Si n-type films, AlN: Be p-type layers, and AlN homojunction devices were fabricated using PAMBE by

metal-modulated epitaxy on sapphire substrates. Pt/Pd/Au contact stacks (10/10/100 nm) were deposited on both p and n-type AlN films using electron-beam evaporation to conduct resistivity and Hall studies. The contacts were then subjected to annealing under pure N_2 at 800 °C for a min. for p-type AlN layers and at 875 °C for a min. for n-type AlN: Si layers via rapid thermal annealing (RTA). Using lithography and lift-off, the contacts were fabricated on large samples of 1 × 1 cm^2 at the corners. At 875 °C in a nitrogen atmosphere, the annealing period was one min., with ramping intervals of 60 seconds each. The impact of annealing on the samples was examined through I-V characteristics obtained using the four-point probe measurement. The circular transmission line measurements (CTLMs) were carried out indicating that having linear correlation coefficients larger than 99.9 percent, both p and n-type contacts exhibited ohmic behavior. The forward diode response was nearly ideal. The semi-log and linear voltage-current density plots of the p-n diode indicated a low breakdown voltage with a V_{on} of ~6V and quite a high series resistance.

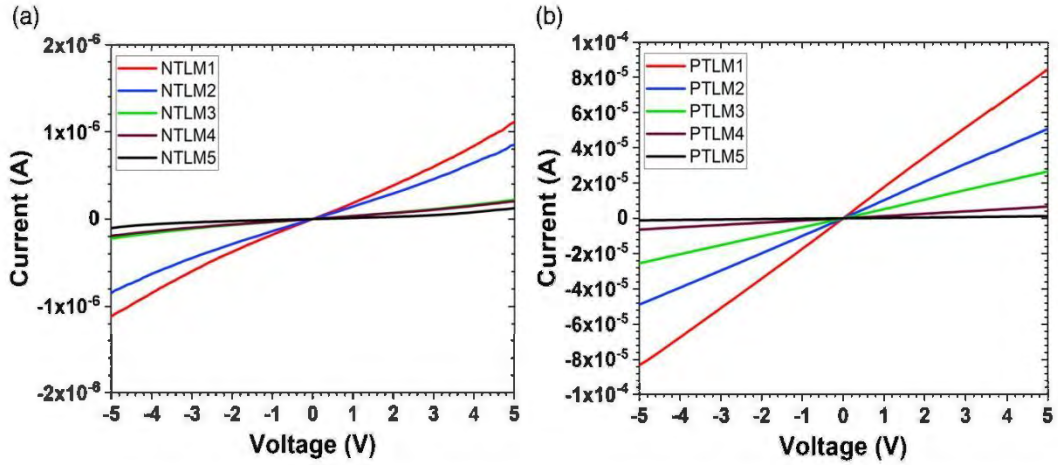

Figure 3.9: Circular transmission line measurements (CTLMs) of the PN diode for (a) n-type contacts and (b) p-type contacts [17]

Habib Ahmad et al. [93] achieved exceptional heteroepitaxial Pin, Schottky, and JBS diodes using the previously developed Beryllium-doped p-type AlN films having a concentration of holes of about 1 × 10^{18} cm^{-3}. This was accomplished by leveraging the internal crack formation in the heteroepitaxial AlN deposited on GaN to tailor the I-V characteristics of p-AlN:Be/i-GaN:Be/n-GaN:Ge diodes ratio of the Schottky diode surface area to that of the Pin diode is determined by the crack density. By introducing an MME-grown GaN:Be i-layer, the quasi-vertical diodes' current distribution

was illustrated preventing field congestion, high flow of current and mesa edges premature breakdown. Various pin diode structures were investigated via Silvaco TCAD for the GaN:Be films' current uniformity enhancement characteristics. By making the Be-doped GaN i-layer thicker to 10 µm and using a buried GaN:Be current spreading layer of 50 nm, the current flow distribution was enhanced to the maximum of the p-type contacts.

On MOCVD-grown n-GaN on sapphire substrates, 1 × 1 cm^2 template sizes were fabricated via MME. Pt/Pd/Au (10/10/100 nm), Ni/Au (50/50 nm) and Ti/Al/Ni/Au (30/130/50/50 nm) were formed as the contacts on AlN:Be, GaN:Mg and GaN:Ge respectively. The contact annealing was performed under pure N_2 for 1 min at 700 ºC for n-type GaN layers while for 1 min at 800 º C for p-type GaN layers.

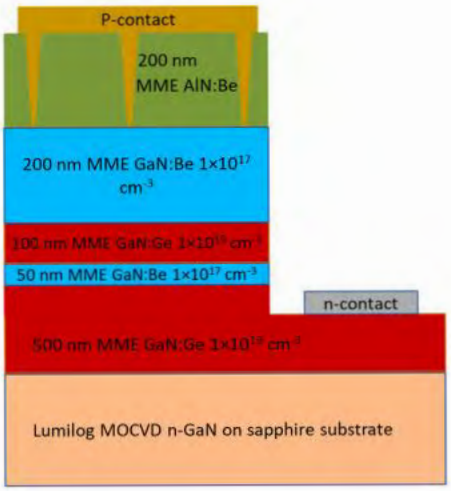

Figure 3.10: Schematic diagram of the AlN:Be/GaN:Be/GaN:Ge pin diode [93]

The growth conditions in only the top Be-doped AlN layer in the pin diodes were changed get the Pin, Schottky, and JBS behavior. GaN:Be and GaN:Ge layers were produced at 650 °C temperature, whereas AlN:Be layers were produced at 700 °C temperature. All of the films had a 1.3 III/V ratio. Distinct levels of deliberate cracking in the AlN layers were attained by varying the Beryllium doping concentration and the MME excess metal dosage. For the Schottky devices, at 200 A/cm^2 of current density, the intentional cracks allowed for a low V_{on} of around 1.5 V and a comparatively small V_{Br} between 12 to 15 V (about 30% of the theoretical 200 nm i-layer GaN-based pin diode with a theoretical V_{Br} of 50 volts). The pin diode performance with ~4 V of V_{on} at J = 200 A/cm^2 and a V_{Br}

between ~22 and 25 V (~50%) was obtained. The Junction Barrier Schottky diode, combining the benefits of Pin and Schottky diodes achieved a V_{on} = ~1.5 V at J = 200 A/cm^2 and a V_{Br} between ~17 and 20 V (~40% of the theoretical GaN breakdown voltage). The density of the intentionally introduced cracks in the diodes can also be varied by controlling AlN film thickness, substrate temperature and the III: V in addition to the metal dosage and Beryllium doping concentration.

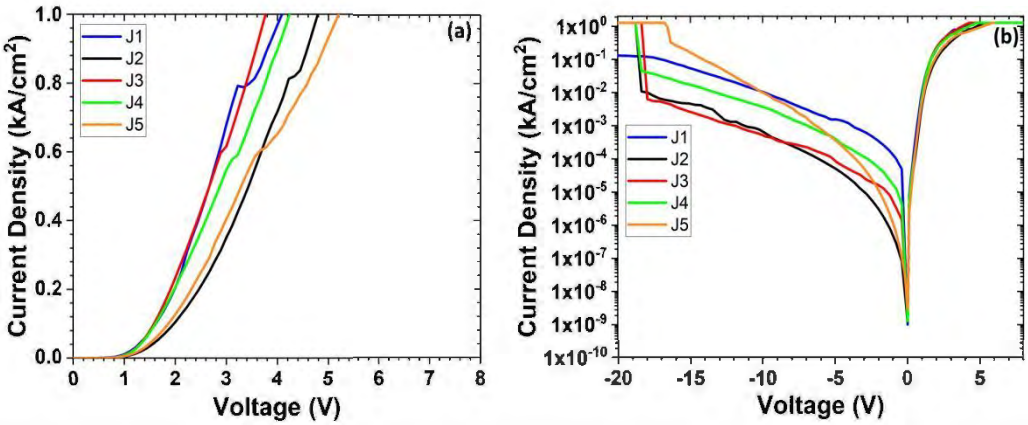

Figure 3.11: FB J-V curves of the JBS diode indicating (a) Von of ~1.5 V at J = 200 A/cm^2 and (b) V_{Br} between ~17 and 20 V [93]

Habib Ahmad et al. [14] achieved substantial bulk p-type conductivity of Be-doped AlN having room temperature hole concentration ranging from 2.3 × 10^{15} to 3.1 × 10^{18} cm^{-3}. The comparable atomic radii of Al and Be and hence low activation energy in combination with the Metal Modulated Epitaxy (MME) was used for films' growth enabling the incorporation of substantial Be concentration at low III/V ratios, optimum shutter cycles, and a low temperature of the substrate. On HVPE-grown AlN on sapphire substrates, the films were produced using Metal Modulated Epitaxy. 100nm thick AlN:Be films were fabricated using two distinct wafer temperatures of 600 °C and 700 °C with a III:V = 1.3. The MME dead time was kept at 8.5 s. To reduce the compensatory surface impurities, a 300 nm undoped AlN buffer film was also layered over the AlN template at 800 °C substrate temperature. Then, on the AlN:Be films, Pt (10 nm)/Pd (10 nm)/Au (100 nm) ohmic contacts were created in the van der Pauw config. via Electron Beam Evaporation. While on the GaN:Ge layers, Ti/Al/Ti/Au (30/100/30/500 nm) contacts were fabricated using lithography and liftoff. The contacts annealing was performed under pure N_2 for 1

min at 800 ºC resulting in highly linear contacts with a current conduction increase of around 5 to 6 orders of magnitude.

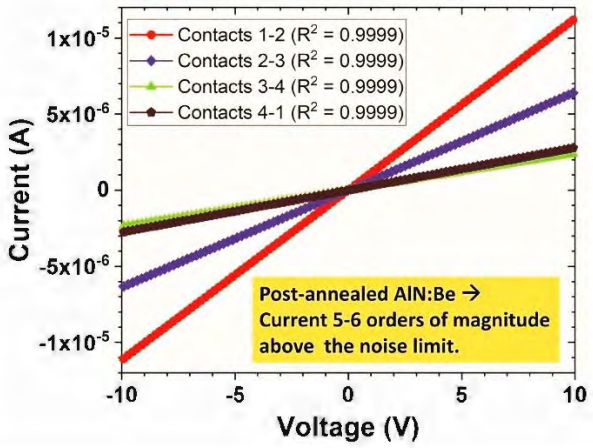

Figure 3.12: I-V behavior of the contacts Pt/Pd/Au on post-annealed AlN:Be layer [14]

Hot probe analysis showed p-type conductivity for the Be-doped AlN layers fabricated at 600 and 700 °C. Hall measurements indicated that with hole concentrations ranging from 2.3×10^{15}–7.6×10^{17} cm^{-3}, the Be doped AlN films produced at 600 °C with the concentration of dopants = 5×10^{16}–7×10^{18} cm^{-3} provide precise outcomes with ≈5% extracted activation efficiency of Be. At 700 °C, the Be-doped AlN films with doping concentration from 7×10^{18}–2×10^{20} cm^{-3} also showed accurate Hall data with increased doping efficiencies of ≈12% with up to 3.1×10^{18} cm^{-3} hole concentrations. While the increased Be doping in the range of 4×10^{19}–2×10^{20} cm^{-3} resulted in massive compensation causing a reduction in hole concentration and effective activation energy. A relatively low activation energy of around 37 meV was attained in the AlN:Be film for the Be that is not compensated. Also, the Hall effect analysis indicated the Be-doped AlN layers have a contact resistance in MΩ. A p-AlN:Be/i-GaN:Be/n-GaN:Ge (100/200/500 nm) diode structure was grown via MME to further validate the p-type behavior of the Be doped AlN layers. The PIN diode's current-voltage characteristics revealed a low reverse and high forward current sweep, indicating rectification of ≈7 orders of magnitude and moderate light emission from defects confirming AlN:Be films' p-type nature.

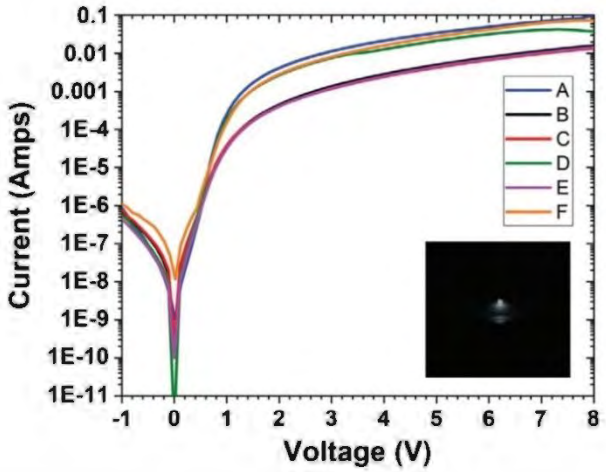

Figure 3.13: Semi-log current-voltage curves of the p-AlN:Be/i-GaN:Be/n-GaN:Ge diode. The pin diode's light emission may be seen in the inset [14]

Pramod Reddy et al. [94] examined the creation of the Schottky barrier between AlN in the c- and m-plane with metals having various work functions. The valence band maximum (VBM) was measured concerning the Fermi level at the junction to determine the height of the Schottky barrier while VBM was obtained using XPS data. Metallization was performed using e-beam evaporation with 10^{-8} Torr pressure at the base. The deposited films were introduced into the XPS chamber in a vacuum environment at 10^{-9} Torr. The InterFace-Induced Gap States (IFIGS) were used to perform the modeling experimentation of the barrier height behavior as the Schottky-Mott model was unable to explain it. The surface state density was taken into account using a slope parameter (S_x), which also serves as a gauge for Fermi-level pinning. AFM results showed smooth surfaces with RMS roughness of less than 0.5nm across an area of 10 × 10 μm^2. All of the bulk AlN templates had insulative behaviors having resistivities greater than 10 TΩcm. The barrier heights at the charge neutrality level were calculated as ~2.7 eV on the c-plane and ~2.1 eV on the m-plane with a slope parameter of nearly 0.36 eV per Miedema unit which were conforming to the theoretical results. S_x very less than 0.86 indicated an interface/surface states-dominated response having substantial Fermi level pinning. Among the metals examined, gold offered the highest barriers while titanium and zirconium offered the lowest. It was repeatedly discovered that elevated CNL caused the barrier heights to generally drop from polar metal surfaces to non-polar ones. These findings support the theory that charged IFIGS would balance out the charge from spontaneous polarization.

The figure below compares the heights of the barriers for various metals on the c-plane to those on the m-plane.

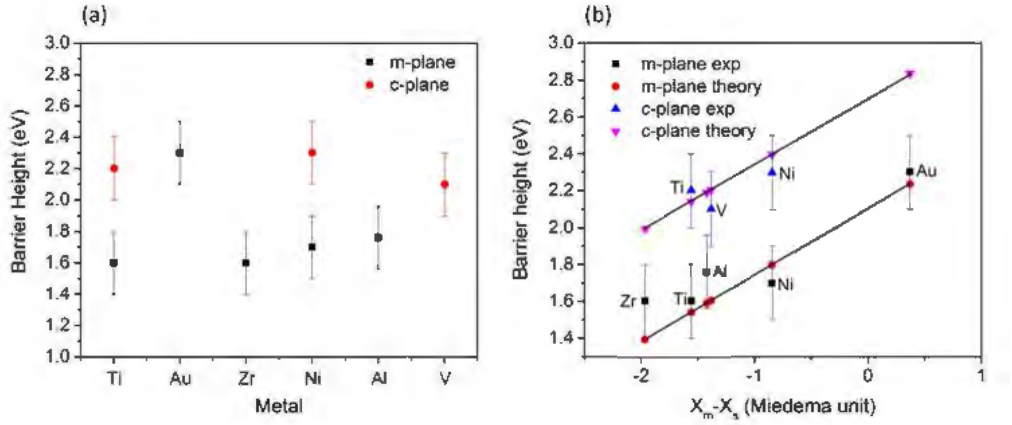

Figure 3.14: Comparison between heights of the barriers for various metals on c- and m-plane AlN [94]

Anatoly V. Sachenko et al. [95] explained the mechanisms of resistance creation for ohmic contacts on n-GaN and n-AlN films having substantial dislocation densities of structural deformities. The ~30 μm thick n-GaN layers (electron concentration greater than 10^{18} cm^{-3}) were fabricated on an AlN layer grown on the sapphire substrate. The ~3.5 μm AlN layers having high resistivity were formed on a SiC wafer with high doping. The films' dislocation densities were measured by XRD to be ~10^9 cm^{-2}. Then, ohmic Pd/Ti/Pd/Au (30/50/70/100 nm) contacts were produced on n-AlN and n-GaN at 350°C temperature followed by RTA at 900 °C a temperature for 30 seconds. Auger electron spectroscopy was employed to examine the component concentration depth profiles in the contacts prior to and following annealing. The transmission line approach was used to obtain the contact resistivity (ρ_c) curves in the range of 100-380 K temperatures. Layered metallization structures were obtained prior to the annealing of the samples while these metallization structures were fused with the GaN and AlN after annealing. Figure 3.15 provides a comparison of contact resistivity as a function of temperature ($\rho_c(T)$) for annealed contacts to n-AlN and n-GaN. The $\rho_c(T)$ curves showed that $\rho_c(T)$ basically does not rely on the temperature when it is below 160 K. The contact resistivity decreases with increasing temperature at low temperatures; for n-GaN contacts, from 160 K to 200 K, and up to 250 K for n-AlN contacts. This exponential change can be referred to as the low-temperature conductivity disordering in metal shunts. ρ_c changes slightly as the temperature elevates to

375 K. The no and weak dependency in portion 3 and portion 1 respectively can be explained based on the current flowing between the dislocations when there is heavy doping in the vicinity of the contact, and hence, considerable degeneration. These outcomes result in a shift in the conductivity to the activation type. Moreover, the value of ρ_c for n-AlN is 3 orders of magnitude greater as compared to n-GaN due to the increased resistance in the AlN film.

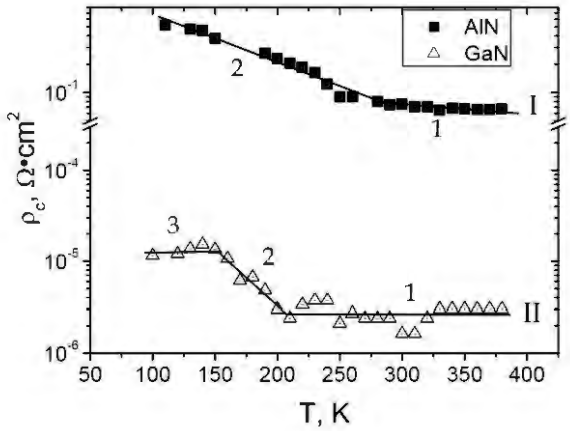

Figure 3.15: Comparison of ρc(T) curves for ohmic Pd/Ti/Pd/Au contacts to n-AlN and n-GaN [95]

M. Hirokia and K. Kumakura [96] fabricated improved ohmic contacts to Si doped AlN using a graded AlGaN contact layer. Metalorganic vapor phase epitaxy was used to grow the samples on semi-insulating SiC substrates. After the creation of an 800 nm undoped AlN layer on SiC substrate, a Si doped AlN of 500 nm thickness was deposited, succeeded by the formation of a graded AlGaN:Si film of 60-340 nm thickness. An $Al_{0.55}$ $Ga_{0.45}$ N:Si cap layer of 30 nm thickness was then grown on the top. The diagram of the layer structure is displayed below.

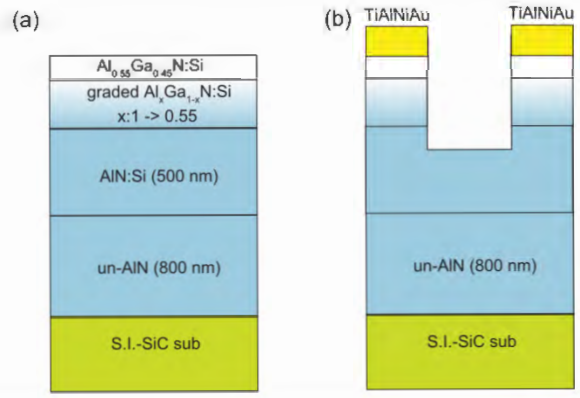

Figure 3.16: (a) Schematic layout of AlN:Si with a layer of graded AlGaN (b) a model structure for analyzing ohmic properties [96]

Metal contacts Ti/Al/Ni/Au were fabricated via e-beam evaporation proceeded by sample annealing at 850 °C. After that, ICP-RIE was used to eliminate the area between the ohmic contacts. The current-voltage curves of the AlN:Si with and without the layer of graded AlGaN are shown in Figure 3.17. Concerning the graded film of a 60 nm thickness sample, the non-linear current-voltage curve was obtained with a very small current. Similarly, non-ohmic characteristics were achieved for the sample with no graded AlGaN layer. While graded films of more than 150 nm thickness sample produced 3 orders of magnitude more I at 1 V. The Transfer line method was utilized to get the specific contact resistance (ρ_c) of the samples. It was found that as the graded AlGaN film thickness rises, its ρ_c decreases because of the graded AlGaN film polarization charge leading to a decrease in the 3-D negative charge density. A minimum ρ_c of 1.4×10^{-2} Ωcm^2 was achieved at 330 nm thick graded-AlGaN layer. To achieve the ohmic behavior of the contacts, the concentration of silicon doping (N_{Si}) must be greater than the density of polarization charge induced negative fixed charges (p_π). But due to self-compensation, the graded-AlGaN layer with high doping and 2.4×10^{19} cm^{-3} N_{Si}, turned semi-insulating. The findings suggested that the ohmic properties of the contacts can be enhanced by lowering p_π of the graded AlGaN layers.

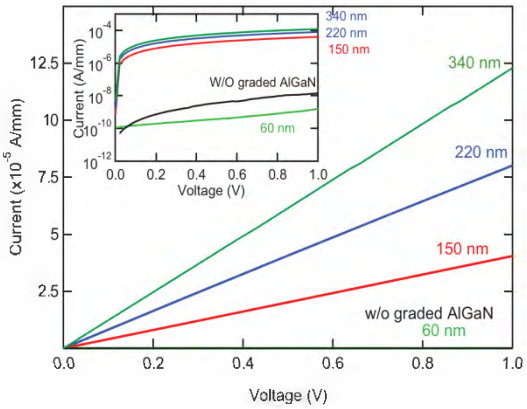

Figure 3.17: I-V curves of the AlN:Si with and without the graded-AlGaN film [96]

Toru Kinoshita et al. [97] demonstrated the formation of vertical SBDs on free-standing AlN wafers. 250 µm-thick AlN:Si films were deposited homoepitaxially on 5 mm diameter PVT (Physical Vapor Transport) - AlN (0001) substrates via hydride vapor phase epitaxy at 1450 °C. The n-type conductivity and donor ionization energy were obtained as 2.4 × 10^{14} cm^{-3} and 245 meV respectively at 300K by growing a Si-doped AlN film of 32 µm thickness to prevent the inaccuracy caused by thickness inhomogeneity. These results were comparable to that of silicon-doped AlN fabricated via MOCVD. Then, to fabricate the SBDs, ohmic Ti/Al/Ti/Au (20/100/20/50 nm) contacts were deposited onto the whole AlN:Si substrate polar surface. After that, sample annealing was performed at 1000 °C in nitrogen at barometric pressure. On the Si-doped AlN wafer's n-polar surface, a number of Schottky Ni/Au (20/50 nm) contacts with an area of 270 × 270 m^2 were fabricated. Using Ag paste on the side of the ohmic contact, the substrate was secured to a ceramic AlN carrier. The following figure illustrates the schematic of the fabricated vertical SBDs.

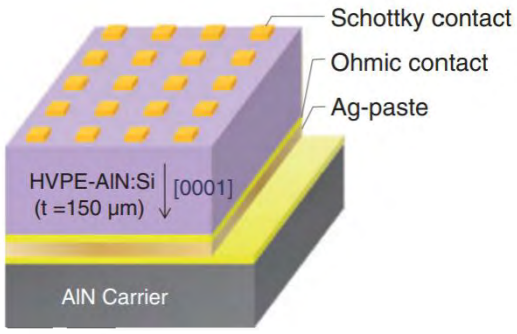

Figure 3.18: Layer structure diagram of the vertical Schottky BDs grown on AlN:Si substrates [97]

The X-ray ω-rocking curve analysis was conducted on the Si-doped AlN films showing high-crystalline quality similar to the PVT-AlN wafers as FWHM of the 0002 (symmetric) and 1011 (skew-symmetric) reflections that resembled those of PVT-AlN wafers. Figure 3.19 depicts the I-V behavior of the Schottky devices at 298 - 373 K temperature range. A V_{on} of roughly 2.2 V, a significant rectification ratio was seen. At 298 K, ϕ_B, n, and R_s were calculated to be approximately 1.1 eV, 7.93 and 3.5×10^6 Ω respectively. While increasing the temperature to 300K, series resistance and ideality factor reduced to 2.9×10^5 Ω and 5.4 respectively with an increase in ϕ_B to 1.7 eV. At AlN:Si and the Schottky interface, the presence of a damage layer is thought to be the reason for the difference in these values. The reverse I-V curves showed the reverse breakdown voltages in the 550–770 V range.

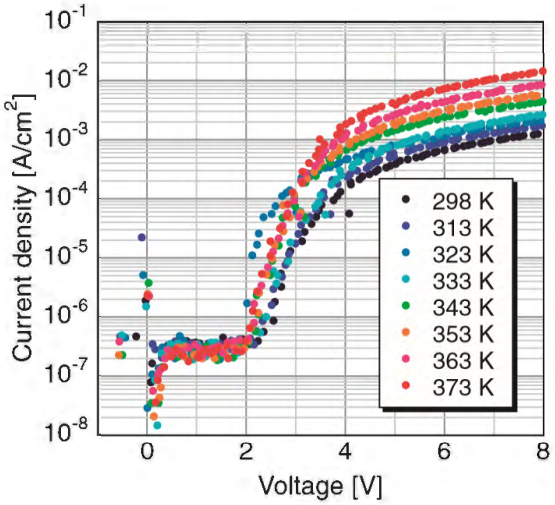

Figure 3.19: I-V behavior of the Schottky BDs fabricated on AlN:Si substrates [97]

CHAPTER 4

MODELING AND SIMULATION

The development of aluminum nitride (AlN) as a semiconductor material has opened new avenues for high-performance electronic and optoelectronic devices. The performance of AlN-based devices is critically dependent upon the quality and characteristics of the contacts to semiconductor devices. This chapter is devoted to the modeling and simulation of various metal contacts to AlN using Silvaco TCAD, a powerful tool for simulating semiconductor devices and processes. A comprehensive investigation of GaN and AlN-on-GaN Junction Barrier Schottky (JBS) diodes was also conducted, focused on inter-p^+ spacings of 0.5 to 2.5 μm to optimize their performance for high-temperature, high-frequency, and high-power applications.

4.1 Overview of Silvaco TCAD

Silvaco TCAD (Technology Computer Aided Design) is a robust software suite used for simulating and analyzing semiconductor devices and fabrication processes. It offers a platform for designing, simulating, and optimizing various electronic components. It provides engineers and researchers with powerful tools to analyze the physical behavior of devices at various stages of development, from fabrication to operational performance.

4.1.1 Key Components of Silvaco TCAD

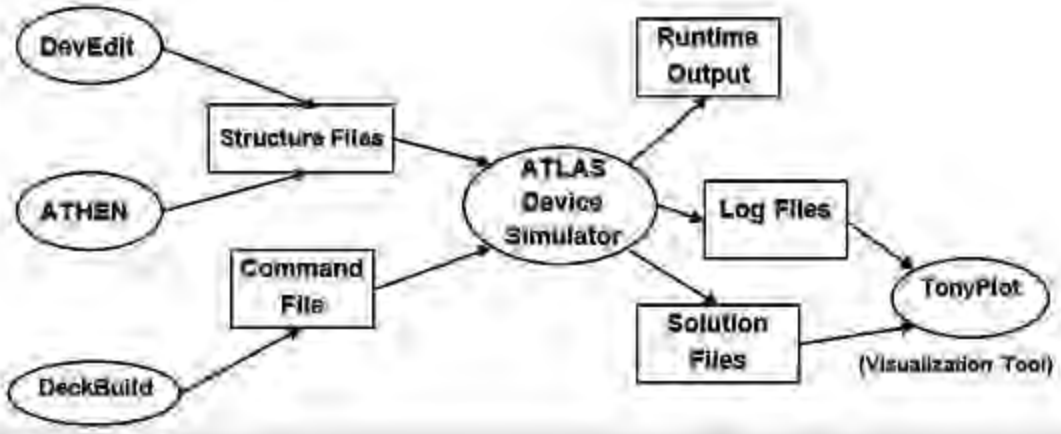

Figure 4.1: Silvaco TCAD Interaction Flowchart [98]

- ***DeckBuild:*** It is the main graphical user interface (GUI) environment within Silvaco TCAD that allows users to create, modify, execute, and analyze semiconductor device simulations. It serves as the central hub for various Silvaco tools.
- ***Athena:*** Focuses on process simulation. It can model the device and the semiconductor fabrication processes such as doping, oxidation, etching, deposition, and lithography.
- ***Atlas:*** Handles device simulation, analyzing the electrical behavior of the designed device structure. It can calculate current-voltage (I-V) characteristics, carrier distributions, and other relevant parameters.
- ***Devedit:*** A tool for designing and simulating semiconductor device structures. It is a powerful tool for creating and editing the device structure, defining regions, and setting up the simulation environment.
- ***TonyPlot:*** TonyPlot is a powerful tool designed for visualizing and interpreting simulation results produced by Silvaco TCAD. It provides a range of features for effective data visualization.

4.2 TCAD Modeling and Simulation of AlN Contacts

4.2.1 Device Design

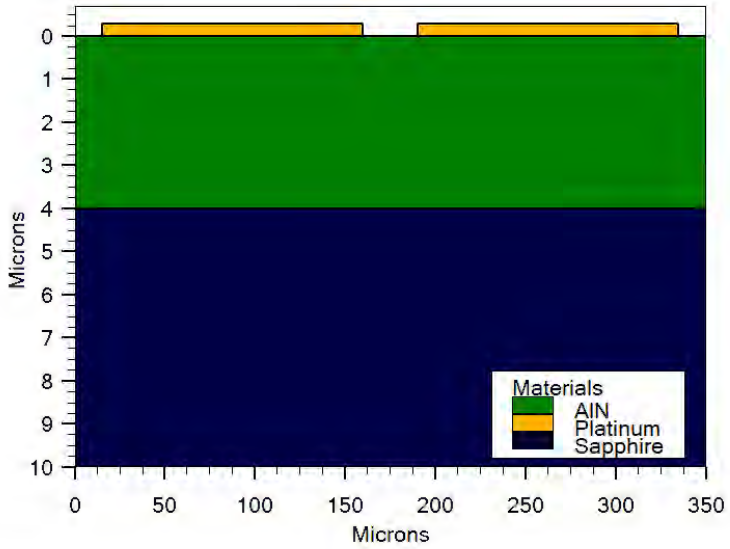

Figure 4.2: Structure of a Schottky diode featuring metal contacts on an AlN layer

Before conducting experimental studies to achieve optimized contacts to AlN, a modeling and simulation study with variation in the contact metal was performed using Silvaco TCAD software to investigate the impact of metals having different work functions. Figure 4.2 shows the simplest planar metallization structure adopted for this study for different metal contacts. The device structure and material properties were defined using the Devedit tool in Silvaco TCAD. The device consists of a 4 µm epitaxial AlN layer of uniform doping deposited on the Sapphire substrate. The doping concentrations were maintained at 5×10^{16} cm^{-3} for n-type and p-type AlN films. The Schottky anode and cathode of 0.1 µm thickness are at the top of the device. The metals used as Schottky contacts are listed in Table 4.1 along with their work functions.

Table 2.1: Work Functions of Contact Metals Utilized in the Simulations

Metal	**Work function, $e\Phi_m$ [eV]**
Platinum, Pt	5.65
Palladium, Pd	5.3
Gold, Au	5.2

Copper, Cu	4.70
Silver, Ag	4.7
Tin, Sn	4.42
Aluminum, Al	4.28
Indium, In	4.12

4.2.2 Simulation Setup

The Schottky diode was simulated using the Atlas module of the Silvaco TCAD. After defining the regions and electrodes, a structured mesh was applied throughout the device to achieve accurate simulation results. This mesh employed increased refinement in critical regions, particularly near the metal-AlN interface and Schottky contacts for accurate modeling of the contact behavior. AlN material properties are pre-defined in Silvaco TCAD including 2.43 eV electron affinity and 6.12 eV bandgap. The simulation employed a set of essential physical models to capture the behavior of the diodes accurately. The carrier statistics models employed were Fermi-Dirac (FERMI) and incomplete ionization (INCOMPLETE). Carrier recombination was modeled using the concentration-dependent (CONSRH), Auger, and optical (OPTR) band-band recombination models. To capture the necessary simulation data, output flags were set to record key parameters, including band structure, carrier mobility, and charge distributions. The Silvaco TCAD TonyPlot tool was used for visualizing and analyzing the results of the diode simulations.

4.2.3 Simulation Results

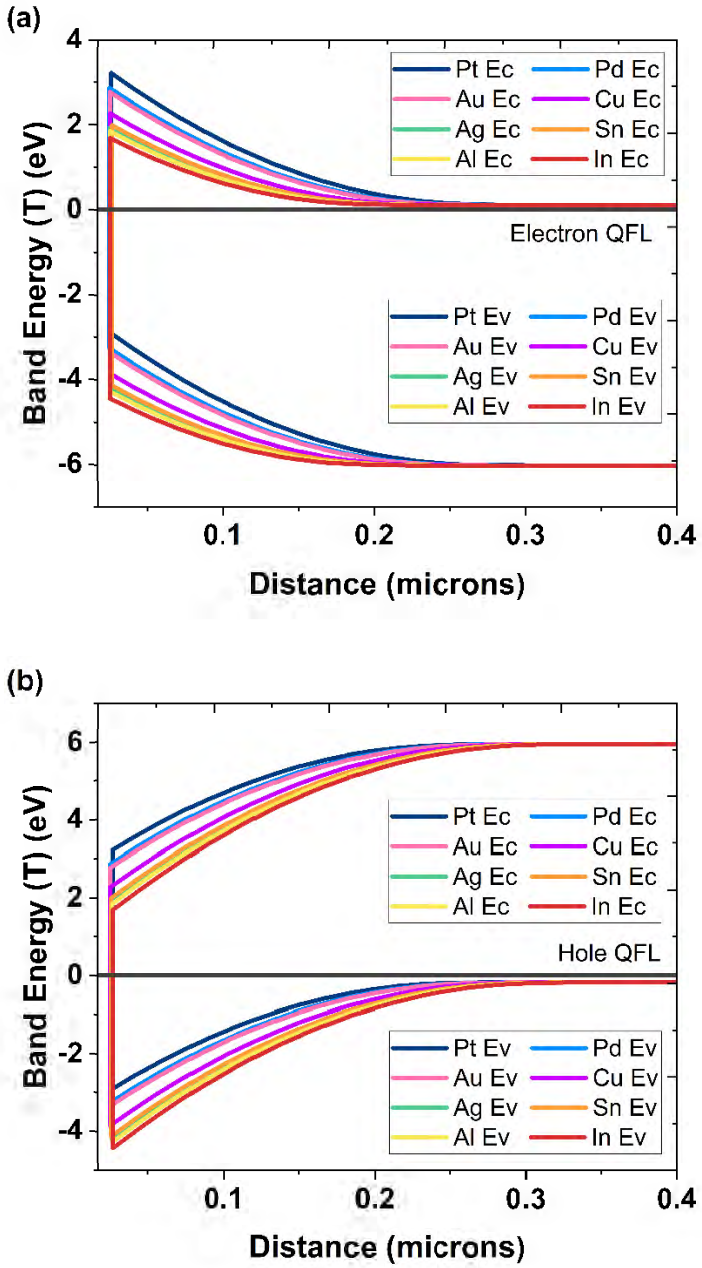

Figure 4.3: Silvaco TCAD energy band diagram simulations for various contact metals on (a) n-type, and (b) p-type AlN films

Figures 4.3 (a) and (b) show the simulated energy band diagrams for n-type and p-type AlN films, respectively with various metal contacts for comparison. The corresponding Schottky barrier heights (Φ_B) for various metals are given in Table 4.2. For p-type AlN, the lowest energy barrier of 2.9 eV is obtained with platinum contacts, as shown in Figure

4.3 (b). In the context of TCAD simulations, AlN is considered with a known electron affinity (χ) of 2.43 eV and given the wide bandgap of AlN, the semiconductor work function for p-type AlN would be very large, which would require the highest work function contact metals to have a low Schottky barrier. The work functions of all other metals are lower than Pt, leading to substantial Schottky barriers between the metal electrode and AlN film and large turn-on voltages. Therefore, the high work function requirements of metal contacts pose significant challenges in establishing ohmic contacts to p-type AlN.

The simulated SBH results for undoped AlN were identical to those for p-type AlN films. This highlights the requirement for employing metals with high work functions when establishing contact with undoped AlN films. The energy band diagram for n-type AlN films featuring distinct metal contacts is illustrated in Figure 4.3 (a). The corresponding potential barriers are listed in Table 4.2. For n-type AlN, metals of lower work function are required to obtain a small energy barrier between the metal electrode and the AlN film. Hence, the lowest value of Φ_B for n-type AlN is achieved in the case of indium metal contact.

For these simulations with single contact metals, the currents were negligible at 10V. Hence, diverse contact stack configurations are employed to tailor the energy barriers at the interface of contact metals and semiconductors, ultimately decreasing the contact resistance. In this simulation study, we investigated the cost-effective high work function metal stacks for undoped AlN films and contacts comprising Pt/Pd/Au stacks for p-type, and n-type AlN films. Based on these simulations, although Pt/Pd/Au combinations could prove advantageous for p-type and undoped materials, opting for low work function metals would improve n-type AlN film's performance.

Table 4.2: Simulated Schottky Barrier Heights for various contacts on n-type and p-type AlN films

Thin Film	Metal Contact	Schottky Barrier Height ($e\phi_{B0}$)
n-AlN	Pt	3.21
p-AlN	Pt	2.90
n-AlN	Pd	2.86

p-AlN	Pd	3.25
n-AlN	Au	2.76
p-AlN	Au	3.35
n-AlN	Cu	2.26
p-AlN	Cu	3.85
n-AlN	Ag	1.91
p-AlN	Ag	4.20
n-AlN	Sn	1.98
p-AlN	Sn	4.13
n-AlN	Al	1.84
p-AlN	Al	4.27
n-AlN	In	1.68
p-AlN	In	4.43

4.3 TCAD Modeling and Simulation of JBS Diodes

4.3.1 JBS Diode Design and Simulation Setup

The geometric layouts of the JBS diodes were created using Silvaco DevEdit, a device structure editor within the Silvaco TCAD suite. This tool also facilitated the assignment of materials and specification of doping concentrations for each device region.

The vertical planar diode structures, depicted in Figure 4.4**,** comprise p^+-GaN/n^--GaN/n^+-GaN regions in fully GaN-based diodes and p^+-AlN/n^--GaN/n^+-GaN in AlN-on-GaN diodes. Both devices feature a 1 µm unintentionally doped (UID) n^--GaN epitaxial drift layer with 1×10^{16} cm^{-3} doping concentration (N_D), placed atop a 5 µm n^+-GaN substrate with a uniform 1×10^{18} cm^{-3} N_D. JBS diode design requires careful selection of the drift region thickness and doping concentration to attain the desired balance between breakdown voltage and on-resistance. A thicker, lightly doped drift region enables higher breakdown voltage by facilitating significant depletion and improved electric field tolerance [41].

The JBS diode features a buried p^+-grid with a uniform 1×10^{18} cm^{-3} N_D. These p^+-GaN and p^+-AlN regions extend to a depth of 0.5 µm from the Schottky contact. The Schottky spacing between adjacent p^+ regions varies periodically, ranging from 0.5 µm at the lowest

to a high of 2.5 µm. The p^+ region width (w) and the distance between the inter- p^+ regions (s) are crucial design factors that affect the tradeoff between forward voltage drop and reverse leakage current in JBS diodes. By optimizing this trade-off, the diode can be tailored to exhibit predominantly PiN, JBS, or Schottky diode behavior. An ideal 0.1 µm thick molybdenum ohmic contact is placed on the n^+-GaN substrate at the bottom of the device for efficient current injection and at the top, a 0.1 µm thick molybdenum Schottky contact, characterized by a work function of 4.8 eV, was formed on the surface of the n^--GaN and p^+ regions. The device has an active area of 1×10^{-7} cm^2.

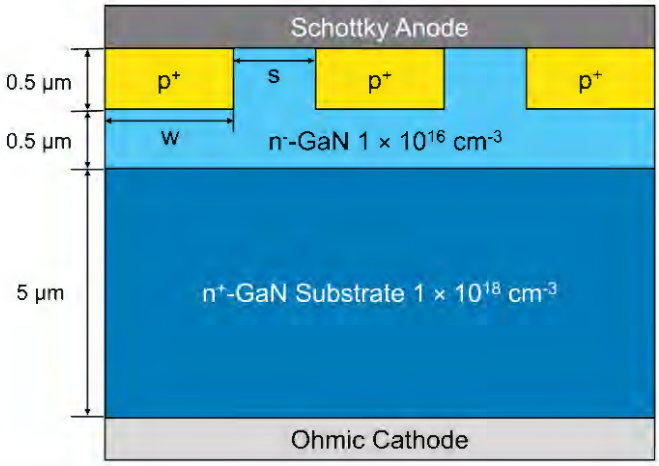

Figure 4.4: Diagram illustrating the simulated vertical diode device cross-section

Additionally, a structured mesh was applied throughout the device to achieve accurate simulation results. This mesh employed increased refinement in critical regions, particularly the active device area, the JBS grid, material junctions, and the top Schottky contact, ensuring precise calculations in areas with high electric field gradients and complex material interactions, which are crucial for capturing the electrical behavior of the diode. Silvaco ATLAS was used to perform a comparative electrical characterization analysis of the devices to assess the performance of fully GaN-based and AlN/GaN diodes. The simulations investigated the impact of varying the p^+-region width and the Schottky region spacing on the forward and reverse bias characteristics of the diodes. The simulation employed a set of essential physical models to capture the behavior of the diodes accurately. The influence of electric fields on carrier mobility was modeled using the Field Dependent Mobility (FLDMOB) model. The carrier statistics models employed were Fermi-Dirac (FERMI) and incomplete ionization (INCOMPLETE). Carrier recombination

was modeled using the concentration-dependent (CONSRH), Shockley-Read-Hall (SRH), and Auger (AUGER) recombination models. The impact ionization model employed was Selberherr's (IMPACT SELB), which is crucial to determining the device's breakdown process. The Silvaco TCAD TonyPlot tool was used for visualizing and analyzing the results of the diode simulations.

4.3.2 Simulation Results and Discussion

The contour plot in Figure 4.5 illustrates the net doping concentration per cm^3 for both fully GaN-based and AlN/GaN diodes. The doping concentrations are uniform throughout and consistent for all the diodes with the heavily doped n^+-GaN substrate and p^+ JBS regions exhibiting 10^{18} cm^{-3} of net doping concentration to ensure efficient carrier injection and contact formation. In contrast, a doping concentration of 10^{16} cm^{-3} characterizes the n^--drift region to facilitate the desired drift behavior for improved device performance.

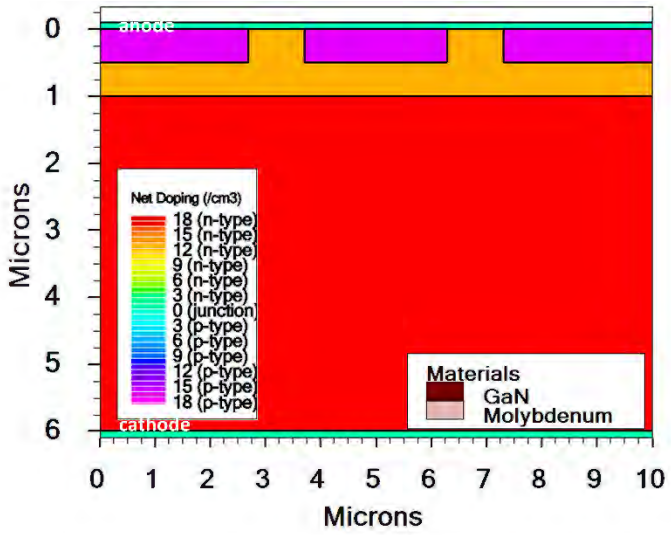

Figure 4.5: Contour plot showcasing the net doping concentration in cm^{-3} across fully GaN-based and AlN/GaN diodes

4.3.2.1 Forward Conduction Characteristics

The forward current conduction paths of fully GaN diodes with inter-p^+ region spacings of 0.5 µm, 1 µm, and 2 µm are illustrated by the current flowline plots in Figures 4.6 (a), 4.6 (b), and 3(c), respectively. At a narrower spacing of 0.5 µm, there is a significant contribution from both the carrier injection by the p^+ regions and thermionic emission at the Schottky contact regions evident from the relatively uniform distribution of current

flowlines across both regions. As the spacing is increased to 1.2 µm, the current flowing through the Schottky regions becomes more prominent as a result of expanded Schottky contact areas as the conduction channels, and at 2 µm, there is a clear trend where almost all the current flows through the Schottky contacts with negligible current contribution by the p^+ regions leading the JBS diode to operate closer to a full Schottky barrier diode.

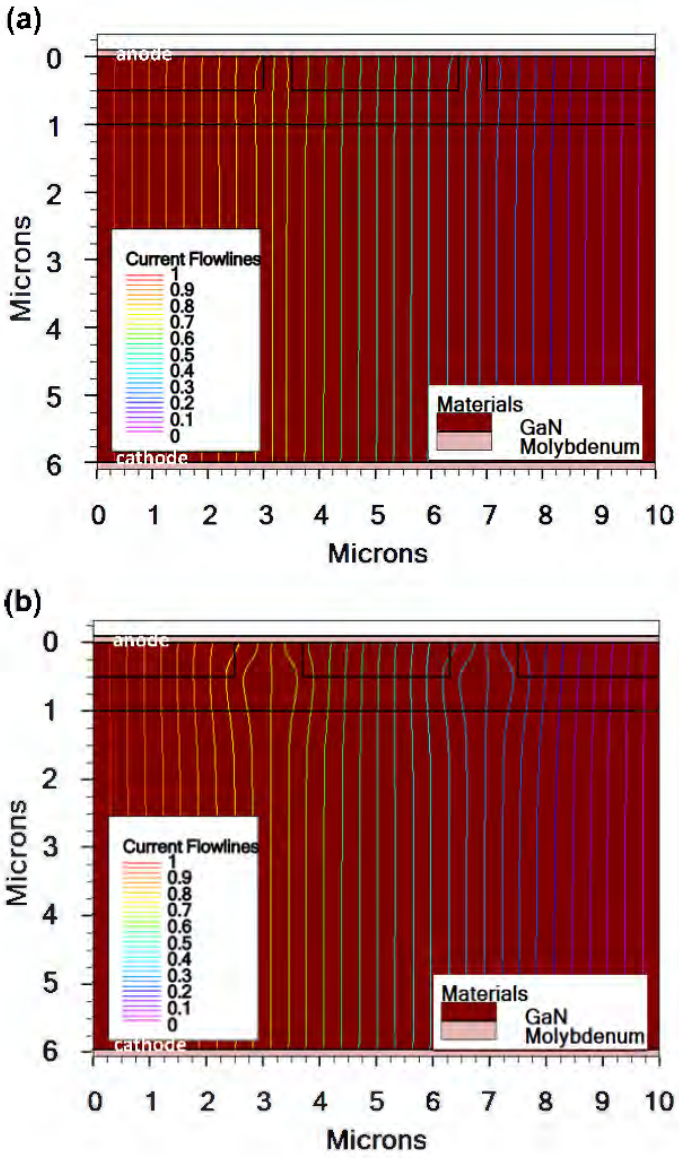

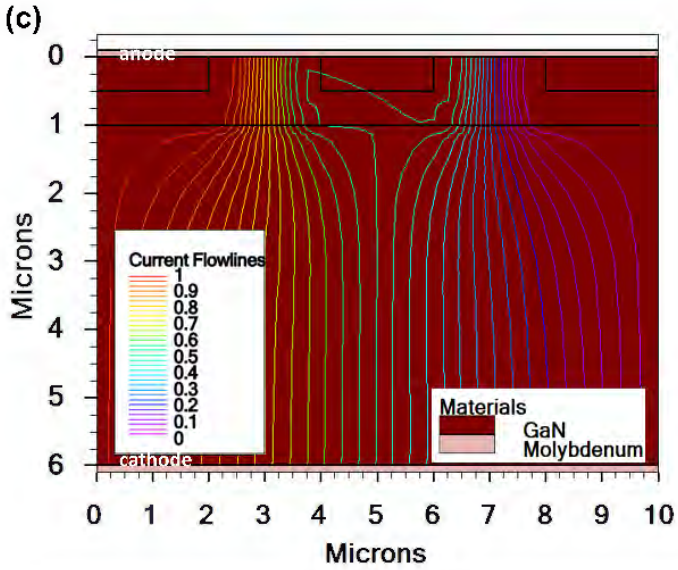

Figure 4.6: Current flowline plots of fully GaN-based diodes corresponding to inter-p+ spacings of (a) 0.5 µm (b) 1.2 µm and (c) 2 µm, indicating uniform distribution for the pin diode, mixed distribution for the JBS diode, and confinement of the current flowlines to the spacing layers for the SBD.

Figures 4.7 (a) and 4.7 (b) present the forward bias I-V behavior of fully GaN diodes while the I-V behaviors of AlN/GaN diodes are plotted in Figures 4.7 (c) and 4.7 (d), with varying relative p^+-region width (w) and Schottky spacing (s). The anode current versus anode voltage curves were plotted at spacings varying between 0.5 µm to 2.5 µm. The fully GaN diodes featuring narrower spacings within 0.5 µm to 0.7 µm range (Figure 4.7 (a)) exhibit PiN diode characteristics. A narrower spacing allows the p^+ regions to influence conduction significantly by facilitating the efficient transport of minority carriers to the n^--drift region and thereby contributing to the forward current. Similarly, the AlN/GaN diodes exhibit PiN behavior within 0.5 µm to 0.8 µm range , as depicted in Figure 4.7 (c).

As the spacing progressively extends from 0.8 µm for fully GaN diodes and 0.9 µm for AlN/GaN diodes to 2.5 µm, a transition in diode behavior is observed from JBS to Schottky characteristics. Within the JBS range, the diodes demonstrate turn-on characteristics similar to those of SBDs. This suggests that the dominant carrier transport mechanism in the JBS diode is Schottky emission, leading to a reduced turn-on voltage and increased forward current density. Unlike the Merged PiN-Schottky (MPS) diodes, the PN junctions

in JBS diodes do not contribute significantly to the forward conduction. When the forward voltage (V_F) exceeds the built-in voltage (V_{bi}) which is expressed in Equation 4.1.

$$V_{bi} = \frac{k_B T}{e} \cdot ln\left(\frac{N_A \cdot N_D}{{n_i}^2}\right) \tag{4.1}$$

where T is the temperature, e is the elementary charge, k_B is Boltzmann's constant, and N_D and N_A denote the donor and acceptor concentrations, respectively, a significant current increase is observed in Figures 4.7 (b) and 4.7 (d) at V_F values of around 3 V for fully GaN and 4 V for AlN/GaN-based diodes. This is attributed to both the p^+ and Schottky regions contributing to the overall current flow. The depletion region narrows at higher voltages, allowing for increased carrier injection through the p^+ regions alongside the thermionic emission in the Schottky regions. The diodes with wider spacings exceeding 1.3 µm for fully GaN and 1.4 µm for AlN/GaN diodes display characteristics similar to Schottky barrier diodes. In this regime, the wider spacings diminish the influence of the p^+ regions, leading to a reduction in SBH [99], and conduction primarily occurs through thermionic emission over the Schottky barrier. The observed reduction in SBH can be attributed to the depletion regions surrounding the p^+ regions that extend into the adjacent Schottky contact regions, effectively narrowing their width even further.

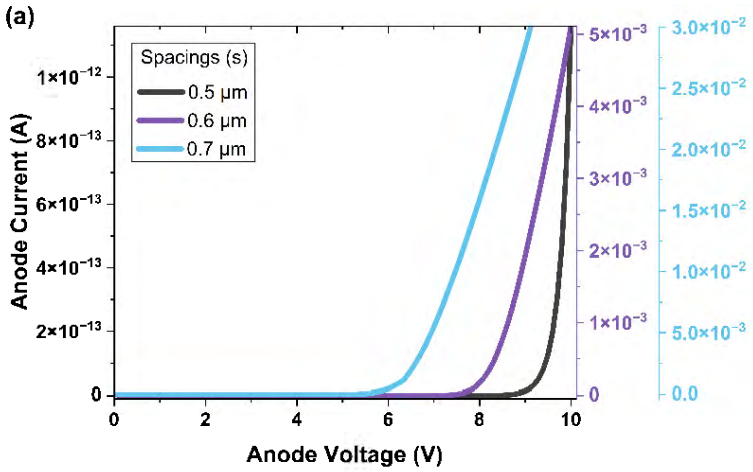

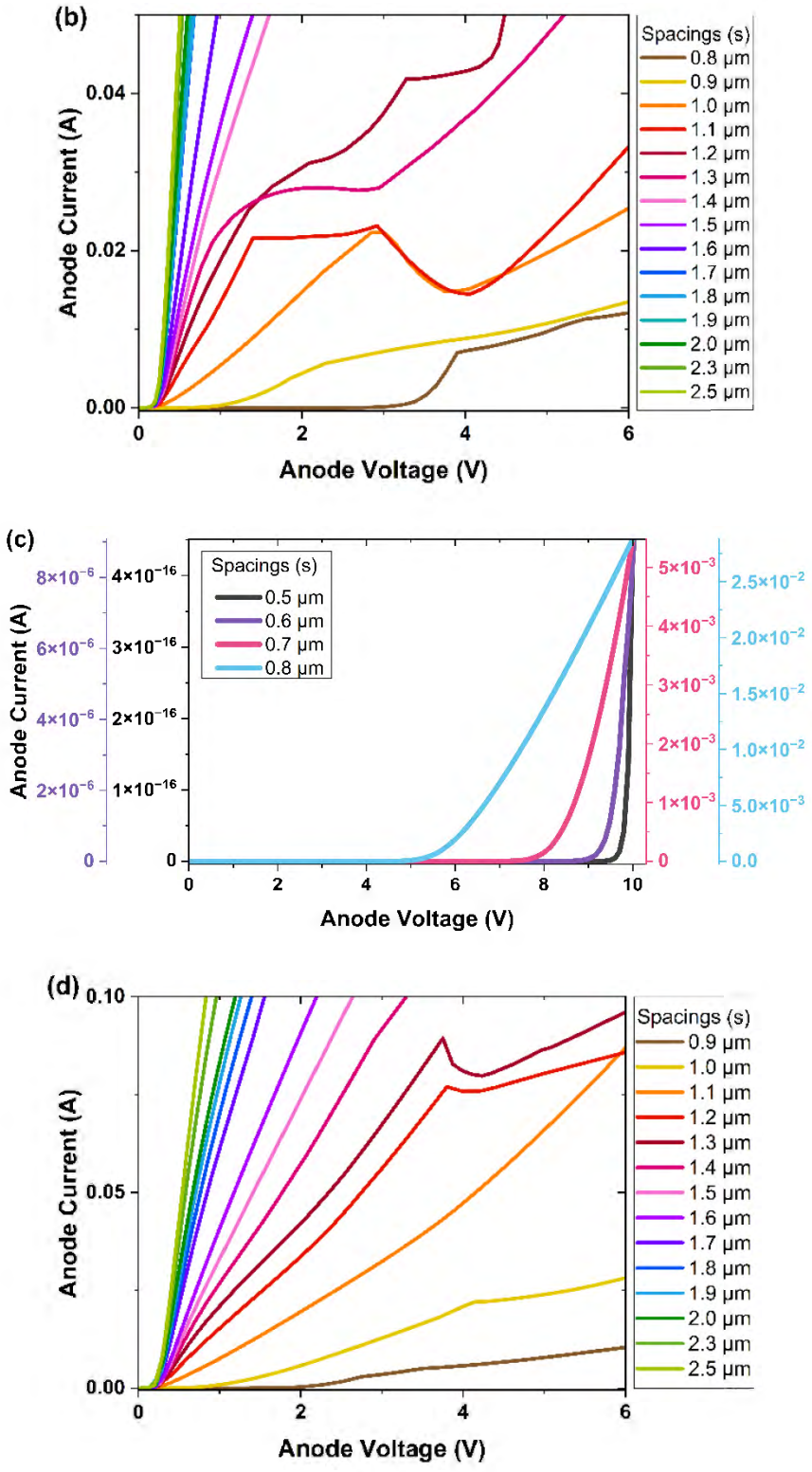

Figure 4.7: Simulated forward bias I-V characteristics of fully GaN-based diodes (a, b) and AlN/GaN diodes (c, d), with varying p^+ spacings

Key performance metrics for a JBS diode in forward operation include the specific on-resistance ($R_{on,sp}$) and the forward voltage drop (V_F). The JBS device design was optimized in Silvaco TCAD to achieve optimal values for these performance parameters. Figures 4.8 (a) and 4.8 (b) illustrate the impact of varying inter-p^+ spacing on the on-state performance of the fully GaN-based and AlN/GaN diodes. At narrower inter-p^+ region spacings, the diodes exhibit PiN characteristics with a high specific on-resistance and large forward voltage drop. The higher $R_{on,sp}$ at narrower Schottky spacings is mainly due to an increase in R_{ch} and R_{spread}. The existence of the p^+ grid reduces the available area of the drift region for current flow, leading to increased channel resistance. Additionally, the arrangement of the p^+ grid introduces non-uniform current distribution, resulting in spread resistance. Conversely, wider spacings reduce the influence of the p^+ regions and lead to improved forward conduction efficiency with a lower V_F and $R_{on,sp}$, approaching the behavior of Schottky barrier diodes.

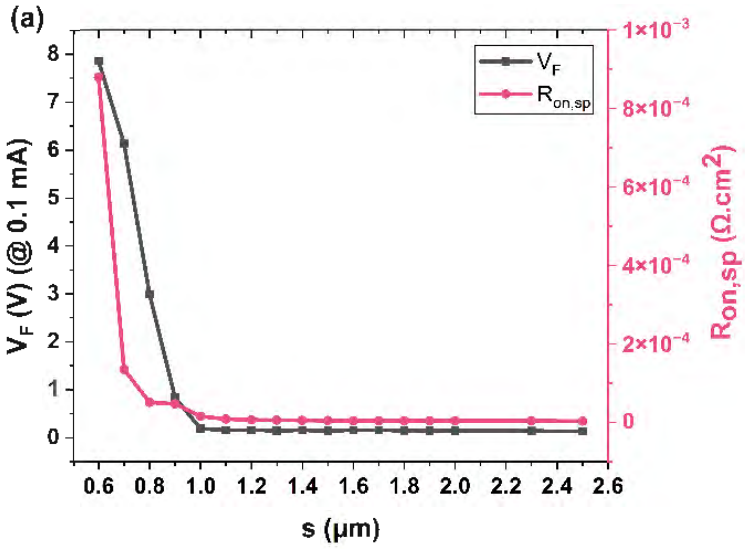

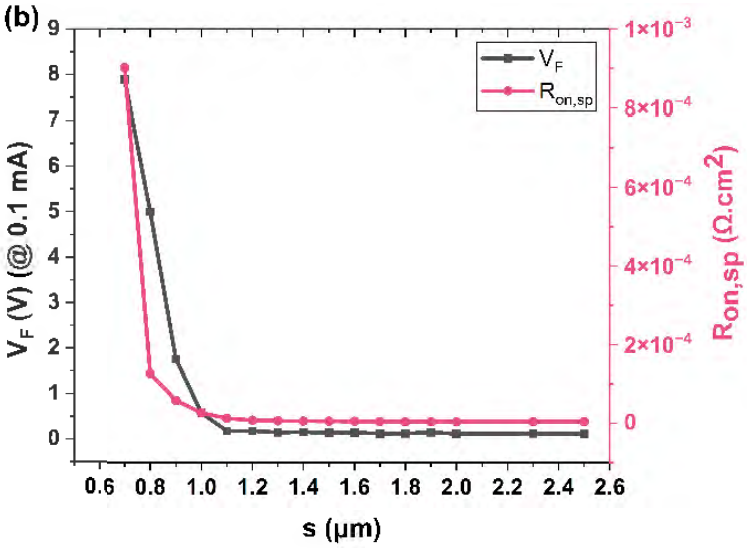

Figure 4.8: Forward diode parameters (forward voltage drop and specific on-resistance) at various inter-p+ region spacings determined from the I-V properties for (a) fully GaN-based and (b) AlN/GaN diodes

4.3.2.2 Reverse Breakdown Characteristics

The breakdown simulations were conducted to analyze the effect of the variations in JBS-grid configurations on shielding the Schottky regions in the devices from the high electric fields near avalanche breakdown [100] and to determine their breakdown characteristics. Figure 4.9 shows the simulated electric field distribution within the devices, for different inter-p^+ region spacings at 2.5 MV/cm of peak electric field (convergence issues encountered during the simulation process limited the breakdown analysis to diodes with specific inter-p^+ region spacings).

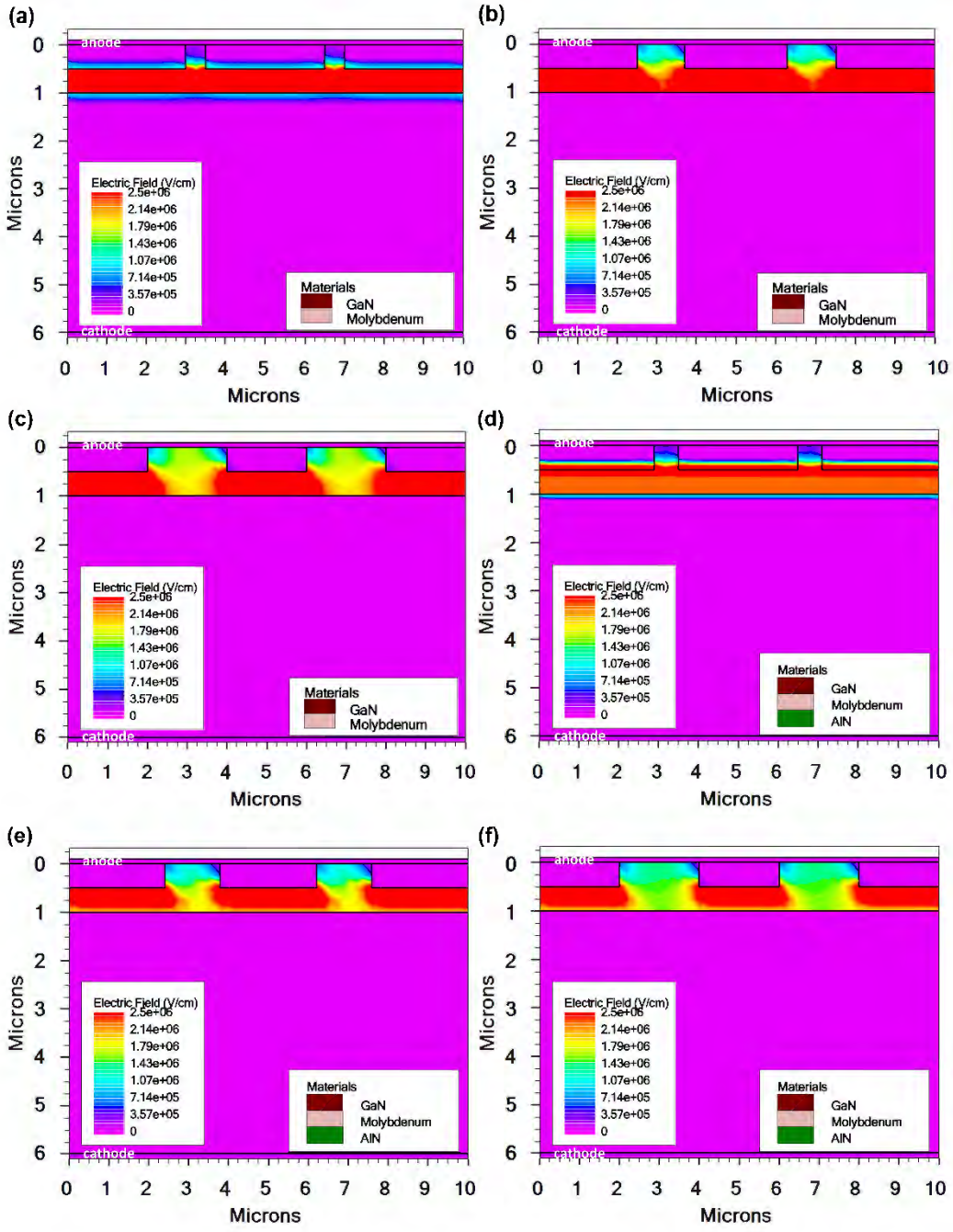

Figure 4.9: Simulated electric field distribution in fully GaN-based diodes with inter-p+ spacings (s) of (a) 0.5 µm, (b) 1.2 µm, and (c) 2 µm, alongside AlN/GaN diodes with s of (d) 0.6 µm, (e) 1.4 µm, and (f) 2 µm. With the increase in the spacing, the critical electrical field gets more confined to the p+ regions.

In cases of narrower spacings between the inter- p^+ regions (as shown in Figures 4.9 (a) and 4.9 (d)), the depletion region of the p^+n^- junction formed by the p^+ grid in a JBS diode

extends further under reverse bias which pinches off the drift region at the lower boundary of the Schottky channel. This depletion region acts as a barrier screening the Schottky interface from high electric fields. Since the acceptor (N_A) and donor (N_D) doping concentrations are comparable in these diodes, the lateral depletion region stretches into both the p^+ regions and the Schottky contact regions [45]. A low electric field at the Schottky interface effectively suppresses the field emission or tunneling current and keeps it lower than the thermionic current, minimizing the overall leakage current. The critical electric field migrates away from the Schottky interfaces and concentrates at the edges of the p^+ regions. Consequently, breakdown now takes place at the p^+ region periphery rather than the Schottky interfaces between them making the breakdown voltage a function of the p^+ grid of the JBS diode. Thus, JBS diodes exhibit an extended breakdown voltage in comparison to standard Schottky barrier diodes (SBDs), due to the pinching-off effect of the Schottky channel, which occurs before reaching the SBD breakdown voltage.[45], [46].

Expanding the inter-p^+ spacing up to 2.5 µm reduces the fusion effect between the adjacent depletion regions, thereby diminishing the shielding capability of the combined depletion regions in protecting the Schottky contact from the electric field. So, the electric field becomes concentrated at the junction between the Schottky contact and the n^--GaN drift region, initiating the premature breakdown of the device. This high electric field facilitates the electron tunneling through the Schottky barrier and contributes to a higher leakage current [41].

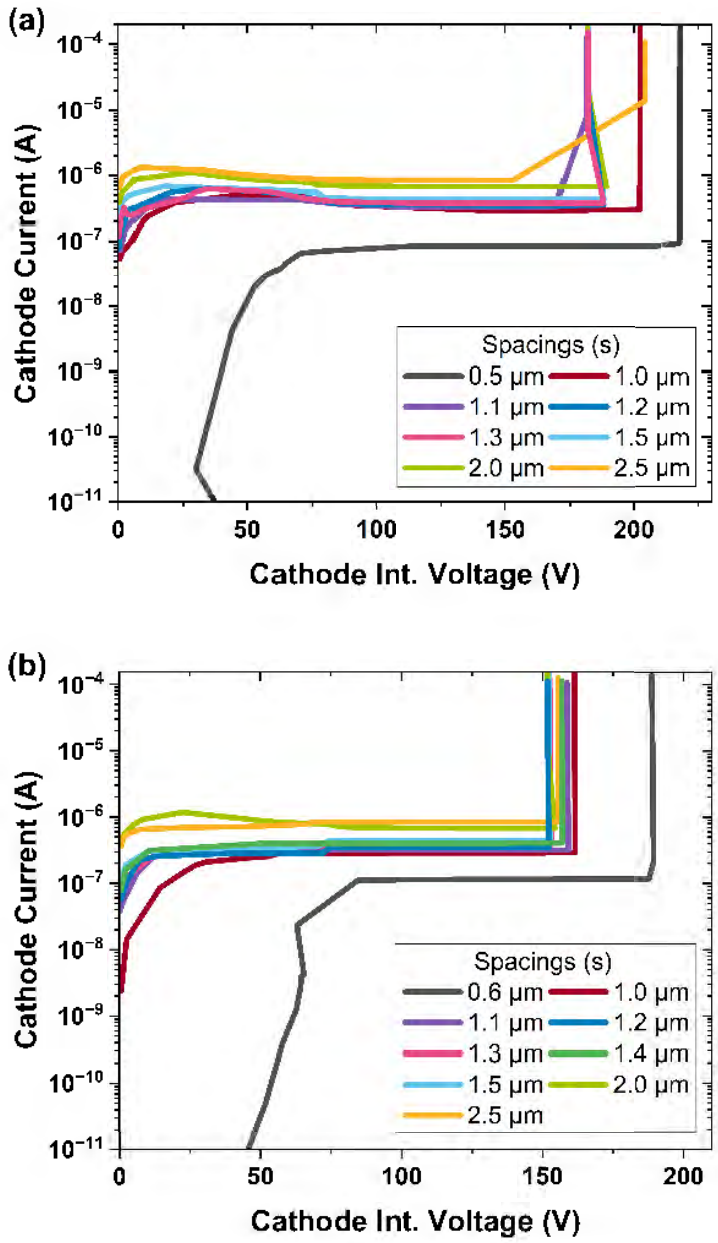

Figure 4.10: Simulated reverse breakdown characteristics of (a) fully GaN-based diodes and (b) AlN/GaN diodes, with varying inter-p+ spacing (s)

JBS diodes should exhibit minimal reverse leakage current in reverse bias conditions, ideally approaching the low levels observed in PiN diodes. Figures 4.10 (a) and 4.10 (b) present semi-log plots of cathode internal voltage vs. cathode current for fully GaN-based and AlN/GaN diodes, respectively, as a function of different JBS grid spacings. It can be observed that the diodes with wider p^+ regions exhibit a low reverse leakage current. As the Schottky spacing increases, the effectiveness to shield the Schottky contact against the

electric field mitigates, increasing the reverse leakage current. Furthermore, increasing the distance between the p^+ regions reduces the critical voltage, approaching the behavior of the SBDs. The lattice mismatch between GaN and AlN can introduce crystallographic defects and dislocations at their interface. These dislocations can deteriorate the reverse breakdown performance of AlN-on-GaN diodes compared to fully GaN diodes. Figures 4.11 (a) and 4.11 (b) illustrate the breakdown voltages at a reverse-biased current of 1 µA and leakage currents at 100 V for diodes with different inter-p^+ region spacings. The identified JBS ranges (1-1.3 µm for fully GaN and 1.1-1.4 µm for AlN/GaN) offer breakdown voltages that lie intermediate between those of PiN diodes (higher breakdown) and the Schottky diodes (lower breakdown). The smallest Schottky spacings provide the lowest leakage current of 0.0791 µA in fully GaN-based and 0.113 µA in AlN/GaN diodes and it increases with increasing spacing between the p^+ regions. For comparison, diodes with the 1 µm inter-p^+ spacing exhibit approximately twofold lower leakage current as compared to the diodes with the spacing of 2 µm. The simulated critical breakdown electric field values for the depleted n^--GaN drift layer at a depth of 0.5 µm from the Schottky contact at their corresponding breakdown voltage points are also plotted in the figures.

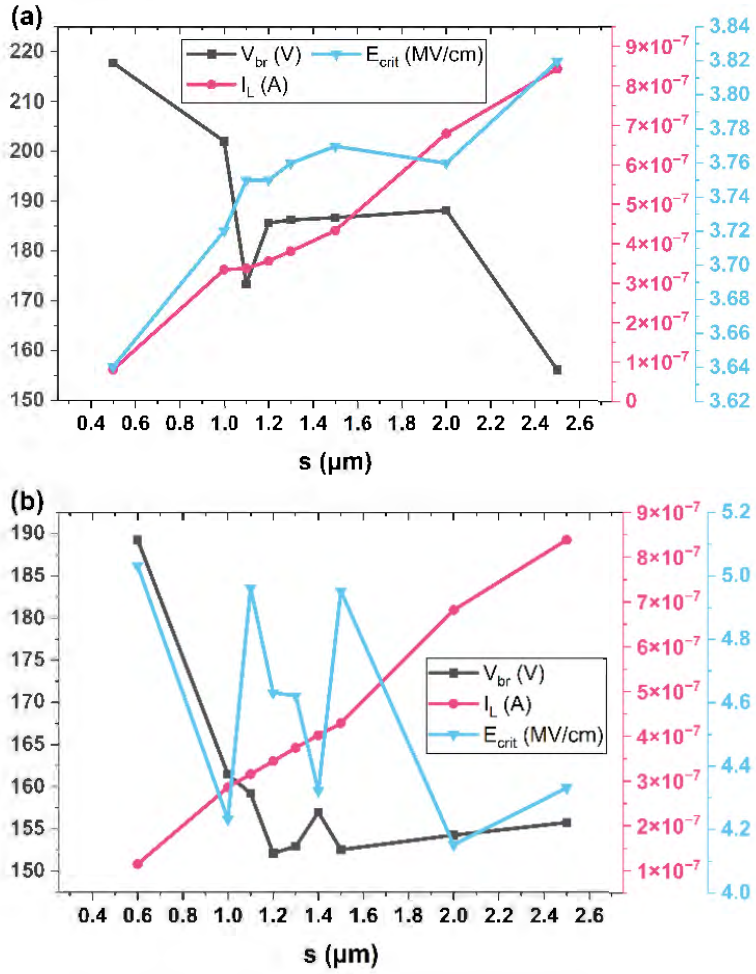

Figure 4.11: Reverse diode parameters (breakdown voltage, leakage current, and breakdown electric field) at various inter-p^+ region spacings determined from the I-V characteristics for (a) fully GaN-based and (b) AlN/GaN-based diodes

4.3.2.3 Baliga's Figure of Merit (BFOM)

Figure 4.12 presents a plot of Baliga's Figure-of-Merit (BFOM), calculated as $V_{br}^2/R_{on,sp}$, against inter- p^+ spacing for the forward JBS ranges of fully GaN and AlN/GaN JBS diodes to evaluate the trade-off between specific on-resistance and breakdown voltage for these diodes. The highest BFOM of 3.47 × 10^8 W/cm^2 for the fully GaN-based JBS diode is achieved at 1.2 μm inter-p^+ spacing indicating that this spacing provides the optimal balance between the diode's voltage-blocking capability and its conduction efficiency for the fully GaN-based device structure whereas 1.4 μm spacing provides the highest BFOM of 6.78 × 10^8 W/cm^2 for AlN/GaN diodes. As shown in Figure 4.12, at the optimal 1.2 μm inter-p^+ spacing for fully GaN-based diodes, key performance metrics include a $R_{on,\,sp}$ of

6.13×10^{-3} mΩ·cm^2, V_F of 0.157 V, V_{br} of 185.72 V, I_L of 0.356 µA and a critical E-field of 3.75 MV/cm. Similarly, the optimal AlN/GaN diode with an inter-p$^+$ spacing of 1.4 µm achieves a $R_{on, sp}$ of 5.14×10^{-3} mΩ·cm^2, V_F of 0.164 V, V_{br} of 156.98 V, I_L of 0.401 µA and a critical E-field of 4.32 MV/cm.

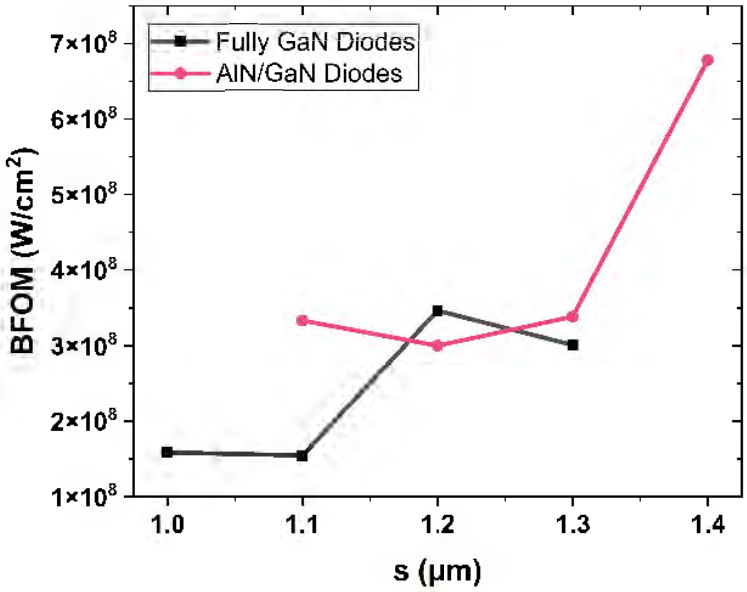

Figure 4.12: Baliga's Figure of Merit (BFOM) as a function of inter-p+ spacing (s) for fully GaN-based diodes (black squares) and AlN/GaN-based JBS diodes (pink circles)

CHAPTER 5

FABRICATION PROCESS

The fabrication of electrical contacts on AlN films is a critical step in optimizing the efficiency of semiconductor devices. This section provides a comprehensive overview of the materials, methods, and techniques utilized in the fabrication process of undoped, p-type, and n-type doped AlN films, as well as the electrical contacts to these films. Emphasis is placed on the precise conditions required for each step to achieve high-quality, reliable contacts that minimize parasitic losses and enhance device performance.

5.1 Material Selection

5.1.1 Substrate Material

Silicon and Sapphire substrates were selected as the growth platforms for epitaxially depositing AlN thin films. Silicon offers cost-effectiveness, widespread availability, and compatibility with existing semiconductor technology. Although the disparity in lattice structure between AlN and silicon introduces certain difficulties, the promise of seamless integration with silicon-based devices, coupled with the material's exceptional thermal properties, underscores its suitability for this research. Sapphire, on the other hand, provides a closer lattice match to AlN, promoting improved crystalline quality.

5.1.2 Dopants

- Silicon was chosen to achieve n-type conductivity in aluminum nitride due to its low ionization potential, which facilitates the generation of free carriers, and its high solubility in aluminum nitride. Additionally, the close atomic radius alignment between silicon and aluminum promotes effectively incorporating silicon dopants into the AlN lattice [101], [102].

- P-type conductivity in AlN was achieved using beryllium (Be), owing to its favorable properties including low ionization energy and high solubility in AlN.

5.1.3 Contact Metals

- Fabricating ohmic contacts on AlN, particularly p-type AlN, necessitates using metals with the highest work functions because of the semiconductor's low electron affinity and wide bandgap. To achieve this, platinum (Pt, 5.65 eV), palladium (Pd, 5.12 eV), and gold (Au, 5.1 eV) – metals known for their highest work functions – were selected as potential contact metals for both p- and n-type AlN films [103].
- To form contacts on undoped AlN films, cost-effective metals exhibiting high work functions were chosen. Silver (Ag), possessing a 4.70 eV work function, was selected as the base contact metal due to its favorable electrical and thermal properties and excellent adhesion to AlN. To investigate the impact of different combinations of metals on contact characteristics, aluminum (Al, 4.28 eV), copper (Cu, 4.65 eV), tin (Sn, 4.42 eV), and zinc (Zn, 4.31 eV) were incorporated to form various contact stacks [103].

5.2 Substrate Preparation

The 1 × 1 cm^2 silicon substrates utilized in this research were diced from a 2-inch, 350 μm thick, p-type silicon wafer. Before the deposition of AlN films, the substrates must be thoroughly prepared to ensure surface cleanliness and proper adhesion of subsequent layers. The following steps outline the substrate preparation process:

5.2.1 Solvent Clean

A two-solvent procedure was employed: the silicon dies were first immersed in acetone at 80 °C for 20 minutes to remove organic contaminants, followed by a 3-minute dip in methanol to eliminate residual acetone. To eliminate solvent residues, samples were thoroughly rinsed with deionized water (DI) and blow-dried with N_2 gas.

5.2.2 RCA Clean

The solution is composed of ammonium hydroxide and hydrogen peroxide (AHP). The samples were placed in the AHP solution ($4NH_4OH:1H_2O_2$) for 5 minutes. The AHP

solution exhibits exceptional efficacy in removing organic residues from silicon wafers. During this cleaning step, the silicon surface undergoes oxidation, leading to the creation of a thin oxide layer.

5.2.3 HF Dip:

A 20% hydrofluoric acid solution (1HF:4H_2O) was used to etch the substrates for 1 minute to remove native oxides (SiO_2) and improve surface roughness. Substrates were finally rinsed with water and dried using nitrogen gas to prevent contamination before film deposition.

5.3 Fabrication of Thin Films

5.3.1 Magnetron Sputtering (MS)

It is a common technique for thin film deposition and a type of physical vapor deposition. This study utilized magnetron sputtering to deposit AlN by striking the target metal with high-energy particles, resulting in the ejection and subsequent condensation of AlN atoms onto the substrate. Magnetron sputtering is favored because it offers the capability to deposit high-quality and uniform coatings with excellent adhesion, ease of use, low cost, and controlled thickness [22].

5.3.1.1 Working Principle

The core principle of magnetron sputtering involves generating plasma in a vacuum chamber. When a voltage is introduced between the target and anode, a field is created that drives electrons toward the target, ionizing the inert gas, typically argon, and generating a plasma. The combined effect of magnetic and electric fields within the sputtering chamber forces electrons to move in a spiral trajectory near the target's surface. This extended electron trajectory increases the likelihood of ionizing argon gas atoms. The positively charged ions generated in the plasma are drawn toward the negatively charged target, leading to the ejection of atoms from the target's surface. These ejected atoms move through the chamber and settle on the substrate, creating a thin layer.

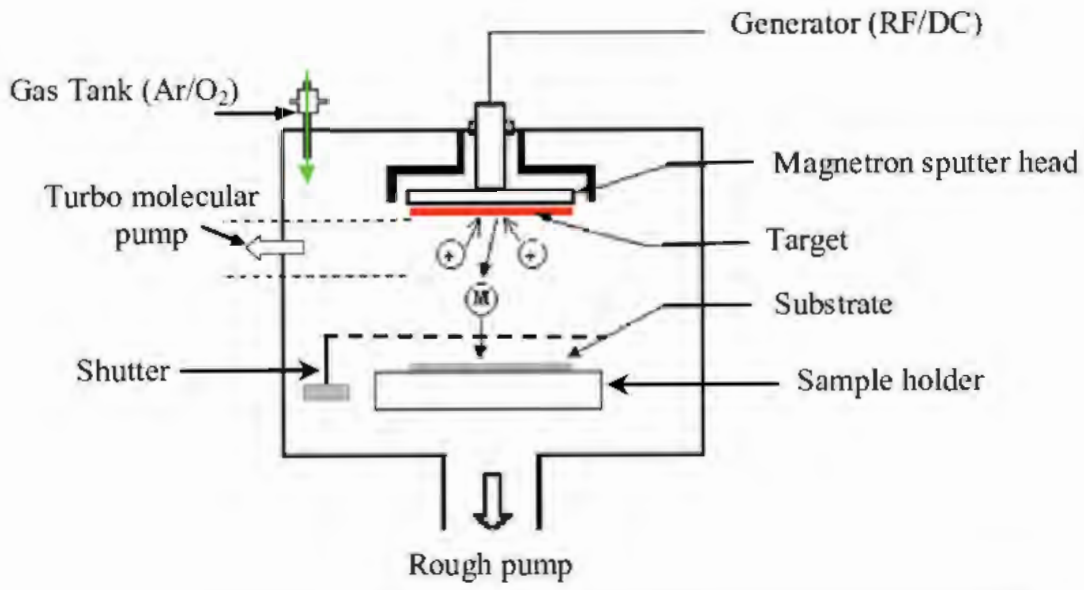

Figure 5.1: Schematic layout of the magnetron sputtering system [104]

5.3.1.2 Types of Magnetron Sputtering

Magnetron sputtering is categorized into two main types:

- ***DC Magnetron Sputtering***

It uses a continuous direct current to generate the plasma. This method is suitable for conducting materials because the constant voltage can efficiently ionize the gas and sputter the target material. The benefits of DC magnetron sputtering include its simplicity, cost-effectiveness, and high deposition rates. However, it is not suitable for insulating materials as they can accumulate charge, leading to arcing and instability in the plasma.

- ***RF Magnetron Sputtering***

RF magnetron sputtering, on the other hand, utilizes an alternating current at radio frequencies (typically 13.56 MHz) to generate the plasma. This alternating current prevents charge buildup, making RF magnetron sputtering suitable for both conducting and insulating materials. While RF sputtering is more complex and can have lower deposition rates compared to DC sputtering, its versatility in handling a wide range of materials makes it a valuable technique for various applications.

5.3.1.3 Magnetron Sputtering Process Parameters

Undoped AlN thin film deposition was performed using a dual-head, high-vacuum 2-inch magnetron plasma sputtering coater system from Zhengzhou CY Scientific Instrument Co., Ltd., utilizing the RF sputtering mode. An aluminum target at the sputter head was attached for the sputtering process. AlN thin layers were fabricated on sixteen silicon-100 substrates held at a temperature of 300 °C. Argon served as the sputtering gas, while molecular nitrogen served as the reactive component. Argon gas flow was held steady at 25 sccm and the nitrogen gas flow was steadily increased from 10 to 25 sccm in increments of 5 sccm. The working pressure varied between 0.2-0.63 Pa, with magnetron power set to 200 and 250 W. A film density of 3.26 g/cm³ and a z-ratio of 1 was set for AlN. Growth time was carefully monitored for each set of deposition parameters to achieve a final AlN film thickness of 100 nm. Table 5.1 summarizes the process parameters employed in different magnetron sputtering runs.

Table 5.1: Magnetron Sputtering Process Parameters

MS. Run #	Samples #	MS. Process Parameters		
		Substrate Temp. [°C]	Power [W]	N_2-Flow [sccm]
1	1, 2	300	200	10
2	3, 4	300	200	15
3	5, 6	300	200	20
4	7, 8	300	200	25
5	9, 10	300	250	10
6	11, 12	300	250	15
7	13, 14	300	250	20
8	15, 16	300	250	25

5.3.2 Metal-Modulated Epitaxy (MME)

MME is an advanced variant of molecular beam epitaxy (MBE) that is increasingly utilized for the growth of high-quality III-nitride semiconductors. This technique is particularly advantageous in achieving precise control over film stoichiometry, surface morphology,

and defect density by controlling the III/V ratio, temperature of the substrate, and excess-metal dose for each shutter cycle growth parameters.

In the MME process, the growth of AlN is modulated by alternating the flux of metal (aluminum) and nitrogen precursors during the epitaxy. In Plasma-Assisted Molecular Beam Epitaxy (PAMBE), a plasma source is used to generate reactive nitrogen species, which are then combined with the aluminum atoms to form the AlN film. The key feature of MME is the temporal separation of metal and nitrogen fluxes, allowing the surface to be saturated with metal atoms before exposure to nitrogen plasma.

In this work, a radio frequency PAMBE system from Riber was used to grow the doped AlN samples through MME on 4 μm AlN grown via hydride vapor phase epitaxy (HVPE) on sapphire substrates. A 300 nm undoped AlN buffer layer was placed on top of the HVPE-AlN templates from MSE Supplies after they had been carefully cleaned and outgassed. For the p-type samples, this buffer layer was deposited at 800 °C substrate temperature, serving the purpose of encapsulating surface contaminants. The 100 nm layer of AlN was deposited on the HVPE- AlN using optimal MME deposition conditions. The temperature of the substrate was maintained at 600 °C, the III/V ratio was set to 1.3 and the shutter sequence was controlled with open/close times of 5 seconds/10 seconds. For the n-type samples, AlN:Si films of 500 nm thickness were epitaxially deposited via MME on HVPE AlN on sapphire templates. The substrate temperature was maintained at 1100 °C throughout the growth procedure, with a III/V ratio maintained at 1.3. The MME process employed a metal-nitrogen flux modulation cycle with a shutter ratio of 21 seconds /11 seconds. Silicon and beryllium were provided by effusion cells. The AlN layers were deposited at ~2×10^{-5} Torr at ~2×10^{-5} Torr N_2 pressure, with MBE chamber base pressure kept at around 5×10^{-11} Torr. A deposition rate of 1.40 μm/h was maintained for the AlN:Si films, while a deposition rate of 700 nm/h rate was maintained for the AlN:Be films.

5.4 Fabrication of Electrical Contacts

5.4.1 Contact Patterning

To define the electrical contacts, a polymer mask was employed for patterning before the deposition process. The mask design consisted of two rectangular contact areas centered

on the AlN region on the 1 × 1 cm^2 sample. The larger contact area measured 0.06 cm^2, while the smaller contact area was 0.018 cm^2.

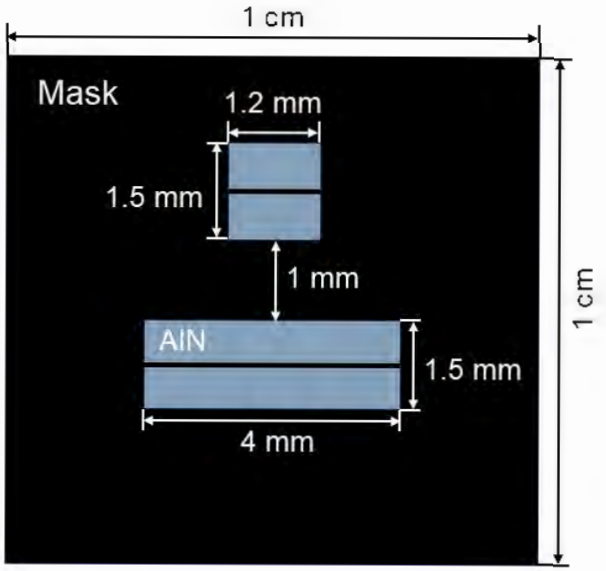

Figure 5.2: Schematic representation of the mask used for contact patterning

5.4.2 Oxide Removal

As explained earlier, oxygen readily reacts with AlN to form an aluminum oxide or aluminum oxynitride layer. Additionally, it can form silicon dioxide or silicon nitride on the AlN surface which can significantly degrade the performance of metal contacts. To clean the AlN thin film surface of its native oxide layer, a mechanical polishing process was employed on eight samples just before metallization. This method involved using an abrasive to gently remove the oxide layer without damaging the underlying AlN layer.

5.4.3 Physical Vapor Deposition (PVD)

PVD is a widely used method for depositing thin films to produce electronic components that operate on the principle of thermal evaporation. In this method, the source substance which can be in various forms is placed in a crucible or boat made of a high-melting-point material. This crucible is then heated, either by passing an electric current through it or by using an external heat source, until the source material reaches its evaporation temperature. The heat energy provided causes the atoms or molecules of the source material to break free from the surface and enter the gaseous state. The vaporized source material then travels through the vacuum or low-pressure chamber and condenses onto the cooler surface of the

substrate, forming a thin layer. The thickness of the evaporated material film is monitored using a quartz crystal. This process allows high purity, uniformity (by controlling substrate rotation speed), and versatility in material selection. Process variables like growth rate, substrate temperature, and pressure can be finely tuned for desired film properties.

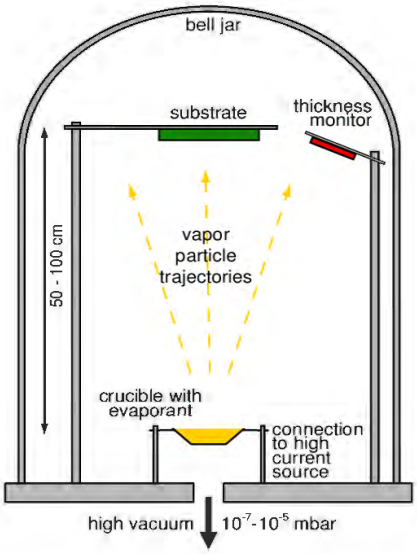

Figure 5.3: Illustration of the PVD system schematic [105]

5.4.3.1 PVD Process Parameters

Contact metal deposition on the undoped AlN samples was performed using the Nano Master NTE-3000 Thermal Evaporator, an atomistic scale physical vapor deposition system. The source metals were evaporated using an S8D-0.010W Tungsten boat under a nitrogen pressure of 15 psi and compressed dry air (CDA) pressure of 80 psi. A chamber pressure of approximately 1.38×10^{-1} torr was achieved during deposition. To optimize process efficiency, multiple samples were loaded in the chamber simultaneously for each run, resulting in a total of five deposition runs for sixteen samples. Deposition rates were controlled within the range of 1-2 Å/s to achieve target thicknesses of 200 Å for silver, 500 Å for zinc, 500 Å for aluminum, 500 Å for copper, and 500 Å for tin as illustrated in Figure 5.4. Table 5.2 cross-references the sputtering deposition conditions with the corresponding contact stacks for various samples across multiple PVD runs in the study.

Figure 5.4: Cross-section of the metal contacts illustrating the stacking order and their thicknesses

Table 5.2: Cross-reference of Magnetron Sputtering Process Parameters and Contact Stacks for Different Samples in PVD Runs.

PVD Run #	Sample #	MS. Process Parameters			Contact Stack #
		Substrate Temp. [°C]	Power [W]	N_2-Flow [sccm]	
1	1, 2	300	200	10	1
2	3, 4	300	200	15	2
3	5, 6	300	200	20	3
4	7, 8	300	200	25	4
5	9, 10	300	250	10	1
6	11, 12	300	250	15	2
7	13, 14	300	250	20	3
8	15, 16	300	250	25	4

5.4.4 Electron Beam Evaporation

It is a PVD technique that enables the production of high-purity metal layers at high deposition rates. It effectively evaporates substances with high melting temperatures and

ensures strong bonding to the substrate surface. The e-beam evaporation method starts in an ultra-high vacuum environment, where the metal source and the substrate are positioned. A tungsten filament, located outside the deposition area, is heated by applying a high-voltage current, typically ranging from 5 to 10 kV. This heating causes the tungsten to emit electrons through thermionic emission. The emitted electrons are subjected to acceleration and focused toward the source metal using a combination of permanent magnets or electromagnetic lenses. The high-energy electrons transfer their kinetic energy to the source metal, causing it to heat up and evaporate. The evaporated atoms or molecules travel in a straight line through the vacuum chamber and deposit onto the surface of the sample, creating a thin layer.

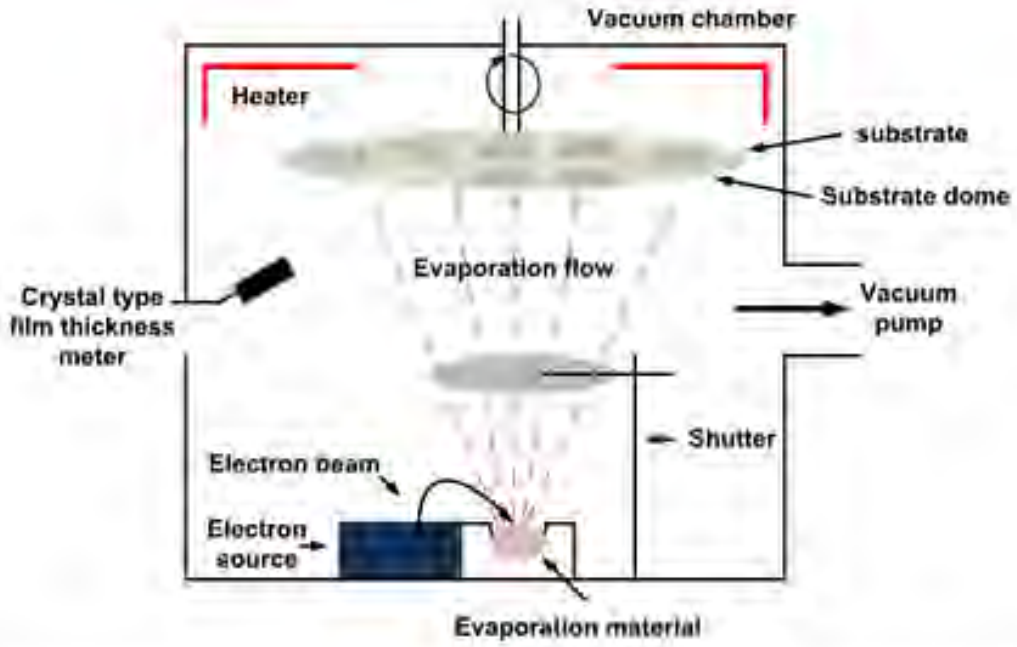

Figure 5.5: Schematic diagram of e-beam evaporation system [106]

5.4.4.1 E-Beam Evaporation Process Parameters

The Explorer E-Beam Evaporation System from Denton Vacuum was used to deposit platinum, palladium, and gold (Pt/Pd/Au) contact stacks in van der Pauw setup at the edges of 1 × 1 cm^2 p-type and n-type AlN samples after defining the contact pattern via photolithography. platinum (10 nm), palladium (10 nm), and gold (100 nm) multilayer contact stack was deposited at 0.1 nm/s controlled rate under a high-vacuum environment with a background pressure of approximately 1 × 10^{-6} Torr. The system is

equipped with quartz crystal monitors that provide real-time feedback on the deposition rate and thickness. Then, a lift-off process was performed using acetone for 20 minutes to define the desired contact patterns.

Figure 5.6: Cross-sectional view of the metal contacts showing the stacking order Pt/Pd/Au and their thicknesses

5.4.5 Rapid Thermal Annealing (RTA)

It is a crucial process in semiconductor manufacturing, employed to enhance materials' electrical and structural properties through controlled heating. This technique involves rapidly heating substrates to high temperatures using high-intensity lamps through precise temperature monitoring and feedback systems. The substrate is placed on a thermally isolated platform inside an RTA chamber, which is then exposed to the intense radiation from the lamps. The temperature can be ramped up quickly, often at rates exceeding several hundred degrees Celsius per second. After reaching the desired temperature, the sample is maintained at that level for a brief period, followed by a quick cooling phase. RTA is advantageous for applications requiring short processing times and precise temperature control. The rapid heating and cooling rates characteristic of RTA minimize thermal diffusion and prevent the degradation of materials, making it essential for modern semiconductor manufacturing.

5.4.5.1 Applications of RTA

In this study, RTA was utilized to enhance the characteristics of the deposited thin layers and metal contact stacks. RTA is commonly used:

- To activate implanted dopants in semiconductors.
- To relieve stress in thin films, reduce defects, and improve crystallinity.

- To promote the formation of metal nitrides or other compound phases at the metal-semiconductor interface, facilitating better charge carrier transport.
- The metals within a stack lead to the formation of alloys and intermetallic phases upon annealing which contribute to enhancing the electrical properties of the contacts.

5.4.5.2 RTA Process Parameters

RTA of the undoped AlN samples was performed using a rapid thermal processor equipped with high-intensity silicon carbide heating rods, which can reach temperatures as high as 1500 °C and have an output power of 2.5 kW. Samples were subjected to annealing cycles in the quartz processing tube using an automated handling system at 300 °C and 400 °C for 1 min and 10 min.s, followed by natural cooling. The system maintained a temperature accuracy of ±1 °C and a vacuum level of 10^{-5} torr (molecular pump) and 10^{-3} torr (mechanical pump). Two S-type thermocouples monitored the temperature within a 152 mm heating zone. Table 5.3 provides the annealing conditions and surface status (scratched or unscratched) for undoped AlN samples with different contact stacks. The fabricated Pt/Pd/Au metal stacks were subjected to rapid thermal annealing (RTA) in a MILA-3000 furnace under a purified nitrogen atmosphere. Annealing conditions were tailored to the specific doping type: 800 °C for 1 minute for the Be-doped AlN sample and 900 °C for 1 minute for the Si-doped AlN sample.

Table 5.3: Annealing Conditions for Different Samples

Contact Stack - 1				
Sample #	Sample 1	Sample 2	Sample 9	Sample 10
Scratched/Unscratched	unscratched	scratched	unscratched	scratched
Annealing temp, duration	300 °C, 1 min	300 °C, 10 min	400 °C, 1 min	400 °C, 10 min
Contact Stack - 2				
Sample #	Sample 3	Sample 4	Sample 11	Sample 12
Scratched/Unscratched	unscratched	scratched	unscratched	scratched
Annealing temp, duration	300 °C, 1 min	300 °C, 10 min	400 °C, 1 min	400 °C, 10 min

Contact Stack - 3				
Sample #	Sample 5	Sample 6	Sample 13	Sample 14
Scratched/Unscratched	unscratched	scratched	unscratched	scratched
Annealing temp, duration	300 °C, 1 min	300 °C, 10 min	400 °C, 1 min	400 °C, 10 min
Contact Stack - 4				
Sample #	Sample 7	Sample 8	Sample 15	Sample 16
Scratched/Unscratched	unscratched	scratched	unscratched	scratched
Annealing temp, duration	300 °C, 1 min	300 °C, 10 min	400 °C, 1 min	400 °C, 10 min

CHAPTER 6

CHARACTERIZATION

In this chapter, different methods employed to evaluate the characteristics of the fabricated samples are discussed. These techniques include Thickness Profilometry, Temperature-dependent Current-Voltage (IV) measurements, X-ray Diffraction (XRD), Spectroscopic Ellipsometry (SE), and Hall Effect Measurements (HEM). Each technique offers valuable insights into the materials' structural, electrical, and optical properties.

6.1 Thickness Profilometry

Thickness profilometry is a contact measurement technique. It employs a physical probe or stylus that is attached to a vertical sensor. This stylus is brought into contact with the surface of the sample, which is secured on a precision platform, and is moved laterally beneath the stylus. As the stylus glides across the surface, it dynamically adjusts its vertical position in response to the slightest changes in height to capture the intricate topography. The vertical movement of the stylus is transformed into electronic signals by an LVDT (Linear Variable Differential Transformer). These signals are then processed to generate a surface profile. is a commonly employed technique for characterizing film thickness and surface profile.

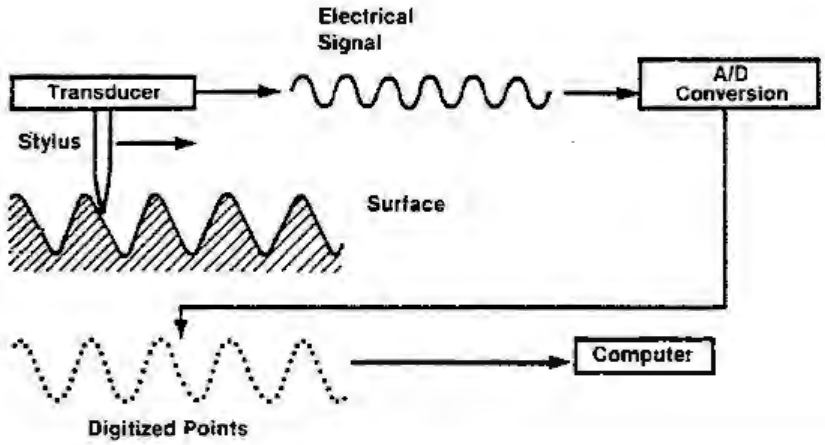

Figure 6.1: Schematic illustrating the operating principle of stylus profilometry [107]

6.1.1 Surface Profilometry Measurement Setup

The Bruker Dektak XT Stylus Profilometer was utilized for assessing the thickness and surface roughness of undoped AlN layers following magnetron sputter deposition. The instrument features 1 Å high vertical resolution and offers a broad measurement range of 10 nm - 1 mm. Additionally, it includes sophisticated data analysis capabilities. The fine diamond-tipped stylus features a radius of 12.5 µm, ensuring precise measurements. Surface profilometry was conducted on eight samples, each grown under varying magnetron sputtering process parameters. A measurement range of 6.5 µm was chosen, with 750 µm scanning length and a 5 mg stylus force. The profiling captured the intricate topography of hills and valleys, with a resolution of 0.25 µm per point in a measurement process duration of 10 seconds.

6.2 Spectroscopic Ellipsometry (SE)

It is an optical method that is both non-contact and non-destructive, employed to characterize the thickness of the layer, dielectric coefficient, refractive index, and extinction coefficient. It works by directing a polarized light beam on the sample at a specific angle. The reflection can cause changes in the phase and amplitude of the reflected light, so its polarization state changes, becoming elliptically polarized. These changes are dependent on the material's properties and the thickness of any layer present. This alteration is defined by two parameters: Ψ (Psi) and Δ (Delta).

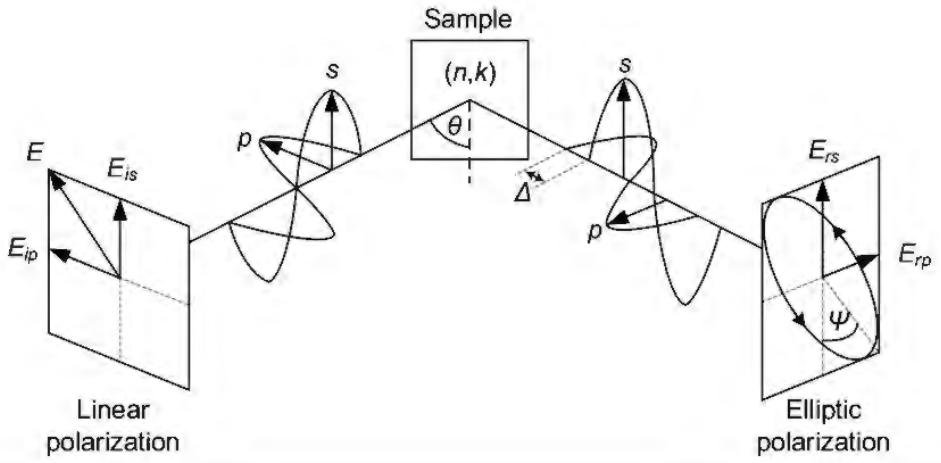

Figure 6.2: Schematic diagram of Spectroscopic Ellipsometry principle [108]

Where,

- Ψ represents the amplitude ratio of the reflected light's perpendicular (s) and parallel (p) components relative to the incidence plane.
- Δ signifies the phase disparity between the s- and p-polarized light waves after being reflected.

Ellipsometry analyzes the relative intensities and phase shifts for both s- and p-polarized light between the Fresnel coefficients of reflection:

$$r = \frac{r_p}{r_s} = \tan(\Psi)e^{i\Delta} \tag{6.1}$$

By measuring Ψ and Δ across various angles of incidence and wavelengths, the film's thickness, n, and k (optical constants) can be derived by matching the data to a theoretical model.

The optical characteristics and thickness of the AlN layers like the refractive index and absorption coefficient were examined utilizing the SENTECH SE 800 ellipsometer. This tool operates based on the Step Scan Analyser measurement mode which helps minimize mechanical errors by allowing all optical components to remain stationary during measurements. the system features a motorized x-y stage, enabling automated scanning of samples. The SE 800 utilizes a Xe-white light source and a diffraction grating to provide a broad spectral range for analysis. Light reflected off the AlN film is detected by two highly sensitive photodetectors. The collected data was analyzed, modeled, and fitted using

SpectraRay 3 software, which facilitated the extraction of optical constants and film thickness.

6.3 Scanning Electron Microscopy (SEM)

6.3.1 Principle of SEM

SEM is a versatile imaging technique capable of revealing the surface structure and material compositional details in micro- and nanoscales. In this method, a finely focused beam of electrons is produced by an electron gun, which generally employs field or thermionic emission sources. The electron beam is accelerated to a high voltage (1-30 kV) and directed toward the specimen through a set of apertures and electromagnetic lenses, which focus and control the beam's size and shape. When the electron beam interacts with the sample surface, it results in the emission of different signals:

1. ***Secondary Electrons (SE):*** Electrons having lower energy released from the surface of the sample, offer detailed information regarding surface topography.
2. ***Backscattered Electrons (BSE):*** The electrons having higher energy are reflected off the sample, creating a compositional contrast that highlights regions with distinct atomic numbers.
3. ***X-rays:*** When inner-shell electrons are ejected from the atoms in the sample, characteristic X-rays are produced. These X-rays have energies unique to each element, a principle used in energy-dispersive X-ray spectroscopy (EDS).

The signals emitted from the sample's surface are detected by specialized detectors: SE, BSE, and EDS detectors. In SEM, magnification is adjusted by altering the dimensions of the area that the electron beam scans, and it can range from approximately 10x to more than 500,000x.

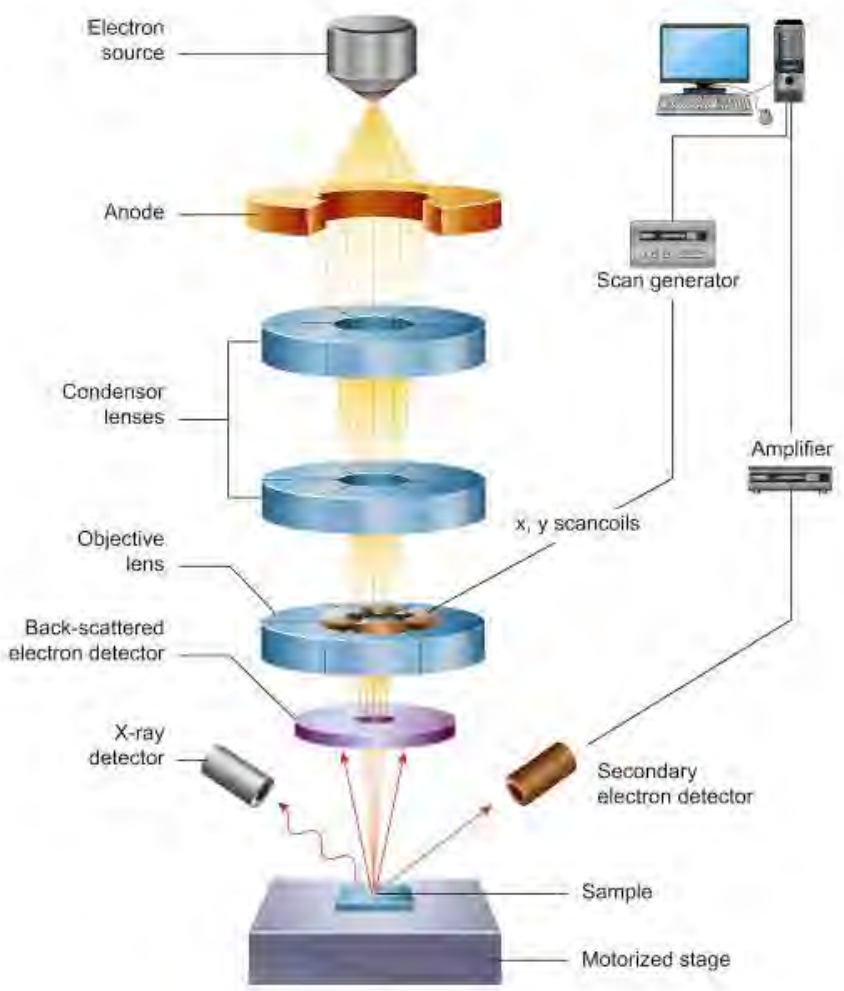

Figure 6.3: Schematic diagram of SEM principle [109]

6.3.2 Experimental Details

To examine the surface morphology of the deposited AlN layers, SEM was conducted utilizing a KYKY-EM6900 SE microscope. The samples were mounted on the five-axis stage within the SEM chamber and aligned under the electron beam. The system maintained a high vacuum environment using turbo molecular and rotation pumps. A tungsten filament was utilized as the electron source in this instrument. Electrons were thermionically emitted from the heated filament and were accelerated toward the sample using an accelerating voltage of 20kV. The electron beam was precisely focused onto the sample surface using the condenser and objective lenses. This tool is equipped with SE and BSE detectors to detect the electrons emitted from the sample. Images were captured at various

magnifications. The images obtained at different magnifications were analyzed with the integrated software to assess surface defects, roughness, and other structural characteristics.

6.4 Current-Voltage (I-V) Characterization

The measurements were conducted to evaluate the electrical properties of the fabricated samples utilizing the Automatic System for Material Electro-physical Characterization (ASMEC) from 300 K to 360 K temperatures in 10 K increments. Three different measurement configurations were used: the larger contact on AlN, the smaller contact on AlN, and a silicon-to-larger contact on AlN. For all samples, the voltage was adjusted in increments of 50 mV, ranging from -10 V to 10 V. Critical diode parameters were extracted including effective barrier height, saturation current, and Richardson constant to assess the transport mechanism in Schottky barrier diodes.

6.4.1 Thermionic Emission Current: Extraction of Parameters

The semiconductor carrier emission into the metal across a uniform barrier is the primary driver of forward bias carrier conduction in an ideal Schottky barrier diode. The I-V-T behavior of an undoped semiconductor can be effectively described through the thermionic emission model. From the thermionic emission theory,

$$ln\left[\frac{I}{1-e^{-\beta V}}\right] = \frac{\beta V}{n} + \ln\left(I_{sat}\right) \tag{6.2}$$

where β=q/kT with q signifies the electronic charge and k the Boltzmann constant (8.62×10^{-5} eV/K). The ideality factor is denoted by n, V represents the voltage drop across the Schottky diode, and I_{sat} represents the saturation current which can be described as:

$$I_{sat} = ST^2A^*e^{\frac{q\Phi_B}{kT}} \tag{6.3}$$

Applying the natural logarithm to both sides,

$$ln\left(\frac{I_{sat}}{ST^2}\right) = ln(A^*) + \frac{q\Phi_B}{kT} \tag{6.4}$$

where S denotes the contact area in cm^2, A* represents the Richardson constant's effective value, and Φ_B signifies the effective barrier height.

By comparing equation 6.4 with the standard linear equation in slop-intercept form, y = mx + c, the following relationships can be established:

$$y = ln\left(\frac{I_{sat}}{ST^2}\right), \qquad x = \frac{1}{kT}, \qquad m = q\Phi_B, \qquad and\ c = ln(A^*)$$

A semi-log plot of $\frac{I_{sat}}{ST^2}$ against $\frac{1}{kT}$ results in a straight line having an intercept of $\ln(A^*)$ and $q\Phi_B$ slope. From this plot, the effective Richardson constant (A^*) and effective Schottky barrier height ($\Phi_{B,eff}$) and can be calculated.

6.5 Hall Effect and Resistivity Measurements

These measurements were conducted on 1 × 1 cm² p- and n-type AlN samples, utilizing four contacts in the van der Pauw setup positioned at the samples' corners. An M91 FastHall Controller from Lake Shore Cryotronics was used to perform the characterizations. The HEMs were conducted using a 10-volt excitation source voltage. The blanking time was set to 1 second for AlN:Be and 500 milliseconds for AlN:Si sample. A 1 Tesla magnetic field was directed at right angles to the sample surface. Current responses were recorded as the voltage was varied from -10 V to +10 V. The measurement range was adjusted to 10 µA-1 V for p-type and 10 mA-10 V for n-type AlN to accommodate the different resistivity values.

6.5.1 Resistivity Measurements

For the resistivity measurements, a steady current was passed through two neighboring contacts, and the voltage was recorded between the two contacts positioned opposite them. The configuration was then rotated by 90° to change the current and voltage contact pairs. The resistances R_A and R_B were calculated using the following expressions:

$$R_A = \frac{V_{43}}{I_{12}}\ and\ R_B = \frac{V_{14}}{I_{23}} \tag{6.4}$$

When current is applied through contacts 2 and 1, the voltage measured across contacts 3 and 4 is V_{43}, and when current is applied through contacts 3 and 2, the voltage recorded

across contacts 4 and 1 is V_{14}. The van der Pauw equation can be used to calculate the sheet resistance R_s, which relates the characteristic resistances R_A and R_B to R_S as follows:

$$e^{\frac{-\pi R_A}{R_s}} + e^{\frac{-\pi R_B}{R_s}} = 1 \tag{6.5}$$

Once R_S is determined, the bulk resistivity ρ is calculated by multiplying the thickness (d) of the AlN layer by R_S:

$$\rho = R_s d \tag{6.6}$$

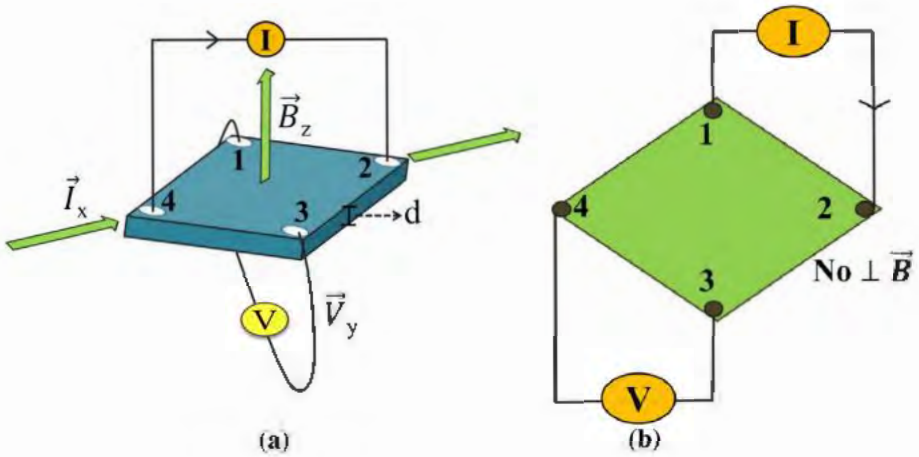

Figure 6.4: Schematic representation of van der Pauw technique applied for (a) Hall effect measurements and (b) Resistivity measurements [110]

6.5.2 Hall Effect Measurements

HEMs provide critical insights into the mobility, concentration, and charge carriers nature in semiconductor materials. When a semiconductor with an electric current is placed in a perpendicular magnetic field, the charge carriers are subjected to a Lorentz force, which causes them to accumulate on one side of the material. This accumulation of charge carriers is referred to as the Hall effect. This occurrence is referred to as the Hall effect. The Hall voltage (V_H) is the potential difference produced by this accumulation.

The carrier concentration and the applied magnetic field both affect the Hall voltage's magnitude, while its sign indicates the type of charge carrier (positive for holes, negative for electrons). These measurements were conducted by applying a constant current to one

pair of diagonal contacts on the samples while subjecting them to a perpendicular magnetic field. The remaining two contacts were used to record the V_H, with the process repeated after reversing the current and the magnetic field.

The following equation is used to compute the Hall coefficient (R_H):

$$R_H = \frac{tV_H}{BI} \tag{6.6}$$

where V_H and I represent the RMS values of the averaged Hall voltage and applied current respectively.

CHAPTER 7

RESULTS AND DISCUSSION

7.1 Thickness Profile Analysis

Thickness profilometry measurements were performed following the magnetron sputtering process to characterize the thickness and surface topography of the deposited AlN thin layers. Key features extracted from the profile include film thickness, surface roughness, and potential defects or variations. Figure 7.1 (a) illustrates a 2D cross-sectional analysis of the AlN film surface profile of sample 1 across a specified length. The average vertical displacement between the AlN film's peak and the silicon substrate's baseline represents the film thickness. The height data indicates a relatively consistent thickness across the measured area, with values fluctuating between 80-106 nm.

The 3D surface topography visualization in Figure 7.1 (b) shows the thickness profile across the AlN thin film of sample 1. The color gradient indicates variations in height, with red areas representing higher elevations and blue areas indicating lower regions. The color bar on the right quantifies the thickness variation. It ranges to approximately 106.48 nm (red regions), The relatively smooth gradient suggests a homogeneous film with minimal defects. 3D surface profiles of samples 3, 5, 7, 9, 11, 13, and 15 are shown in Figures 7.2 (a-g) respectively.

The irregularities in the film profile indicate surface roughness. A relatively flat profile suggests good uniformity, while significant deviations indicate thickness variations. Statistical parameters such as average roughness (Pa), root mean square (RMS) roughness (Pq), skewness (Psk), kurtosis (Pku), average max height (Pz), max peak height (Pp), max valley depth (Pv), and maximum height between the highest peak and the lowest valley (Pt) over a specified sample length were calculated to quantify the surface topography. Skewness measures the asymmetry of the surface height distribution. A positive skew suggests a dominance of peaks, whereas a negative skew implies more valleys. A

skewness value approaching zero suggests a symmetrical distribution of film thicknesses. Kurtosis provides insight into the distribution of surface features. A high kurtosis value suggests a sharply peaked distribution with steep slopes, whereas a low kurtosis value indicates a flatter surface profile. These statistical parameters for all the magnetron sputtered-AlN samples are detailed in Table 7.1.

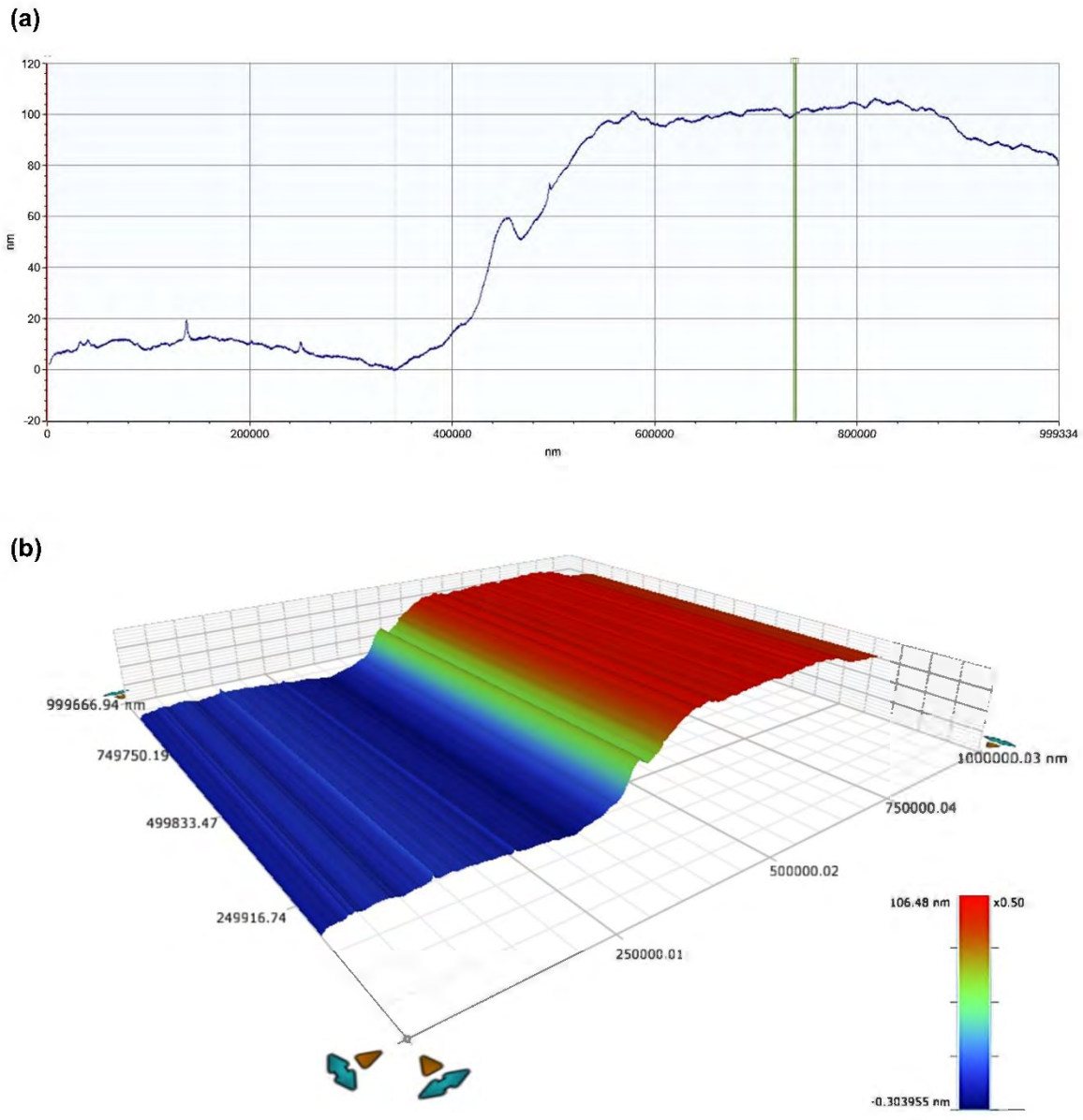

Figure 7.1: (a) 2D cross-sectional image and (b) 3D image of the surface topography of the AlN thin film in sample 1

(a)

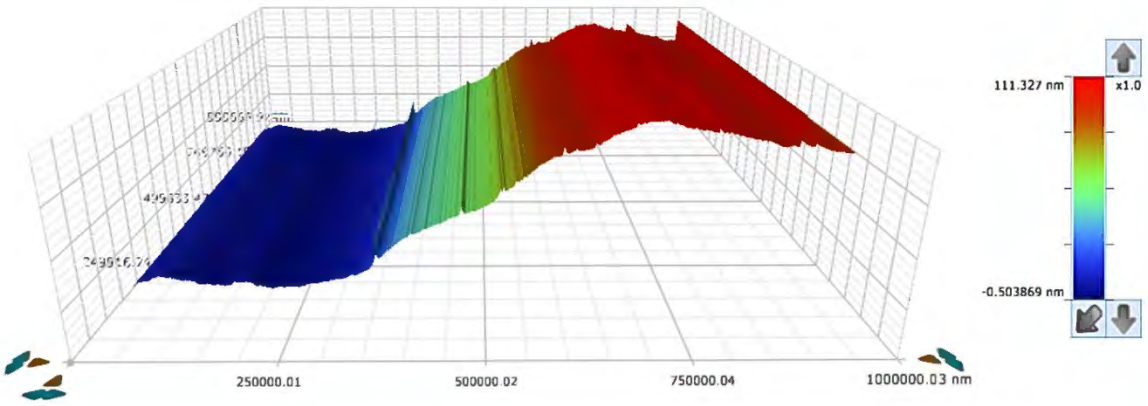
111.327 nm
x1.0
-0.503869 nm
250000.01
500000.02
750000.04
1000000.03 nm

(b)

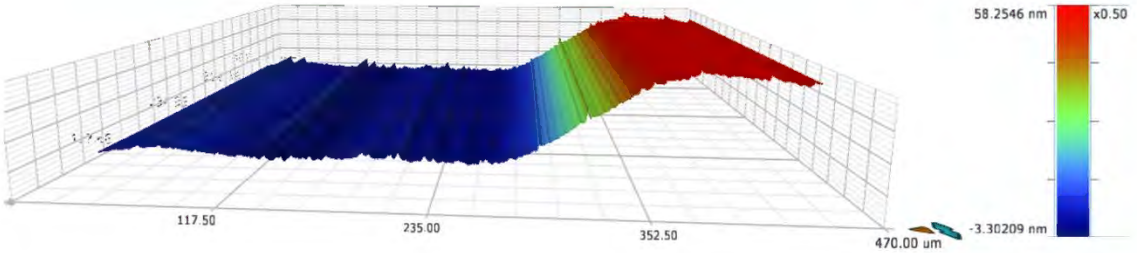
58.2546 nm
x0.50
-3.30209 nm
117.50
235.00
352.50
470.00 um

(c)

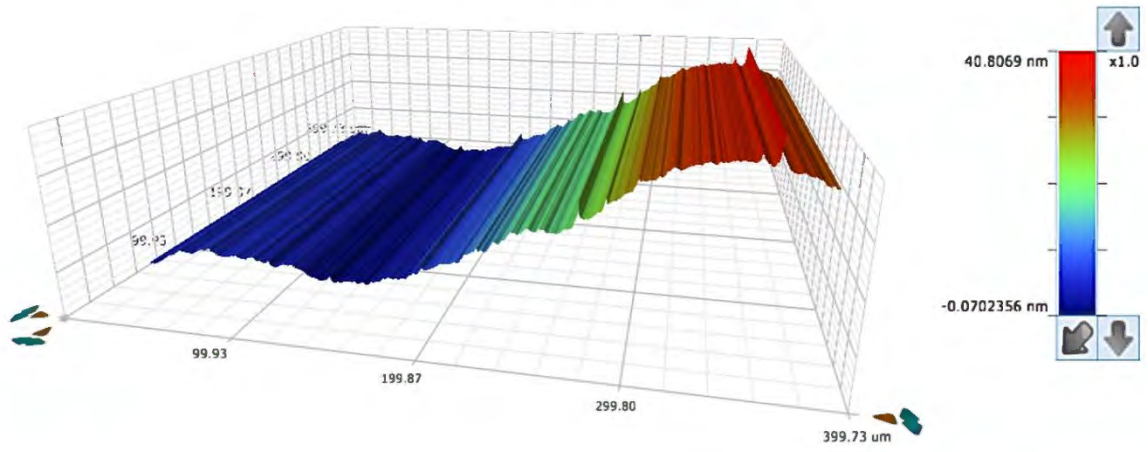
40.8069 nm
x1.0
-0.0702356 nm
99.93
199.87
299.80
399.73 um

(d)

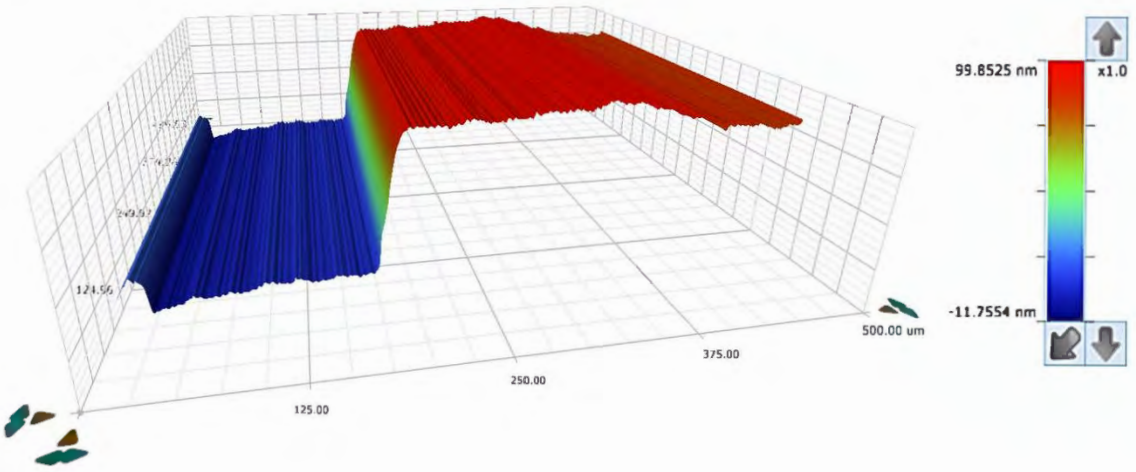
99.8525 nm
x1.0
-11.7554 nm
124.56
125.00
250.00
375.00
500.00 um

(e)

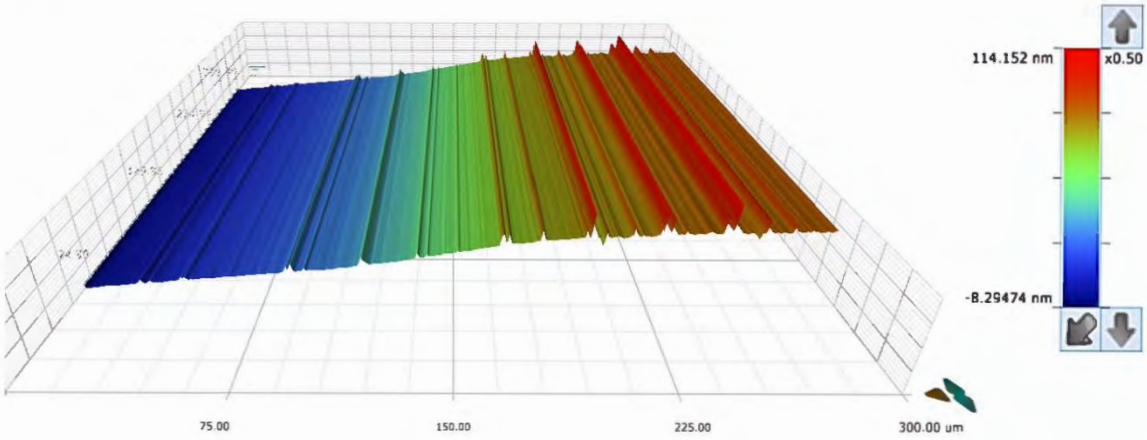
114.152 nm
x0.50
-8.29474 nm
75.00
150.00
225.00
300.00 um

(f)

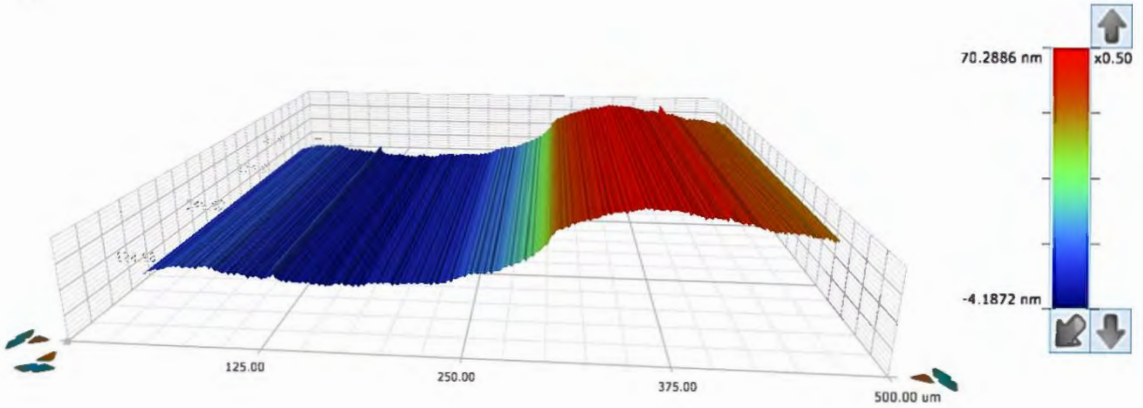
70.2886 nm
x0.50
-4.1872 nm
125.00
250.00
375.00
500.00 um

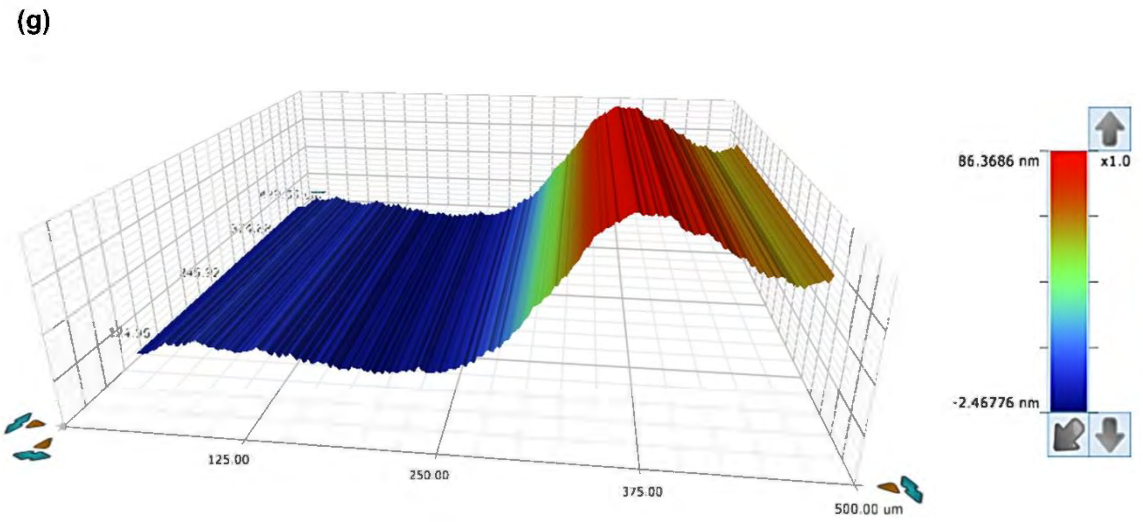

Figure 7.2: 3D surface profile of the AlN thin layers in samples 3, 5, 7, 9, 11, 13, and 15, shown in (a) to (g), respectively

Table 7.1: Surface Profilometry Results for Thickness and Statistical Roughness Parameters

Sample #	Thickness Achieved [nm]	Pa [nm]	Pq [nm]	Psk	Pku	Pz [nm]	Pp [nm]	Pv [nm]	Pt [nm]
1	100.06	1.371	1.73	0.023	2.493	7.89	4	3.89	7.89
3	100.87	2.11	2.32	-0.172	1.591	8.22	3.91	4.31	8.22
5	52.19	1.181	1.47	-0.094	2.797	7.78	4.32	3.46	7.78
7	32.56	1.24	1.32	0.066	1.37	4.05	2.22	1.83	4.05
9	97.94	1.48	1.73	0.403	2.238	7.87	4.31	3.57	7.87
11	76.09	4.45	7.06	2.693	11.272	49.14	36.16	13.01	49.17
13	65.65	2.17	2.55	-0.429	2.084	9.87	4.45	5.43	9.87
15	78.72	1.41	1.69	-0.638	2.324	6.39	2.48	3.92	6.39

7.2 Spectroscopic Ellipsometry Analysis

Spectroscopic ellipsometry (SE) was utilized to examine the optical characteristics and thickness of the deposited AlN thin layers. The findings, outlined in Table 7.2, show that the AlN films consistently achieved a thickness close to 100 nm across all samples, with an average of 97.62 nm.

Table 7.2: Summary of Spectroscopic Ellipsometry Results

Sample #	Thickness Achieved [nm]	% Error in Thickness
1	90.71	1.99
2	97.94	1.90
3	99.77	0.57
4	100.54	0.84
5	99.88	0.60
6	95.00	1.83
7	98.50	1.61
8	98.83	1.99
9	95.77	1.82
10	96.76	0.73
11	98.41	1.20
12	97.96	1.73
13	96.00	1.44
14	95.53	2.58
15	100.00	0.70
16	100.38	0.66

Figure 7.3 (a) illustrates the refractive indices of the AlN thin films across a spectral range of 300 to 2500 nanometers. It reflects how light propagates through the material and varies with wavelength (dispersion). The refractive index values for most samples range between approximately 2.1 and 2.3, which is consistent with the values reported for AlN layers, implying that the films exhibit good transparency in the visible near-IR regions [111], [112]. The slight variations among samples can suggest differences in film quality and thickness. Samples 1 and 2 show notable deviations from the general trend, with significantly lower refractive indices, especially in the longer wavelength region. Lower refractive index values for S1 and S2 might suggest lower density or increased porosity of the films, deviations in material composition, or interference due to an unintended intermediate layer (e.g., SiO_2).

Figure 7.3 (b) represents the absorption coefficient of AlN films for the samples over a similar range of wavelengths. The absorption coefficient provides insights into the material's capacity to absorb light at specific wavelengths. Most samples exhibit relatively low absorption, which decreases steadily as the wavelength increases, especially in the NIR range indicating transparency in this region. The negative values of absorption coefficients in the data are not physically meaningful and typically indicate an issue with the data analysis, experimental noise, or model fitting errors. Samples 1 and 2 display significantly higher absorption coefficients indicating that these samples might have lower-quality films with more defect states, structural defects, or variations in stoichiometry, leading to higher absorption.

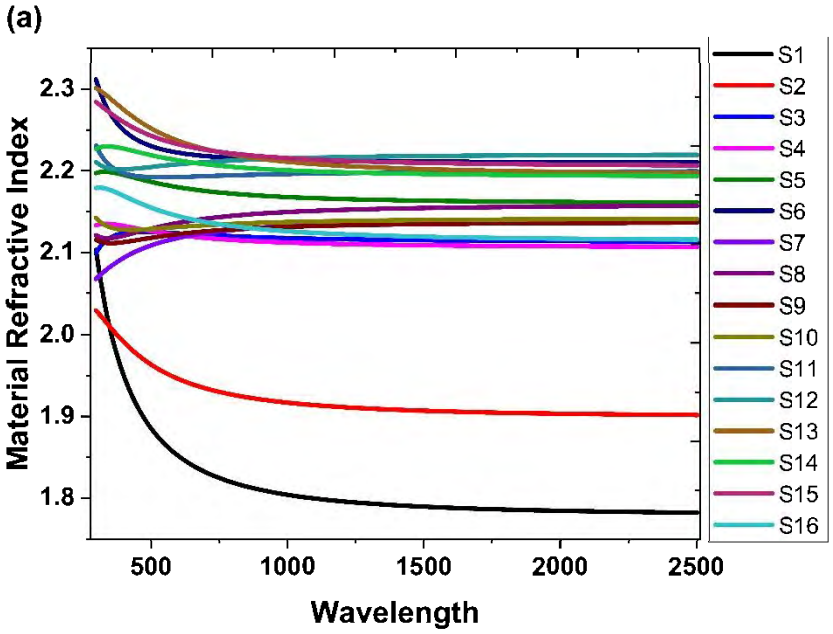

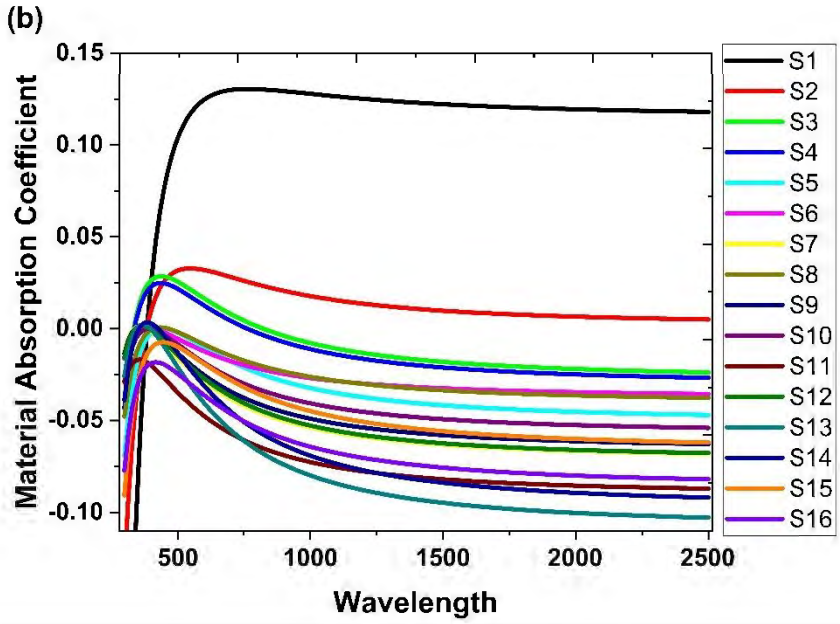

Figure 7.3: (a) Refractive indices and (b) absorption coefficients of the AlN thin layers over 300 to 2500 nanometers spectral range.

7.3 SEM Analysis

The SEM analysis investigated the surface morphology, structural features, and potential defects on the AlN thin films deposited on silicon substrates. The SEM images were captured at varying magnification scales to assess the large-scale surface characteristics and finer structural details. Figures 7.4 (a) and (b) provide insights into the surface characteristics of the sample 2. A notable crack measuring around 1.62 µm is visible running across the sample, indicating mechanical stress or defects during deposition or post-deposition processing. The film surface appears to have rough areas, with some irregularities and small particles dispersed randomly across the sample which might be residual contaminants or artifacts from the deposition chamber or contamination during handling requiring improved cleaning procedures or environmental control.

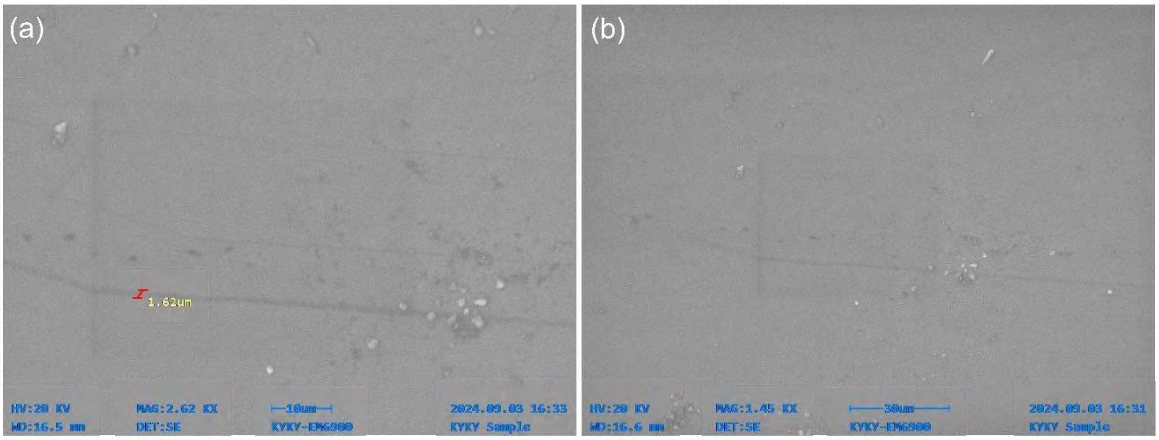

Figure 7.4: SEM images of Sample 2, captured at magnifications of (a) 10 µm and (b) 30 µm

Figures 7.5 (a) and (b) present SEM images of the surface of Sample 8. The images reveal the presence of tiny features on the surface, which may indicate surface defects such as pits, scratches, cracks, or impurities within the AlN film. Despite these minor imperfections, the overall surface appears smooth and exhibits no significant irregularities, suggesting a high degree of uniformity in most areas.

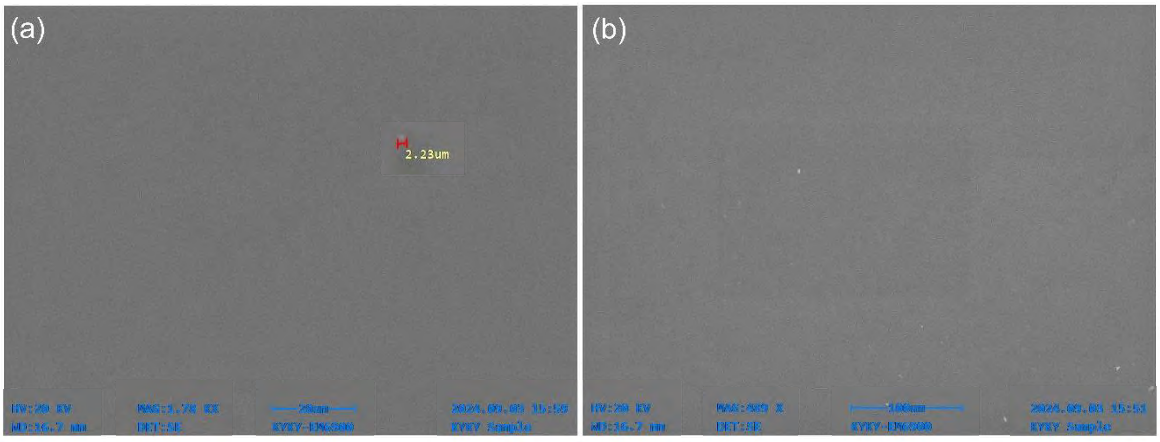

Figure 7.5: SEM images of Sample 8 at (a) 20 µm and (b) 100 µm scales

Figure 7.6 (a-d) presents a series of SEM images showcasing the surface morphology of Sample 9 at different magnifications. Figure 7.6 (a) shows a relatively smooth and uniform surface with a localized defect which seems to be mechanical damage or strain applied to the film. Minimal surface roughness or a few irregularities or cracks are visible in Figure 7.6 (b) which might have resulted from stress arising from the difference in thermal

expansion coefficients between AlN and silicon. Figure 7.6 (c) indicates that the AlN film surface is not perfectly smooth. There appears to be a degree of surface roughness, as evidenced by the presence of non-uniform regions and scattered, textured areas. The imperfections on the surface could stem from non-uniform deposition during the sputtering process. Variations in the deposition rate or temperature could cause such defects.

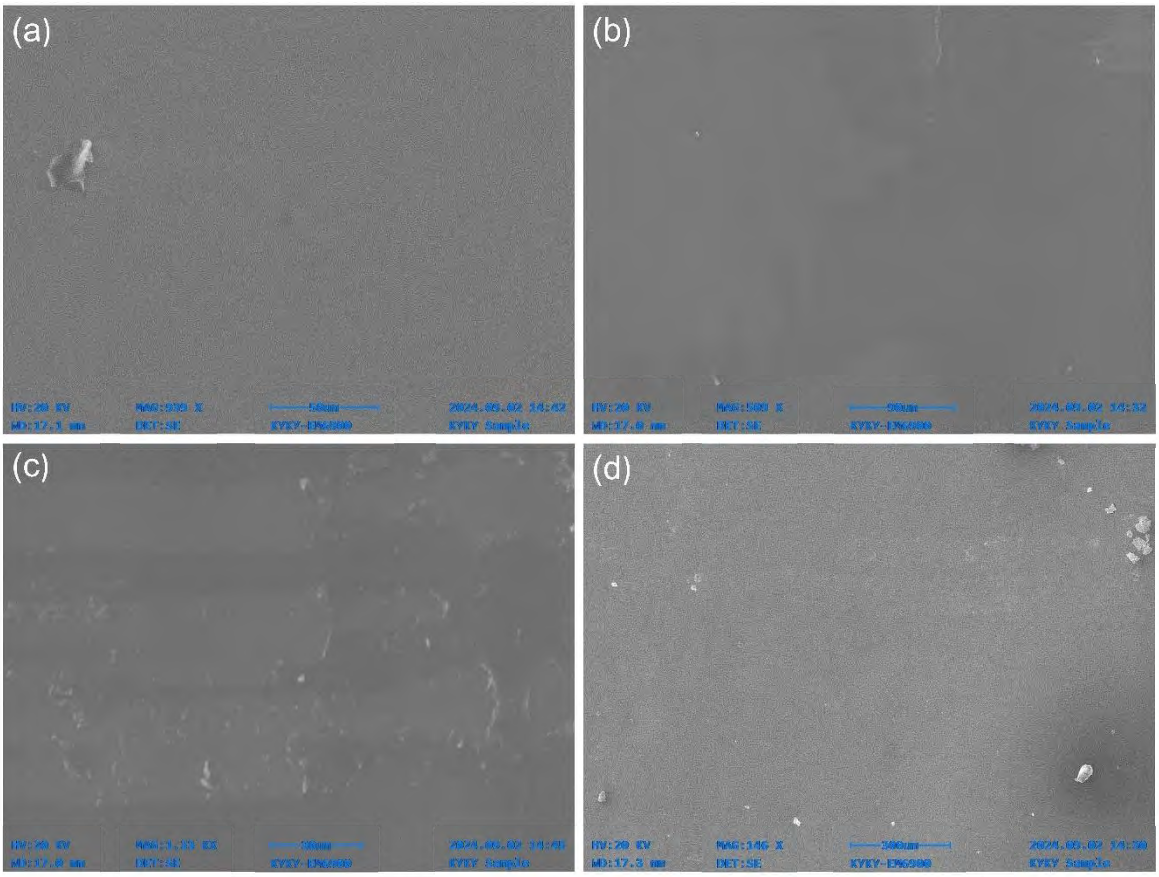

Figure 7.6: SEM images of Sample 9 at various magnifications with a scale bar of (a) 50 µm, (b) 90 µm, (c) 10 µm, and (d) 300 µm

Figures 7.7 and 7.8 provide insights into the surface morphology of Samples 11 and 13, respectively. The Figures show faint parallel lines that seem to extend across the surface. The surface of Sample 13 shows multiple intersecting lines and textures, suggesting possible microstructural changes within the film. A larger, more prominent crack measuring around 5.33 µm is evident in Figure 7.8 (a). The crack extends over a significant portion of the sample, highlighting areas of structural weakness. They might indicate that

the processing parameters used for these samples resulted in higher internal stress within the films or external strain forces acting upon the AlN film.

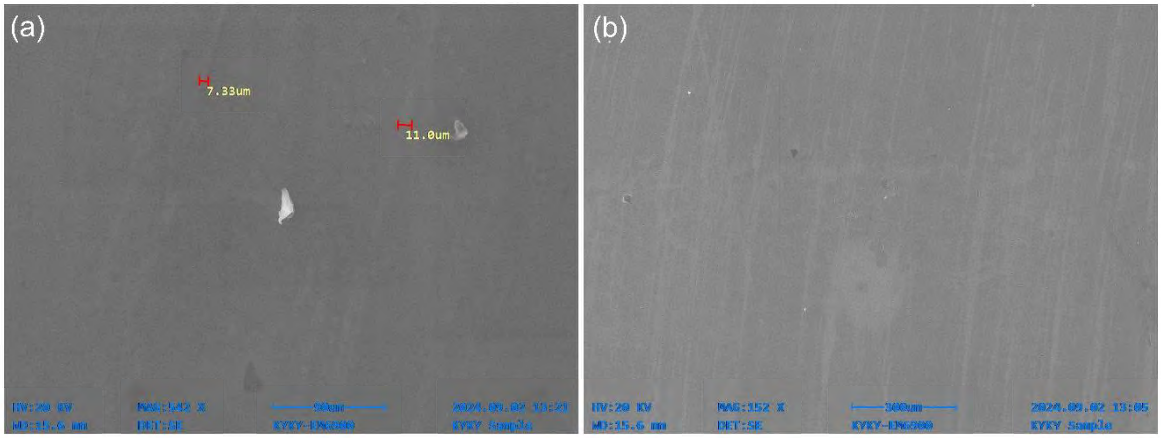

Figure 7.7: SEM images of Sample 11 at (a) 90 µm and (b) 300 µm scales

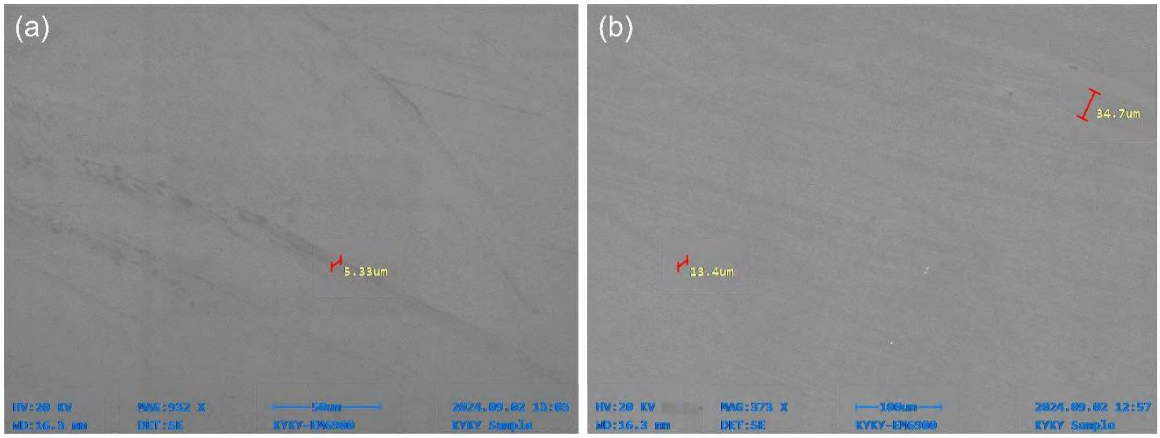

Figure 7.8: SEM images of Sample 13 at (a) 50 µm and (b) 100 µm scales

7.4 Current-Voltage Characteristics

These measurements were performed on the undoped AlN/Si samples to evaluate their electrical behavior. These measurements were performed on three contact configurations: larger contact**,** smaller contact**,** and larger contact to the silicon substrate**.** Below are the detailed results and analysis for selected samples: samples 2, 8, 11**,** and 13**.**

Figures 7.9 (c) and (d) display the I-V behavior of samples 11 and 13 respectively revealing higher than expected currents for all measurement configurations. AlN is an ultra-wide

bandgap semiconductor material (~6.1 eV bandgap), so ideally, the current flowing through the high resistivity undoped AlN samples should be relatively small depending on the thickness, film quality, and contact resistance. The high currents suggest the AlN layers in these samples have significant defects such as cracks, pinholes, thin regions, or impurities that can create paths for the leakage currents to flow. These leakage paths allow currents to bypass the AlN layer resulting in short-circuit or direct conduction between the underlying silicon substrate and the top contact stack. There can be a small contribution in the currents from localized tunneling through these defects. The increased larger contact-silicon current further supports the hypothesis of shorting through the Si substrate due to defects. The higher current through the smaller contact in sample 11 suggests that the smaller contact region has an even more pronounced leakage or defect concentration. This could be due to the non-uniform deposition of the AlN layer in this region or higher defect density near the smaller contact. The rest of the samples not mentioned here showed similar IV characteristics. Figure 7.9 (a) illustrates the current-voltage behavior of Sample 2. The current levels in this sample are also unusually high for undoped AlN and this could suggest that sample 2 may have some level of short-circuiting or leakage through defects in the AlN layer.

Sample 8 exhibited IV characteristics (shown in Figure 7.9 (b)) consistent with the insulating nature of undoped AlN. The I-V measurements showed currents in nanoamperes across all contact configurations with the least amount of current for top-to-bottom indicating that minimal to no current is flowing from the silicon substrate. These results align well with the expected behavior of undoped AlN, indicating that this sample has a relatively intact and defect-free AlN film.

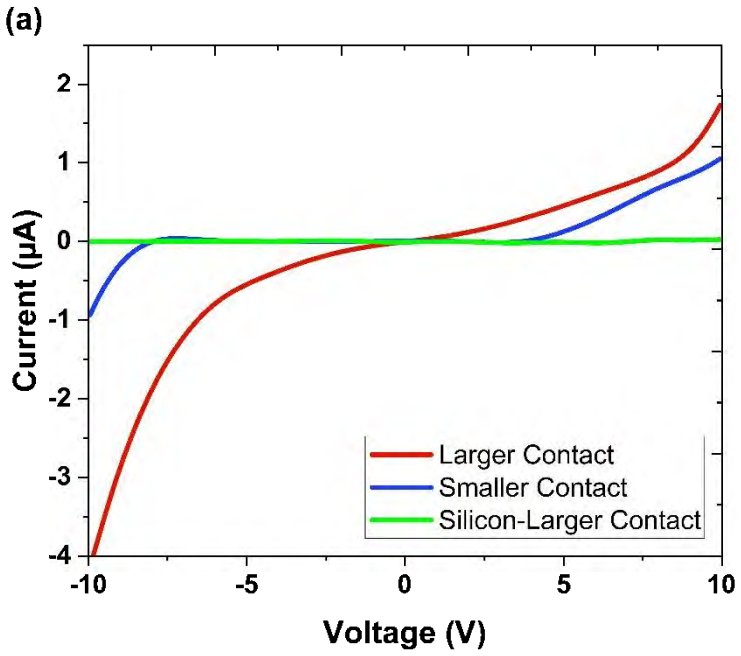
(a)
Current (μA)
Voltage (V)
Larger Contact
Smaller Contact
Silicon-Larger Contact

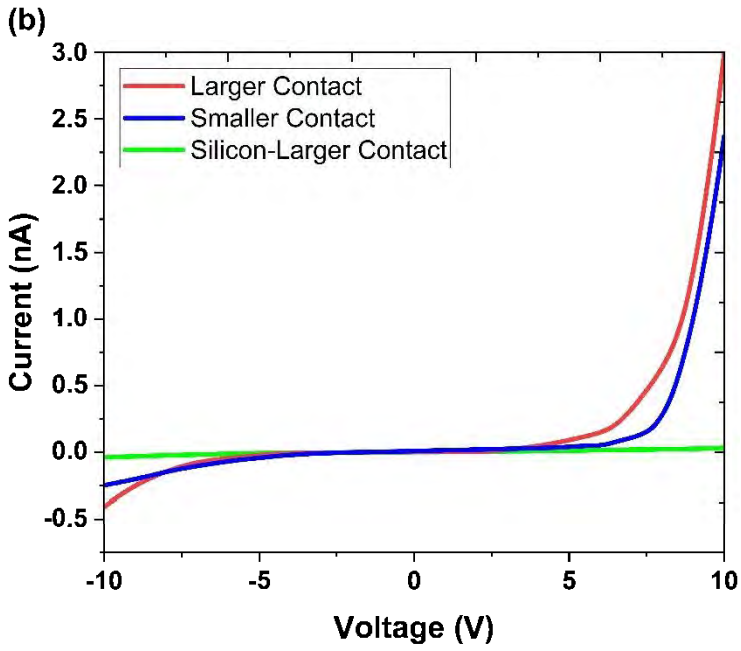
(b)
Current (nA)
Voltage (V)
Larger Contact
Smaller Contact
Silicon-Larger Contact

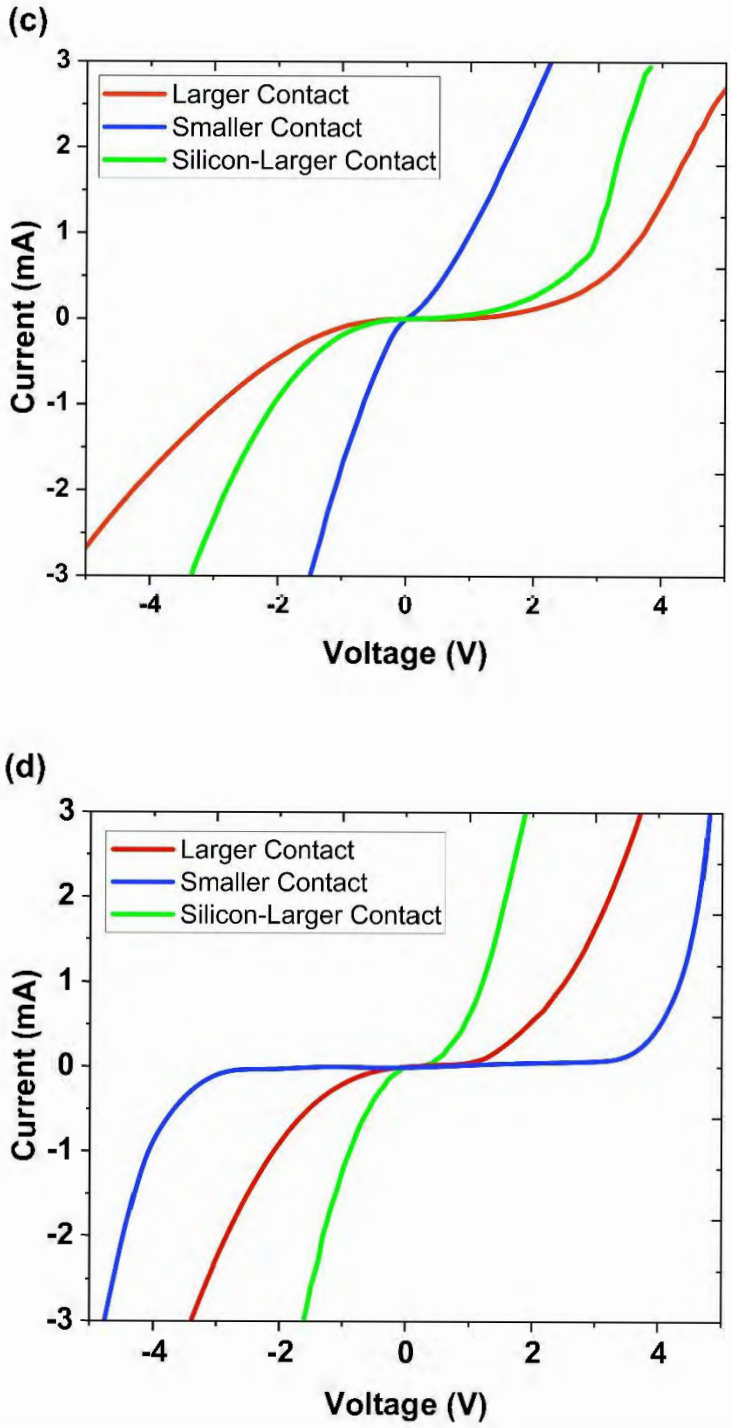

Figure 7.9: Current-voltage behavior of Samples (a) 2, (b) 8, (c) 11, and (d) 13

7.4.1 Temperature-Dependent I-V Characterization

IVT behaviors were plotted to examine the current transport mechanisms and extract key diode parameters. IVT characteristics over the 300 K to 360 K temperature range on

samples 2, 8, 11, and 13 are shown in Figure 7.10 (a-d). The abrupt change in the forward and reverse currents with temperature in samples 2, 11, and 13 suggests the presence of defects, which introduce additional current transport mechanisms and facilitate thermally activated processes, leading to a more complex and non-linear temperature-dependent I-V behavior. One possible explanation is the formation of localized states within the bandgap due to these defects. These defect states can trap charge carriers at lower temperatures, leading to trap-assisted conduction mechanisms. As the temperature increases, the carriers gain enough thermal energy to escape these traps, reducing the overall current. The non-linear behavior can be attributed to the varying activation energies of different conduction paths, leading to a more complex temperature dependence.

The I-V curves of sample 8 shift towards higher currents and ohmic behavior with increasing temperature implying a reduction in the effective Schottky barrier height as temperature increases, facilitating easier charge carrier transport. Sample 8 also exhibited a more linear I-V behavior compared to the other samples. These suggest that thermionic emission is the dominant current transport mechanism. This process follows a linear relationship with temperature and shows no significant contributions from tunneling or defect-assisted conduction. This indicates that the sample is uniform and defect-free across the contact area.

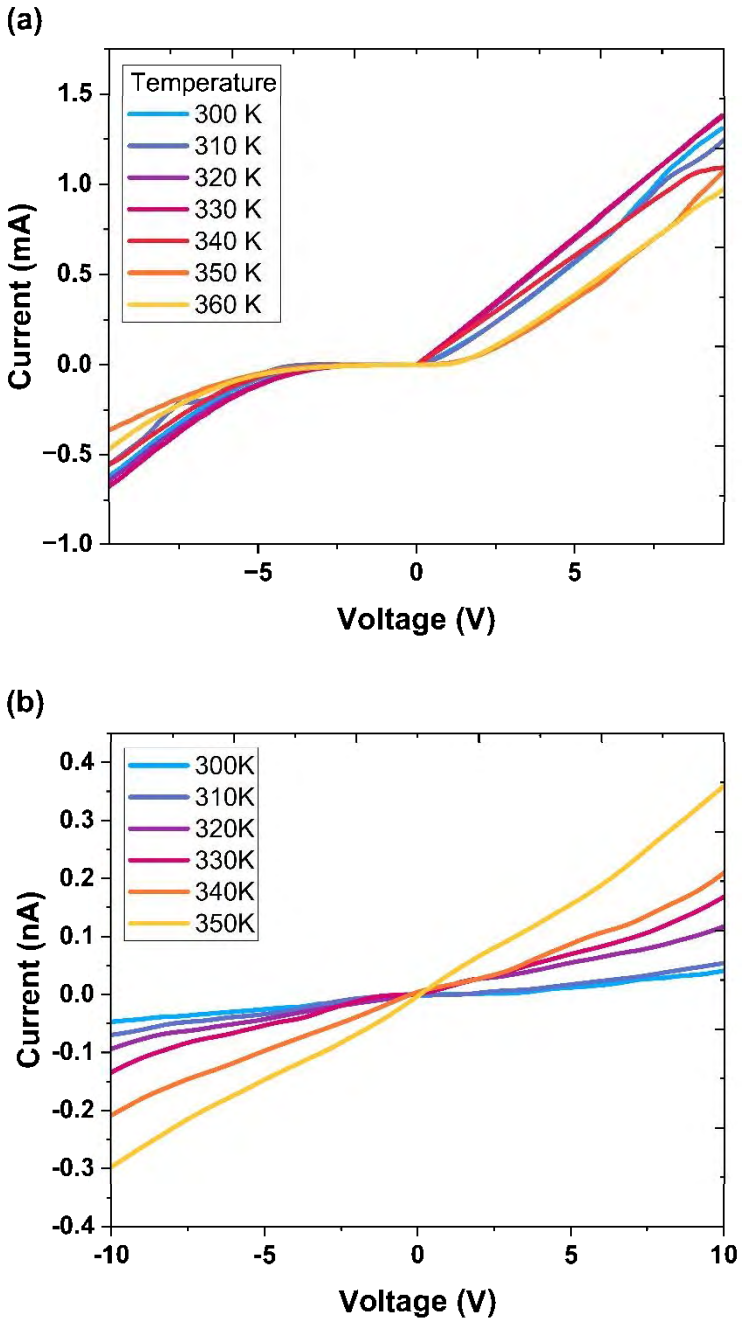
(a)
Temperature
300 K
310 K
320 K
330 K
340 K
350 K
360 K
Current (mA)
Voltage (V)
(b)
300K
310K
320K
330K
340K
350K
Current (nA)
Voltage (V)

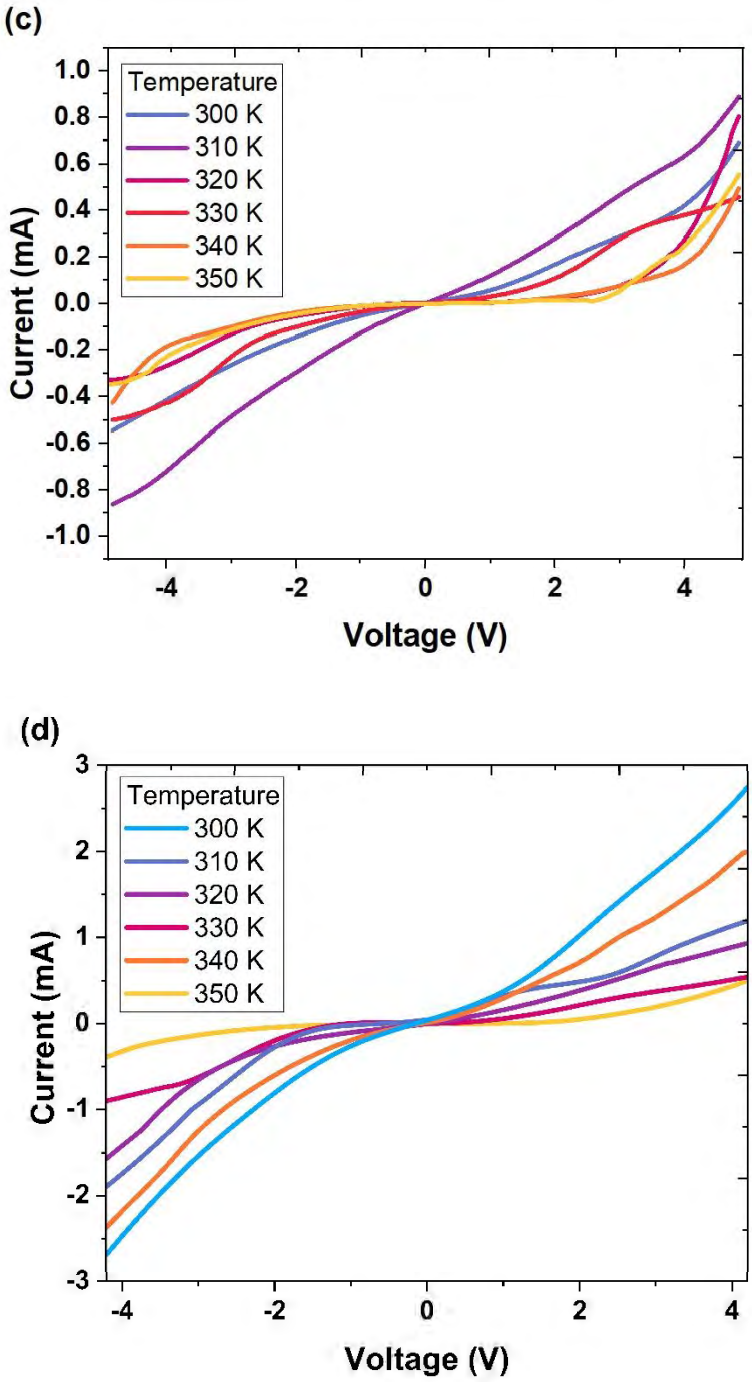

Figure 7.10: Temperature-dependent I-V behavior of Samples (a) 2, (b) 8, (c) 11, and (d) 13 measured over the 300 K to 360 K temperature range.

The saturation current (I_{sat}) at different temperatures, varying from 300 to 360 K, was determined from the Y-intercepts of the I-V-T plots. Richardson plots were then generated by plotting ln (I_{sat}/ST^2) against 1/kT as shown in Figure 7.11 (a-d), where S represents the

contact area (0.06 cm^2 in this case). By fitting the experimental data of the Richardson plot, the effective Richardson constant (A*) and Schottky barrier height (Φ_B) were determined from the intercept and slope respectively, provided in Table 7.3.

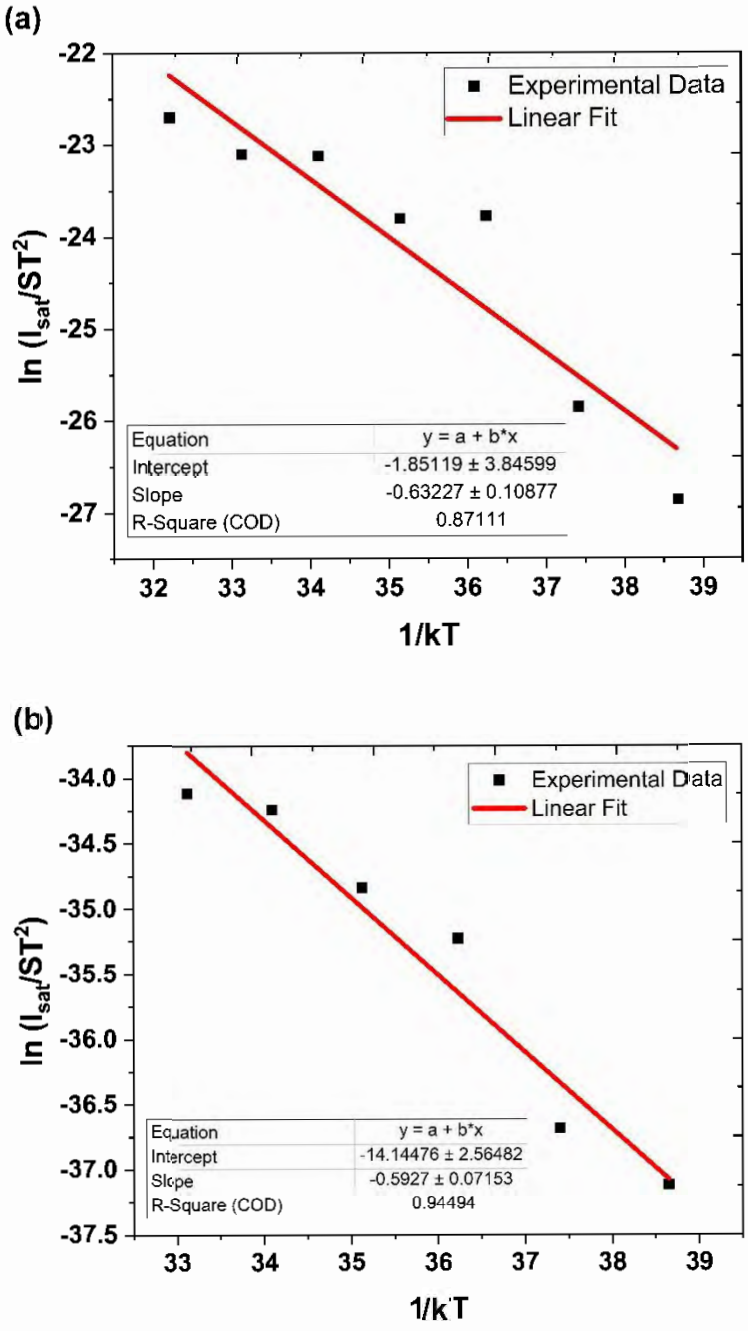

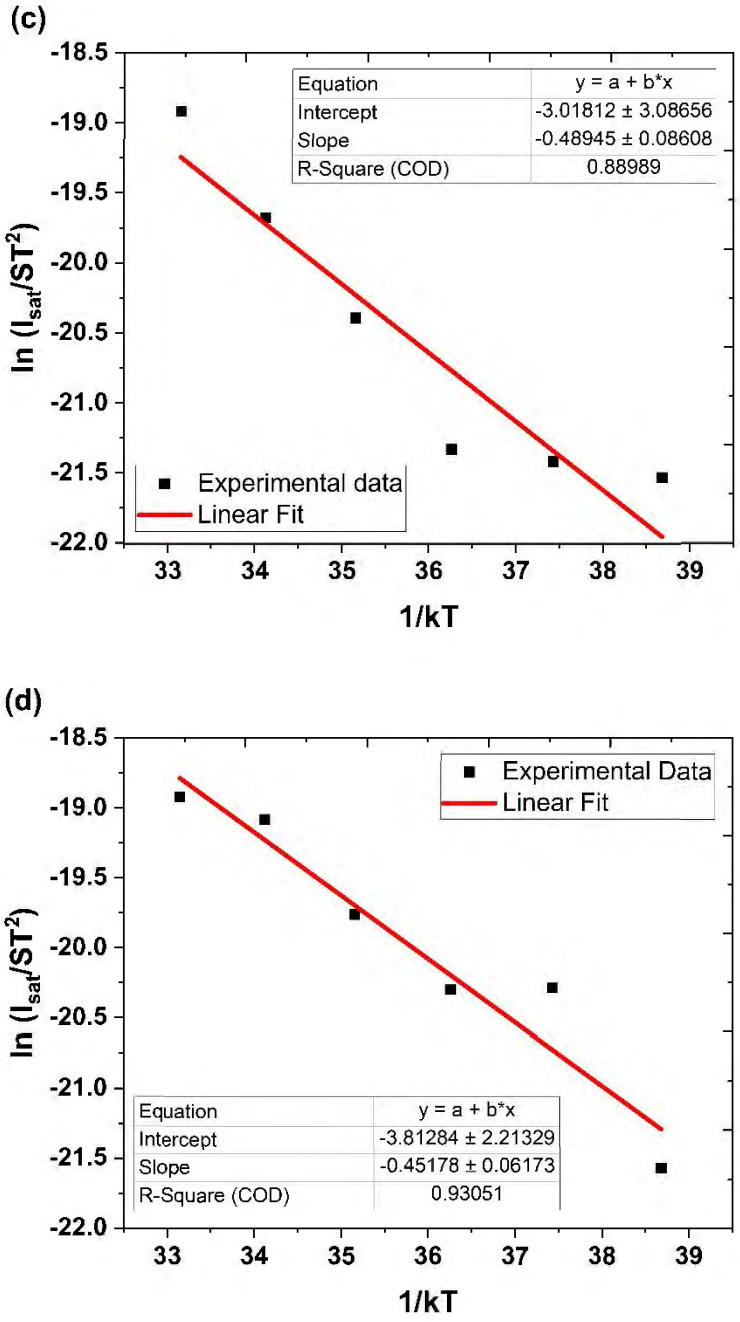

Figure 7.11: Richardson plot depicting the relationship between ln (I_{sat}/ST^2) and 1/kT, for samples (a) 2, (b) 8, (c) 11, and (d) 13

Table 7.3: Extracted values of effective Richardson's constant (A*) and Schottky barrier height ($q\Phi_{B,eff}$) for samples 2, 8, 11, and 13

Sample #	A* [A/cm^2.K^2]	$q\Phi_{B,eff}$ [eV]

2	0.157	0.63
8	7.19×10^{-7}	0.59
11	0.048	0.48
13	0.022	0.45

The observed lower Schottky barrier heights for samples 2, 11, and 13 [94], [113] reinforce the hypothesis of defect-induced conduction. Defects can facilitate increased current flow by allowing leakage currents and direct conduction through the silicon substrate, leading to an apparent reduction in the SBH. The effective Richardson constant, in this context, reflects a modified understanding of thermionic emission that accounts for the thermionic emission process at the metal-silicon interface and includes interference from defects and leakage. The Richardson constant for sample 8 is much smaller than the other samples which is an indication of defect-free AlN film. The metal-AlN contact in Sample 8 has a lower barrier height, which can be attributed to the specific metal stack used and the quality of the AlN film.

7.5 Resistivity and Hall Effect Measurements

7.5.1 Beryllium-doped AlN Films

The electrical conductivity of the Be-doped AlN samples with Pt (10 nm)/Pd (10 nm)/Au (100 nm) contact stacks after annealing was evaluated using Hall effect measurements. The I-V behavior of the annealed Pt/Pd/Au contacts on the Be-doped AlN sample at 800 °C annealing temperature is shown in Figure 7.12. These IV characteristics exhibit linear behavior across the four different contact pairs. The high R^2 values, approaching unity, confirm the direct correlation between voltage and current, indicating the ohmic nature of the contacts within the applied voltage range. The experimental results for the Be-doped AlN sample yielded a reliable resistivity (ρ) value of 1.642 Ω·cm ± 1.64 mΩ·cm with an SNR of 1003. The Hall effect measurements provided a significant mobility value of 13 ± 0.337 $cm^2/(V\cdot s)$, a positive Hall coefficient of 21.3 ± 554 cm^3/C confirming that holes are the predominant charge carriers and the Hall voltage came out to be -111 μV ± 2.873 μV with an SNR of 38.55. The Hall measurements indicated an active hole concentration of $2.92 \times 10^{17} \pm 7.58 \times 10^{15}$ cm^{-3} for the Be-doped AlN sample.

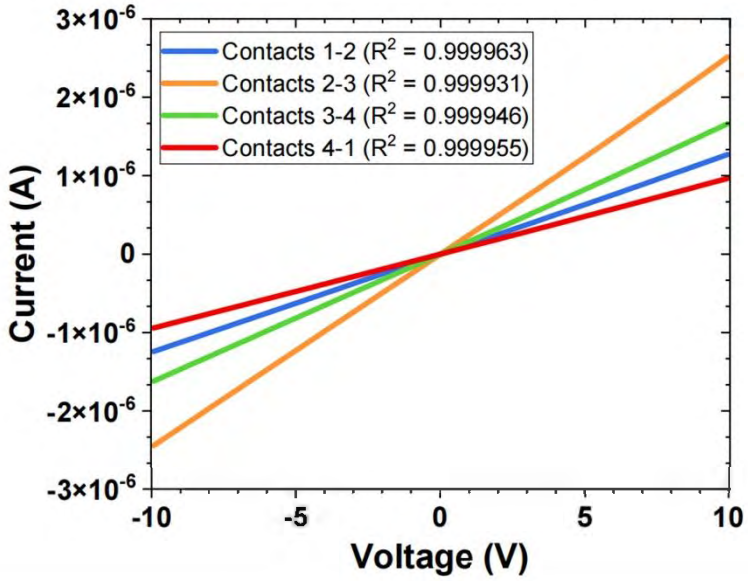

Figure 7.12: I-V behavior of the annealed Pt (10 nm)/Pd (10 nm)/Au (100 nm) contacts on the Be-doped AlN

7.5.2 Silicon-doped AlN Films

The HEM results of the AlN:Si sample exhibited an electron concentration of $9.7 \times 10^{17} \pm 1.12 \times 10^{15}$ cm^{-3}, a Hall coefficient of $6.37 \pm 7.3 \times 10^{-3}$ cm^3/C confirming the n-type nature of the material, a resistivity of 102 mΩ.cm ± 117 μΩ.cm with an SNR of 875.2, and a moderate Hall mobility of $62.45 \pm 71.5 \times 10^{-3}$ $cm^2/(V \cdot s)$ indicating some scattering mechanisms introduced by the Si doping, possibly due to impurities or defects. The I-V behavior of the Pt/Pd/Au contacts on the Si-dopedAlN sample at an annealing temperature of 900 °C is shown in Figure 7.13. The AlN:Si sample exhibits ohmic behavior at two orders of magnitude greater current at a given voltage than the Be-doped sample. This difference is primarily due to the higher carrier concentration and mobility in the Si-doped AlN. The linearity and I-V curves' steeper slope suggest lower resistance in the Si-doped AlN sample, consistent with its lower resistivity. The observed linearity and I-V curves' steeper slope indicate reduced resistivity in the Si-doped AlN sample.

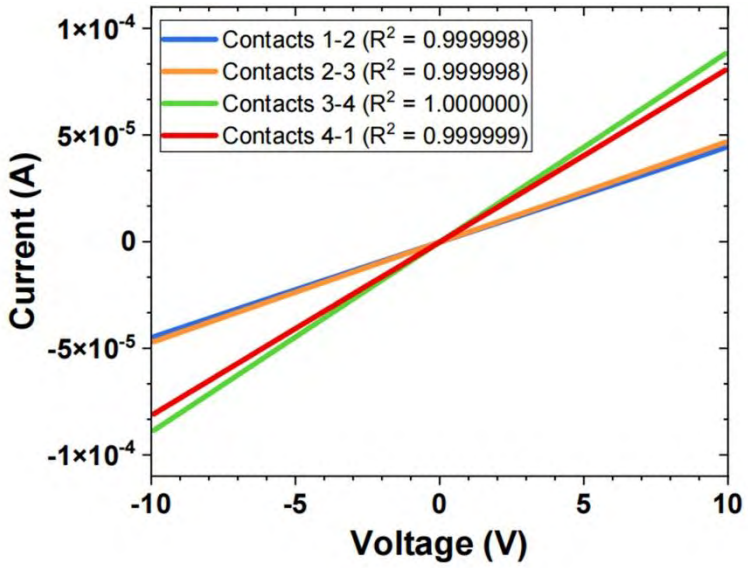

Figure 7.13: I-V behavior of the annealed Pt/Pd/Au (10 nm/10 nm/100 nm) contacts on AlN:Si samples

1.6 Comparison with Literature

7.6.1 TCAD Simulations

Existing studies have highlighted the advantages of GaN-based JBS diodes for high-power applications due to their minimal on-resistance and higher breakdown voltage [114], [115], [116], [117], [118]. AlN-on-GaN structures are less commonly explored but show promise due to the potential for enhanced electric field management and thermal stability. Previous research has often focused on optimizing material properties or diode structures, with less emphasis on the detailed impact of inter-p^+ spacing over a wide range. This study addresses a gap in the existing research by systematically examining the influence of inter-p^+ spacing over a wide range of 0.5 to 2.5 µm in GaN and AlN-on-GaN Junction Barrier Schottky (JBS) diodes using TCAD simulations, providing critical insights for practical design and application. Additionally, it presents a novel comparative TCAD analysis of various cost-effective metal contacts on undoped, n-type, and p-type AlN films.

7.6.2 Contacts to n-type AlN Films

Research on AlN contacts is quite limited, with only a few studies exploring this area.

- Contreras et al. [119] fabricated ohmic contacts by depositing a Ti/Al/Ni/Au (30 nm/180 nm/40 nm/150 nm) multilayer stack onto MBE-grown 1 µm-thick Si-

doped AlN films on a 30 nm GaN nucleation layer on sapphire substrates GaN capping layer of 3nm thickness. Subsequent annealing resulted in ~600 Ω·cm of resistivity, ~6 cm^2/Vs of Hall mobility and 1.7×10^{15} cm^{-3} of carrier concentration.\

- Breckenridge et al. [120] used e-beam evaporation and annealing at 850 °C for 60 seconds to create V(30 nm)/Al (100 nm)/Ni (70 nm)/Au (70 nm) contacts on 200 nm thick MOCVD-grown AlN homoepitaxial films deposited on AlN single-crystal substrates. Hall effect measurements indicated ~5×10^{18} cm^{-3} for electron concentration and ~1 cm^2/Vs for the Hall mobility.
- Numerous studies on Si-doped AlN have been presented; however, none of them demonstrated significant bulk conductivity.
- Ahmad et al. [17] fabricated Pt (10nm)/Pd (10nm)/Au (100nm) contact stacks on Si-doped AlN films and annealed them for a minute at 875 °C. The AlN films displayed bulk conductivity, with an electron mobility of 17 $cm^2/V \cdot s$ and around 6×10^{18} cm^{-3} of electron concentration.

In this study, the n-type AlN sample exhibited bulk conductivity with $9.7 \times 10^{17} \pm 1.12 \times 10^{15}$ cm^{-3} electron concentration, a resistivity of 102 mΩ.cm ± 117 μ Ω.cm, and 62.45 ± 71.5 × 10^{-3} $cm^2/(V \cdot s)$ Hall mobility.

7.6.3 Contacts to p-type AlN Films

Working with p-type AlN films is more challenging as we need metals with work functions close to the Fermi level of the p-type AlN which is in proximity to the valance band (that would be $\chi_{semi} + E_g$ (~8eV)).

- Ahmad et al. [14] fabricated Pt (10nm)/Pd (10nm)/Au (100nm) contact stacks on p-type AlN layers grown via MME and subjected to annealing for 1 minute at 800 °C. The AlN films exhibited p-type bulk conductivity with 3.1×10^{18} cm^{-3} of hole concentration.
- Nakarmi et al. [121] utilized MOCVD to grow Mg-doped AlN epilayers, each 1 μm in thickness, on AlN-coated sapphire substrates. The p-type resistivity was measured to be around 450 Ω·cm, with a mobility of 5.5 ± 3.4 $cm^2/V \cdot s$ at 850 K and approximately 2.5×10^{15} cm^{-3} hole concentration.
- Kishimoto et al. [122] produced surface p-type conductive layers of <10 nm thickness on AlN. 100 nm thick circular Ni electrodes were deposited followed by

annealing for 1 hour at 600 °C in H_2. The resulting C:AlN sample exhibited a sheet hole concentration of 4×10^{13} cm^{-2}, a sheet resistance of 3×10^4 Ω/sq, and a mobility of 5 $cm^2 V^{-1} s^{-1}$.

In this study, the p-type AlN sample yielded a resistivity value of 1.642 Ω·cm ± 1.64 mΩ·cm. The Hall effect measurements provided a significant mobility value of 13 ± 0.337 $cm^2/(V \cdot s)$ and an active bulk hole concentration of $2.92 \times 10^{17} \pm 7.58 \times 10^{15}$ cm^{-3}.

7.6.3 Contacts to undoped AlN Films

- Ahmad et al. [14] demonstrated a Pt (10nm)/Pd (10nm)/Au (100nm) contact stack on 100 nm MME-grown AlN on AlN. The annealed, undoped sample, which exhibited a clean, crack-free surface, showed extremely low currents in the nA range over a voltage range of -10 to 10 V with noticeable deviation from ideal linearity. This low-level current conduction is characteristic of highly resistive or insulating layers, a trend also observed in undoped annealed MME-grown AlN on sapphire with a similar contact stack [17].
- Xuewei Li et al. [92] fabricated Ti(20nm)/Al(130nm)/Ni(50nm)/Au(150nm) contacts on HVPE-grown undoped-AlN films via e-beam evaporation. The I-V behavior of undoped samples annealed at 200°C to 600°C and above 950 °C exhibited non-linear behavior, with currents in the $\leq 10^{-11}$ A range whereas in the 10^{-5} A range when annealed within the temperature range of 800 °C to 950 °C.

Currently, there are no reported studies on undoped AlN films that include Richardson analysis, to the best of our knowledge. However, the following studies provide a relevant comparison:

- Fu et al. [27] demonstrated ohmic contacts for MOCVD-grown n-AlN Schottky barrier diodes by depositing 20nm Ti/100nm Al/20nm Ti/50nm Au layers, followed by annealing for 30 seconds at 1000 °C. This study yielded a Schottky barrier height (Φ_B) of 0.9 to 1.6 eV and a Richardson constant (A*) of 48 A. $cm^{-2}K^{-2}$.
- Using vacuum-evaporated gold for the Schottky contact and aluminum for the ohmic contact, Hacke et al. [123] created Schottky barrier diodes using HVPE-grown unintentionally doped n-type GaN. An A* of 6×10^{-3} A/cm^2K^2 and a Φ_B of 0.844 eV were determined.

The A* in the current study is 7.19×10^{-7} A.cm^{-2}K^{-2}, and the Φ_B is 0.59 eV. The reduced Richardson constant in this study can be attributed to an additional barrier the electrons must tunnel. The presence of a thin native oxide layer, such as Al_2O_3 or SiO_2 on the AlN surface, or the direct tunneling of electrons into the metal from the semiconductor's conduction band could also contribute to the reduced Richardson constant [123]. The Schottky barrier height achieved is also low for undoped AlN, which can be attributed to the specific metal stack used and the quality of the AlN film.

CHAPTER 8

CONCLUSION AND FUTURE WORK

8.1 Conclusion

The study addressed the challenges in achieving high-crystalline-quality AlN films and low-resistance ohmic contacts to these films. Using Silvaco TCAD for device modeling and simulation provided valuable insights into the behavior of metal contacts on AlN films. The lowest Schottky energy barrier (Φ_B) of 2.9 eV for p-type and undoped AlN is obtained with the highest work function Pt metal contacts while low work function In contacts resulted in the lowest Φ_B of 1.6 eV for n-type AlN. The TCAD study also investigated the influence of inter-p^+ spacings on the performance of fully GaN-based and AlN-on-GaN Junction Barrier Schottky (JBS) diodes. Optimal JBS operation was found at 1-1.3 µm for GaN-based diodes and 1.1-1.4 µm for AlN/GaN diodes. For GaN-based diodes, the best trade-off between specific on-resistance ($R_{on,sp}$) and breakdown voltage (V_{br}) occurred at 1.2 µm spacing, yielding a BFOM of 347 MW/cm^2, $R_{on,sp}$ of 6.13×10^{-3} mΩ·cm^2, and V_{br} of 185.72 V. For AlN/GaN diodes, optimal performance was at 1.4 µm spacing with a BFOM of 678 MW/cm^2, $R_{on,sp}$ of 5.14×10^{-3} mΩ·cm^2, and V_{br} of 156.98 V. These optimized JBS diodes outperform PiN diodes in forward bias and Schottky diodes in reverse bias.

In the experimental study, the annealed undoped AlN samples exhibited exceptionally high currents likely due to defects such as cracks or impurities in the films. However, Sample 8, deposited using a magnetron sputtering power of 200 W, a substrate temperature of 300 °C, and an N_2 flow rate of 25 sccm, resulted in a high-quality, defect-free AlN film with current levels in the nanoampere range. Temperature-dependent I-V measurements yielded an effective Richardson constant of 7.19×10^{-7} A/cm²K² and a Schottky barrier height of 0.59 eV for Sample 8. The deposition of AlN thin films via metal-modulated epitaxy (MME) demonstrated the ability to achieve high-crystalline-quality films. Hall effect measurements confirmed significant bulk conductivity in AlN:Si

sample with 9.7×10^{17} electron concentration, a resistivity of 102 mΩ.cm, and 62.45 $cm^2/(V \cdot s)$ Hall mobility. The AlN:Be sample demonstrated bulk conductivity with 2.92×10^{17} cm^{-3} hole concentration, a Hall mobility of 13 $cm^2/(V \cdot s)$, and a resistivity of 1.642 Ω·cm. The study explored various high work function metal contact stacks, including Pt/Pd/Au for p-type and n-type AlN films, and cost-effective contact stacks of Ag, Al, Cu, Sn, and Zn metals for undoped AlN films, all of which demonstrated good adhesion and stability when interfaced with AlN films. Undoped AlN Sample 8, which was scratched and annealed at 300 °C for 10 minutes, employed Sn/Al/Ag contact stacks. The Pt/Pd/Au contact stacks on AlN:Si and AlN:Be films exhibited ohmic behavior following annealing at 900 °C and 800 °C for 1 min, respectively, with current levels approaching 0.1 mA for AlN:Si and 1 μA for AlN:Be films. The demonstrated high-crystalline-quality AlN films and low-resistance ohmic contacts can significantly enhance the performance of power electronics and semiconductor devices, offering practical solutions for advanced applications in power, RF, and optoelectronics. The electrical contacts demonstrated in this study particularly using cost-effective metals can be further optimized to enhance the efficiency and reliability of devices operating under extreme conditions, such as high power, temperature, and radiation environments.

8.2 Recommendations for Future Research

As the demand for high-performance electronic devices increases, further research is necessary to address the challenges in material quality and device optimization. Magnetron sputtering, while widely used for thin film deposition, is not ideal for working with wide bandgap materials like AlN, particularly for heteroepitaxial growth, due to its limitations such as high defect densities, poor crystallinity, limited thermal processing range, and inconsistent control over sputtering parameters [125]. Fabrication techniques like MBE or MOCVD should be preferred for their ability to better control the growth conditions and material properties [126].

Based on the TCAD simulations, although high work function metals could prove advantageous for p-type and undoped materials, opting for low work function metals would improve n-type AlN film’s performance.

To further optimize the JBS diode design, improvements could include incorporating a thicker, lower-doped drift layer and increasing the p^+-GaN doping concentration.

Future research could focus on further refining the contact optimization process by exploring alternative contact metals for improved performance and cost-effectiveness, annealing temperatures, and alternative doping strategies. Additionally, expanding the study to include other wide-bandgap semiconductors and their heterostructures could provide broader insights into the field of advanced electronic and optoelectronic materials.

REFERENCES

[1] J. Wu and W. Walukiewicz, "Band gaps of InN and group III nitride alloys," *Superlattices Microstruct*, vol. 34, no. 1–2, pp. 63–75, 2003.

[2] M. A. Khan, G. Simin, S. G. Pytel, A. Monti, E. Santi, and J. L. Hudgins, "New developments in gallium nitride and the impact on power electronics," in *2005 IEEE 36th Power Electronics Specialists Conference*, IEEE, 2005, pp. 15–26.

[3] A. Kumar *et al.*, "Wide band gap devices and their application in power electronics," *Energies (Basel)*, vol. 15, no. 23, p. 9172, 2022.

[4] B. Chatterjee, "Electro-Thermal Investigation of Next Generation Wide Bandgap Electronics," *The Pennsylvania State University*, 2020.

[5] W. M. Yim, E. J. Stofko, P. J. Zanzucchi, J. I. Pankove, M. Ettenberg, and S. L. Gilbert, "Epitaxially grown AlN and its optical band gap," *J Appl Phys*, vol. 44, no. 1, pp. 292–296, 1973.

[6] H.-Y. Joo, H. J. Kim, S. J. Kim, and S. Y. Kim, "Spectrophotometric analysis of aluminum nitride thin films," *Journal of Vacuum Science & Technology A: Vacuum, Surfaces, and Films*, vol. 17, no. 3, pp. 862–870, 1999.

[7] H. K. Lee and D. K. Kim, "Effect of second phase after-heat treatment on the thermal conductivity of AlN Ceramics," in *Key Engineering Materials*, Trans Tech Publ, 2009, pp. 61–63.

[8] K. Jagannadham, A. K. Sharma, Q. Wei, R. Kalyanraman, and J. Narayan, "Structural characteristics of AlN films deposited by pulsed laser deposition and reactive magnetron sputtering: A comparative study," *Journal of Vacuum Science & Technology A: Vacuum, Surfaces, and Films*, vol. 16, no. 5, pp. 2804–2815, 1998.

[9] S. Shanmugan, P. Anithambigai, and D. Mutharasu, "An effect of synthesis parameters on structural properties of AlN thin films deposited on metal substrates," *International Journal of Advanced Studies in Computers, Science and Engineering*, vol. 1, no. 4, p. 1, 2012.

[10] M.-H. Park and S.-H. Kim, "Thermal conductivity of AlN thin films deposited by RF magnetron sputtering," *Mater Sci Semicond Process*, vol. 15, no. 1, pp. 6–10, 2012.

[11] J. Y. Tsao *et al.*, "Ultrawide-bandgap semiconductors: research opportunities and challenges," *Adv Electron Mater*, vol. 4, no. 1, p. 1600501, 2018.

[12] X. Fu, "Aluminum Nitride Wide Band-gap Semiconductor and Its Basic Characteristics," 2016, doi: 10.2991/EMIM-16.2016.117.

[13] S. Fukumoto, T. Hookabe, and H. Tsubakino, “Hydrolysis behavior of aluminum nitride in various solutions,” *J Mater Sci*, vol. 35, pp. 2743–2748, 2000.

[14] H. Ahmad, J. Lindemuth, Z. Engel, C. M. Matthews, T. M. McCrone, and W. A. Doolittle, “Substantial P-Type Conductivity of AlN Achieved via Beryllium Doping,” *Advanced Materials*, vol. 33, no. 42, p. 2104497, 2021.

[15] “Aluminum nitride | AlN | CID 90455 - PubChem.” Accessed: Aug. 29, 2024. [Online]. Available: https://pubchem.ncbi.nlm.nih.gov/compound/Aluminum-nitride

[16] “Silicon | Si | CID 5461123 - PubChem.” Accessed: Aug. 29, 2024. [Online]. Available: https://pubchem.ncbi.nlm.nih.gov/compound/Silicon

[17] H. Ahmad, Z. Engel, C. M. Matthews, S. Lee, and W. A. Doolittle, “Realization of homojunction PN AlN diodes,” *J Appl Phys*, vol. 131, no. 17, 2022.

[18] K. A. Aissa *et al.*, “Thermal conductivity measurement of AlN films by fast photothermal method,” in *Journal of Physics: Conference Series*, IOP Publishing, 2012, p. 012089.

[19] A. T. Wieg, Y. Kodera, Z. Wang, T. Imai, C. Dames, and J. E. Garay, “Visible photoluminescence in polycrystalline terbium doped aluminum nitride (Tb: AlN) ceramics with high thermal conductivity,” *Appl Phys Lett*, vol. 101, no. 11, p. 111903, 2012.

[20] M. C. Benjamin, C. Wang, R. F. Davis, and R. J. Nemanich, “Observation of a negative electron affinity for heteroepitaxial AlN on α (6H)-SiC (0001),” *Appl Phys Lett*, vol. 64, no. 24, pp. 3288–3290, 1994.

[21] H. B. Michaelson, “Work functions of the elements,” *J Appl Phys*, vol. 21, no. 6, pp. 536–540, 1950.

[22] C. L. A. Cunha, T. C. Pimenta, and M. A. Fraga, “Development and Applications of Aluminum Nitride Thin Film Technology,” in *Thin Film Deposition-Fundamentals, Processes, and Applications*, IntechOpen, 2022.

[23] X.-D. Wang, W. Jiang, M. G. Norton, and K. W. Hipps, “Morphology and orientation of nanocrystalline AlN thin films,” *Thin Solid Films*, vol. 251, no. 2, pp. 121–126, 1994.

[24] H. Morkoç, *Nitride Semiconductors and Devices*, vol. 32. in Springer Series in Materials Science, vol. 32. Berlin, Heidelberg: Springer Berlin Heidelberg, 1999. doi: 10.1007/978-3-642-58562-3.

[25] G. F. Iriarte, “Influence of the magnetron on the growth of aluminum nitride thin films deposited by reactive sputtering,” *Journal of Vacuum Science & Technology A: Vacuum, Surfaces, and Films*, vol. 28, no. 2, pp. 193–198, 2010.

[26] R. F. Dalmau, *Aluminum Nitride bulk crystal growth in a resistively heated reactor*. North Carolina State University, 2005.

[27] H. Fu *et al.*, “Demonstration of AlN Schottky barrier diodes with blocking voltage over 1 kV,” *IEEE Electron Device Letters*, vol. 38, no. 9, pp. 1286–1289, 2017.

[28] R. F. Pierret, *Semiconductor device fundamentals*. Pearson Education India, 1996.

[29] A. Casadei, “GaAs nanowires: from doping to plasmonic hybrid devices,” EPFL, 2016.

[30] R. T. Tung, “Recent advances in Schottky barrier concepts,” *Materials Science and Engineering: R: Reports*, vol. 35, no. 1–3, pp. 1–138, 2001.

[31] V. N. Brudnyi, A. V Kosobutsky, and N. G. Kolin, “The charge neutrality level and the fermi level pinning in A 3 N (BN, AlN, GaN, InN) nitrides,” *Russian Physics Journal*, vol. 51, pp. 1270–1278, 2008.

[32] R. Islam, G. Shine, and K. C. Saraswat, “Schottky barrier height reduction for holes by Fermi level depinning using metal/nickel oxide/silicon contacts,” *Appl Phys Lett*, vol. 105, no. 18, 2014.

[33] G. Greco, F. Iucolano, and F. Roccaforte, “Ohmic contacts to Gallium Nitride materials,” *Appl Surf Sci*, vol. 383, pp. 324–345, 2016.

[34] B. J. Baliga, *Fundamentals of power semiconductor devices*. Springer Science & Business Media, 2010.

[35] T. Kimoto and J. A. Cooper, *Fundamentals of silicon carbide technology: growth, characterization, devices and applications*. John Wiley & Sons, 2014.

[36] B. M. Wilamowski, “Schottky diodes with high breakdown voltages,” *Solid State Electron*, vol. 26, no. 5, pp. 491–493, 1983.

[37] B. J. Baliga, “The pinch rectifier: A low-forward-drop high-speed power diode,” *IEEE Electron Device Letters*, vol. 5, no. 6, pp. 194–196, 1984.

[38] J.-S. Lai, X. Huang, H. Yu, A. R. Hefner, D. W. Berning, and R. Singh, “High current SiC JBS diode characterization for hard-and soft-switching applications,” in *Conference Record of the 2001 IEEE Industry Applications Conference. 36th IAS Annual Meeting (Cat. No. 01CH37248)*, IEEE, 2001, pp. 384–390.

[39] X. Li, F. Xiao, Y. Luo, and Y. Duan, “Parameter extraction method for a physics-based lumped-charge SiC MPS diode model,” *IET Power Electronics*, vol. 13, no. 14, pp. 2992–3000, 2020.

[40] B. J. Baliga, *Silicon carbide power devices*. World scientific, 2006.

[41] Y. Zhang, X. Lu, and X. Zou, “Device design assessment of GaN merged PiN Schottky diodes,” *Electronics (Basel)*, vol. 8, no. 12, p. 1550, 2019.

[42] B. N. Pushpakaran, S. B. Bayne, and A. A. Ogunniyi, “Physics based electro-thermal transient simulation of 4H-SiC JBS diode using Silvaco ATLAS,” in *2015 IEEE Pulsed Power Conference (PPC)*, IEEE, 2015, pp. 1–5.

[43] R. T. Tung, “Electron transport at metal-semiconductor interfaces: General theory,” *Phys Rev B*, vol. 45, no. 23, p. 13509, 1992.

[44] H. Bartolf, V. Sundaramoorthy, A. Mihaila, and V. Benda, “Simulation Study of a JBS-Rectifier with Close to Schottky-Interface Conduction Investigated for High-Voltage Classes,” in *Proceedings of the International Seminar on Power Semiconductors, ISPS2014, Prague, edited by V. Benda (CTU Prague, 2014) p*, 2014.

[45] Y. Zhang *et al.*, “Vertical GaN junction barrier Schottky rectifiers by selective ion implantation,” *IEEE Electron Device Letters*, vol. 38, no. 8, pp. 1097–1100, 2017.

[46] A. D. Koehler *et al.*, “Vertical GaN junction barrier Schottky diodes,” *ECS Journal of Solid State Science and Technology*, vol. 6, no. 1, p. Q10, 2016.

[47] J. X. Zhang *et al.*, “Growth of AlN films on Si (100) and Si (111) substrates by reactive magnetron sputtering,” *Surf Coat Technol*, vol. 198, no. 1–3, pp. 68–73, 2005.

[48] B. Riah *et al.*, “Hetero-Epitaxial Growth of AlN Deposited by DC Magnetron Sputtering on Si (111) Using a AlN Buffer Layer,” *Coatings*, vol. 11, no. 9, p. 1063, 2021.

[49] M. K. Sandager, C. Kjelde, and V. Popok, “Growth of Thin AlN films on Si Wafers by Reactive Magnetron Sputtering: Role of Processing Pressure, Magnetron Power and Nitrogen/Argon Gas Flow Ratio,” *Crystals (Basel)*, vol. 12, no. 10, p. 1379, 2022.

[50] I.-S. Shin, J. Kim, D. Lee, D. Kim, Y. Park, and E. Yoon, “Epitaxial growth of single-crystalline AlN layer on Si (111) by DC magnetron sputtering at room temperature,” *Jpn J Appl Phys*, vol. 57, no. 6, p. 060306, 2018.

[51] G. F. Iriarte, F. Engelmark, M. Ottosson, and I. V Katardjiev, “Influence of deposition parameters on the stress of magnetron sputter-deposited AlN thin films on Si (100) substrates,” *J Mater Res*, vol. 18, no. 2, pp. 423–432, 2003.

[52] F. Medjani, R. Sanjinés, G. Allidi, and A. Karimi, “Effect of substrate temperature and bias voltage on the crystallite orientation in RF magnetron sputtered AlN thin films,” *Thin Solid Films*, vol. 515, no. 1, pp. 260–265, 2006.

[53] X. Jiao, Y. Shi, H. Zhong, R. Zhang, and J. Yang, “AlN thin films deposited on different Si-based substrates through RF magnetron sputtering,” *Journal of Materials Science: Materials in Electronics*, vol. 26, pp. 801–808, 2015.

[54] P. Panda *et al.*, “Reduction of residual stress in AlN thin films synthesized by magnetron sputtering technique,” *Mater Chem Phys*, vol. 200, pp. 78–84, 2017.

[55] A. Das, M. Rath, D. R. Nair, M. S. R. Rao, and A. DasGupta, “Realization of preferential (100) oriented AlN thin films on Mo coated Si substrate using reactive RF magnetron sputtering,” *Appl Surf Sci*, vol. 550, p. 149308, 2021.

[56] J. H. Choi, J. Y. Lee, and J. H. Kim, “Phase evolution in aluminum nitride thin films on Si (100) prepared by radio frequency magnetron sputtering,” *Thin Solid Films*, vol. 384, no. 2, pp. 166–172, 2001.

[57] H. Jin *et al.*, “Influence of substrate temperature on structural properties and deposition rate of AlN thin film deposited by reactive magnetron sputtering,” *J Electron Mater*, vol. 41, pp. 1948–1954, 2012.

[58] J. Han *et al.*, “Influence of nitrogen flow ratio on the optical property of AlN deposited by DC magnetron sputtering on Si (100) substrate,” *Micro Nano Lett*, vol. 15, no. 8, pp. 556–560, 2020.

[59] T. Li *et al.*, “Influence of pressure on the properties of AlN deposited by DC reactive magnetron sputtering on Si (100) substrate,” *Micro Nano Lett*, vol. 14, no. 2, pp. 146–149, 2019.

[60] S. Khan *et al.*, “Texture of the nano-crystalline AlN thin films and the growth conditions in DC magnetron sputtering,” *Progress in Natural Science: Materials International*, vol. 25, no. 4, pp. 282–290, 2015.

[61] Q. Wei *et al.*, “Effects of sputtering pressure on nanostructure and nanomechanical properties of AlN films prepared by RF reactive sputtering,” *Transactions of Nonferrous Metals Society of China*, vol. 24, no. 9, pp. 2845–2855, 2014.

[62] C. Duquenne *et al.*, “Magnetron sputtering of aluminium nitride thin films for thermal management,” *Plasma Processes and Polymers*, vol. 4, no. S1, pp. S1–S5, 2007.

[63] C. Cheng, Y. Chen, H. Wang, and W. Chen, “Low-temperature growth of aluminum nitride thin films on silicon by reactive radio frequency magnetron sputtering,” *Journal of Vacuum Science & Technology A: Vacuum, Surfaces, and Films*, vol. 14, no. 4, pp. 2238–2242, 1996.

[64] C. Han *et al.*, “High potential columnar nanocrystalline AlN films deposited by RF reactive magnetron sputtering,” *Nanomicro Lett*, vol. 4, pp. 40–44, 2012.

[65] I. C. Oliveira, K. G. Grigorov, H. S. Maciel, M. Massi, and C. Otani, “High textured AlN thin films grown by RF magnetron sputtering; composition, structure, morphology and hardness,” *Vacuum*, vol. 75, no. 4, pp. 331–338, 2004.

[66] C. Stoeckel, C. Kaufmann, R. Hahn, R. Schulze, D. Billep, and T. Gessner, “Pulsed dc magnetron sputtered piezoelectric thin film aluminum nitride–technology and piezoelectric properties,” *J Appl Phys*, vol. 116, no. 3, p. 034102, 2014.

[67] D.-T. Phan and G.-S. Chung, “The effect of geometry and post-annealing on surface acoustic wave characteristics of AlN thin films prepared by magnetron sputtering,” *Appl Surf Sci*, vol. 257, no. 20, pp. 8696–8701, 2011.

[68] A. V. Singh, S. Chandra, and G. Bose, “Deposition and characterization of c-axis oriented aluminum nitride films by radio frequency magnetron sputtering without external substrate heating,” *Thin Solid Films*, vol. 519, no. 18, pp. 5846–5853, 2011.

[69] A. Ababneh, U. Schmid, J. Hernando, J. L. Sánchez-Rojas, and H. Seidel, “The influence of sputter deposition parameters on piezoelectric and mechanical properties of AlN thin films,” *Materials Science and Engineering: B*, vol. 172, no. 3, pp. 253–258, 2010.

[70] S. Venkataraj, D. Severin, R. Drese, F. Koerfer, and M. Wuttig, “Structural, optical and mechanical properties of aluminium nitride films prepared by reactive DC magnetron sputtering,” *Thin Solid Films*, vol. 502, no. 1–2, pp. 235–239, 2006.

[71] X. Bi, Y. Wu, J. Wu, H. Li, and L. Zhou, “A model for longitudinal piezoelectric coefficient measurement of the aluminum nitride thin films,” *Journal of Materials Science: Materials in Electronics*, vol. 25, pp. 2435–2442, 2014.

[72] J. P. Kar, G. Bose, and S. Tuli, “Influence of rapid thermal annealing on morphological and electrical properties of RF sputtered AlN films,” *Mater Sci Semicond Process*, vol. 8, no. 6, pp. 646–651, 2005.

[73] B. Abdallah *et al.*, “Thickness and substrate effects on AlN thin film growth at room temperature,” *The European Physical Journal-Applied Physics*, vol. 43, no. 3, pp. 309–313, 2008.

[74] F. Engelmark, G. Fucntes, I. V Katardjiev, A. Harsta, U. Smith, and S. Berg, “Synthesis of highly oriented piezoelectric AlN films by reactive sputter

deposition," *Journal of Vacuum Science & Technology A: Vacuum, Surfaces, and Films*, vol. 18, no. 4, pp. 1609–1612, 2000.

[75] M. B. Assouar, M. El Hakiki, O. Elmazria, P. Alnot, and C. Tiusan, "Synthesis and microstructural characterisation of reactive RF magnetron sputtering AlN films for surface acoustic wave filters," *Diam Relat Mater*, vol. 13, no. 4–8, pp. 1111–1115, 2004.

[76] A. C. Galca, G. E. Stan, L. M. Trinca, C. C. Negrila, and L. C. Nistor, "Structural and optical properties of c-axis oriented aluminum nitride thin films prepared at low temperature by reactive radio-frequency magnetron sputtering," *Thin Solid Films*, vol. 524, pp. 328–333, 2012.

[77] X. Meng, C. Yang, Q. Chen, Y. Gao, and J. Yang, "Preparation of highly c-axis oriented AlN films on Si substrate with ZnO buffer layer by the DC magnetron sputtering," *Mater Lett*, vol. 90, pp. 49–52, 2013.

[78] W.-S. Liu *et al.*, "Optimal Growth Conditions for Forming c-Axis (002) Aluminum Nitride Thin Films as a Buffer Layer for Hexagonal Gallium Nitride Thin Films Produced with In Situ Continual Radio Frequency Sputtering," *Micromachines (Basel)*, vol. 13, no. 9, p. 1546, 2022.

[79] I. Ivanov *et al.*, "Growth of epitaxial AlN (0001) on Si (111) by reactive magnetron sputter deposition," *J Appl Phys*, vol. 78, no. 9, pp. 5721–5726, 1995.

[80] K. A. Aissa *et al.*, "AlN films deposited by dc magnetron sputtering and high power impulse magnetron sputtering for SAW applications," *J Phys D Appl Phys*, vol. 48, no. 14, p. 145307, 2015.

[81] W. A. Doolittle *et al.*, "Prospectives for AlN electronics and optoelectronics and the important role of alternative synthesis," *Appl Phys Lett*, vol. 123, no. 7, 2023.

[82] C. Stampfl and C. G. Van de Walle, "Theoretical investigation of native defects, impurities, and complexes in aluminum nitride," *Phys Rev B*, vol. 65, no. 15, p. 155212, 2002.

[83] C. G. Van de Walle and J. Neugebauer, "First-principles calculations for defects and impurities: Applications to III-nitrides," *J Appl Phys*, vol. 95, no. 8, pp. 3851–3879, 2004.

[84] J. Y. Tsao *et al.*, "N- and P- type Doping in Al-rich AlGaN and AlN," *Adv Electron Mater*, vol. 4, no. 1, p. 1600501, 2018.

[85] R. R. Sumathi, "Status and challenges in hetero-epitaxial growth approach for large diameter AlN single crystalline substrates," *ECS Journal of Solid State Science and Technology*, vol. 10, no. 3, p. 035001, 2021.

[86] Y. Taniyasu, M. Kasu, and N. Kobayashi, “Intentional Control of n-type Conduction for Si-doped AlN and AlxGa1—xN with High Al Content,” *physica status solidi (b)*, vol. 234, no. 3, pp. 845–849, 2002.

[87] R. Zeisel *et al.*, “DX-behavior of Si in AlN,” *Phys Rev B*, vol. 61, no. 24, p. R16283, 2000.

[88] R. Q. Wu *et al.*, “Possible efficient p-type doping of AlN using Be: An ab initio study,” *Appl Phys Lett*, vol. 91, no. 15, 2007.

[89] Y. Zhang, W. Liu, and H. Niu, “Native defect properties and p-type doping efficiency in group-IIA doped wurtzite AlN,” *Phys Rev B*, vol. 77, no. 3, p. 035201, 2008.

[90] J. Liu, J. Ma, X. Du, F. Han, S. Shi, and G. Yang, “Tailoring p-type conductivity of aluminum nitride via transition metal and fluorine doping,” *J Alloys Compd*, vol. 862, p. 158017, 2021.

[91] Z. Lu, F. Wang, and Y. Liu, “The first principle calculation of improving p-type characteristics of B x Al1-x N,” *Sci Rep*, vol. 11, no. 1, p. 12720, 2021.

[92] X. Li *et al.*, “Effect of annealing temperature on Ti/Al/Ni/Au ohmic contacts on undoped AlN films,” *Journal of Semiconductors*, vol. 38, no. 11, p. 116002, 2017.

[93] H. Ahmad, Z. Engel, C. M. Matthews, and W. A. Doolittle, “p-type AlN based heteroepitaxial diodes with Schottky, Pin, and junction barrier Schottky character achieving significant breakdown performance,” *J Appl Phys*, vol. 130, no. 19, p. 195702, 2021.

[94] P. Reddy *et al.*, “Schottky contact formation on polar and non-polar AlN,” *J Appl Phys*, vol. 116, no. 19, p. 194503, 2014.

[95] A. V Sachenko *et al.*, “Resistance formation mechanisms for contacts to n-GaN and n-AlN with high dislocation density,” *physica status solidi c*, vol. 10, no. 3, pp. 498–500, 2013.

[96] M. Hiroki and K. Kumakura, “Ohmic contact to AlN: Si using graded AlGaN contact layer,” *Appl Phys Lett*, vol. 115, no. 19, p. 192104, 2019.

[97] T. Kinoshita *et al.*, “Fabrication of vertical Schottky barrier diodes on n-type freestanding AlN substrates grown by hydride vapor phase epitaxy,” *Applied Physics Express*, vol. 8, no. 6, p. 061003, 2015.

[98] J. Chowdhury, J. K. Das, A. Sarkar, and K. Mohapatra, “TCAD simulation of emerging nanoscale devices,” in *Nanoelectronics: Physics, Materials and Devices*, Elsevier, 2023, pp. 409–455.

[99] A. B. Renz *et al.*, “The optimization of 3.3 kV 4H-SiC JBS diodes,” *IEEE Trans Electron Devices*, vol. 69, no. 1, pp. 298–303, 2021.

[100] H. Bartolf, V. Sundaramoorthy, A. Mihaila, M. Berthou, P. Godignon, and J. Millan, “Study of 4H-SiC Schottky diode designs for 3.3 kV applications,” in *Materials Science Forum*, Trans Tech Publ, 2014, pp. 795–799.

[101] Y. Taniyasu, M. Kasu, and N. Kobayashi, “Intentional Control of n-type Conduction for Si-doped AlN and AlxGa1—xN with High Al Content,” *physica status solidi (b)*, vol. 234, no. 3, pp. 845–849, 2002.

[102] R. Zeisel *et al.*, “DX-behavior of Si in AlN,” *Phys Rev B*, vol. 61, no. 24, p. R16283, 2000.

[103] C. J. Powell, “Electron Stopping Powers,” in *CRC Handbook of Chemistry and Physics*, 97th ed., W. M. Haynes, D. R. Lide, and T. J. Bruno, Eds., Boca Raton: CRC Press, 2017, pp. 12–123.

[104] A. Bendjerad, S. Boukhtache, A. Benhaya, D. Luneau, H. A. S. El, and K. Benyahia, “Modeling of magnetic properties of iron thin films deposited by RF magnetron sputtering using Preisach model,” *Serbian Journal of Electrical Engineering*, vol. 13, no. 2, pp. 229–238, 2016.

[105] B. Stuhrmann, “Self-Organized Active Biopolymer Networks in Migrating Living Cells,” PhD, Robert Bosch GmbH, Reutlingen, Germany, 2009.

[106] E. M. Mkawi, Y. Al-Hadeethi, E. Shalaan, and E. Bekyarova, “Substrate temperature effect during the deposition of (Cu/Sn/Cu/Zn) stacked precursor CZTS thin film deposited by electron-beam evaporation,” *Journal of Materials Science: Materials in Electronics*, vol. 29, pp. 20476–20484, 2018.

[107] D. El Khoury, “Towards the use of Electrostatic Force Microscopy to study interphases in nanodielectric materials,” PhD diss., Université Montpellier, 2017.

[108] H. Fujiwara, *Spectroscopic Ellipsometry: Principles and Applications*. John Wiley & Sons, 2007.

[109] B. J. Inkson, “Scanning electron microscopy (SEM) and transmission electron microscopy (TEM) for materials characterization,” in *Materials characterization using nondestructive evaluation (NDE) methods*, Elsevier, 2016, pp. 17–43.

[110] M. Kamalanathan, H. Shamima, R. Gopalakrishnan, and K. Vishista, “Influence of solvents on solvothermal synthesis of Cu2SnS3 nanoparticles with enhanced optical, photoconductive and electrical properties,” *Mater. Technol*, vol. 33, pp. 72–78, 2018.

[111] J. Pastrňák and L. Roskovcová, “Refraction index measurements on AlN single crystals,” *physica status solidi (b)*, vol. 14, no. 1, pp. K5–K8, 1966.

[112] L. Y. Beliaev, E. Shkondin, A. V Lavrinenko, and O. Takayama, “Thickness-dependent optical properties of aluminum nitride films for mid-infrared wavelengths,” *Journal of Vacuum Science & Technology A*, vol. 39, no. 4, 2021.

[113] G. Çankaya and N. Ucar, “Schottky barrier height dependence on the metal work function for p-type Si Schottky diodes,” *Zeitschrift für Naturforschung A*, vol. 59, no. 11, pp. 795–798, 2004.

[114] L. Yates *et al.*, “Demonstration of> 6.0-kV breakdown voltage in large area vertical GaN pn diodes with step-etched junction termination extensions,” *IEEE Trans Electron Devices*, vol. 69, no. 4, pp. 1931–1937, 2022.

[115] Y. Saitoh *et al.*, “Extremely low on-resistance and high breakdown voltage observed in vertical GaN Schottky barrier diodes with high-mobility drift layers on low-dislocation-density GaN substrates,” *Applied Physics Express*, vol. 3, no. 8, p. 081001, 2010.

[116] H. Bartolf, A. Mihaila, L. Knoll, V. K. Sundaramoorthy, R. A. Minamisawa, and E. Bianda, “JBS power-rectifiers for 1.7 kV applications with conduction properties close to pure Schottky-design,” in *2015 17th European Conference on Power Electronics and Applications (EPE’15 ECCE-Europe)*, IEEE, 2015, pp. 1–10.

[117] H. Ahmad, Z. Engel, A. Ghosh, C. M. Matthews, and W. A. Doolittle, “GaN: Be I-Layer-Based High-Power pin Diodes Achieving Large Quasi-Vertical MBE Breakdown Performance,” *IEEE Trans Electron Devices*, vol. 69, no. 5, pp. 2566–2572, 2022.

[118] T. Hayashida, T. Nanjo, A. Furukawa, and M. Yamamuka, “Vertical GaN merged PiN Schottky diode with a breakdown voltage of 2 kV,” *Applied Physics Express*, vol. 10, no. 6, p. 061003, 2017.

[119] S. Contreras *et al.*, “High temperature electrical transport study of Si-doped AlN,” *Superlattices Microstruct*, vol. 98, pp. 253–258, 2016.

[120] M. H. Breckenridge *et al.*, “High n-type conductivity and carrier concentration in Si-implanted homoepitaxial AlN,” *Appl Phys Lett*, vol. 118, no. 11, 2021.

[121] M. L. Nakarmi, N. Nepal, C. Ugolini, T. M. Altahtamouni, J. Y. Lin, and H. X. Jiang, “Correlation between optical and electrical properties of Mg-doped AlN epilayers,” *Appl Phys Lett*, vol. 89, no. 15, 2006.

[122] K. Kishimoto, M. Funato, and Y. Kawakami, “Control of p-type conductivity at AlN surfaces by carbon doping,” *Applied Physics Express*, vol. 13, no. 1, p. 015512, 2020.

[123] P. Hacke, T. Detchprohm, K. Hiramatsu, and N. Sawaki, “Schottky barrier on n-type GaN grown by hydride vapor phase epitaxy,” *Appl Phys Lett*, vol. 63, no. 19, pp. 2676–2678, 1993.

[124] H. Kim, H. J. Yun, S. Choi, and B. J. Choi, “Atomic Layer Deposition of AlN Thin Films on GaN and Electrical Properties in AlN/GaN Heterojunction Diodes,” *Transactions on Electrical and Electronic Materials*, vol. 21, pp. 621–629, 2020.

[125] B. Peng, D. Gong, W. Zhang, J. Jiang, L. Shu, and Y. Zhang, “Effects of sputtering parameters on AlN film growth on flexible hastelloy tapes by two-step deposition technique,” *Materials*, vol. 9, no. 8, p. 686, 2016.

[126] P. Capper, S. Irvine, and T. Joyce, “Epitaxial Crystal Growth: Methods and Materials,” in *Springer Handbook of Electronic and Photonic Materials*, S. Kasap and P. Capper, Eds., Cham: Springer International Publishing, 2017, p. 1. doi: 10.1007/978-3-319-48933-9_14.